Next Generation Materials and Strategies for the Advancement of Redox-Flow Batteries

Jaime Rodriguez

A dissertation

submitted in partial fulfillment of the

requirements for the degree of

Doctor of Philosophy

University of Washington

2021

Reading Committee:

Lilo D. Pozzo, Chair

Stuart Adler

David Beck

Daniel Schwartz

Program Authorized to Offer Degree:

Chemical Engineering

University of Washington

Abstract

Next Generation Materials and Strategies for the Advancement of Redox-Flow Batteries

Jaime Rodriguez

Chair of the Supervisory Committee:

Dr. Lilo D. Pozzo

Chemical Engineering

Initiatives to increase the capacity of renewable energy into our electrical grid have grown substantially over the last decade in efforts to reduce global carbon emissions. The COVID-19 pandemic saw an unprecedented decline in demand for fossil fuels, while demand for renewables surged. Despite this temporary curb in carbon emissions, they have rebounded strongly as the economy begins to recover. Demand for renewables will continue to increase as a result, yet the inherent intermittency of this energy source poses a challenge for meeting this demand. The use of batteries as electrochemical energy storage devices has shown promise for solving this issue, reversibly converting electrical energy into chemical energy to smooth out the intermittency of renewables. One type of battery, Redox-flow batteries (RFBs), have become particularly attractive due to their unique aspect of separating the power and energy from the system. This allows for flexibility in terms of scaling and sizing. Despite this advantage, the high cost of the materials for

this technology has limited its commercialization. This dissertation will discuss research efforts to develop higher performing, cost effective, and sustainable alternative materials necessary for the commercial penetration of RFBs. Early work in developing low-cost sol-gel ceramic membranes will be addressed, which resulted in a patent outlining a development process which reduced the cost by almost 10x compared to the industry standard for RFBs. Next, research focusing on the use of redox-active organic materials as a cost effective and environmentally sustainable alternative to the current metal-ion based RFBs is presented, where derivatives of the fluorenone molecule, a common abundant precursor in organic synthesis and pharmaceuticals, were demonstrated for use in an aqueous RFB. Finally, efforts to incorporate deep-eutectic solvent electrolytes into organic based RFBs will be highlighted, giving an overview of the high-throughput and data-driven strategies necessary to probe the immense design space for these materials.

TABLE OF CONTENTS

LIST OF FIGURES

LIST OF TABLES

Chapter 1. INTRODUCTION AND MOTIVATION

1.1 THE RISE OF RENEWABLE ENERGY

The Global Carbon Project reported a 0.6% rise in global CO2 emissions in 2019, leading to a historical high of 36.4 Gt of CO2.[1] While it was expected for this trend to continue increasing in 2020, the emergence of the Covid-19 pandemic drastically impacted global energy demand and usage. Emissions declined by an unprecedented 2.4 Gt of CO2 in 2020, which signaled the largest drop in recorded history, and largest relative drop in emissions since the second world war.[2] While the demand for conventional fossil fuels plummeted as a result of the pandemic, renewables were the only energy source to experience any type of growth in demand during this period.[3] Additions to renewable energy capacity increased by 45% in 2020 and were largely driven by solar and wind power.[4] This was positive news as renewable energy sources have gained considerable attention to combat global dependence on fossil fuels which contribute to CO2 emissions, and consequently, negative environmental impacts from climate change. This curb in emissions was short-lived, however. Once the economy began to recover from the pandemic, so did the demand for fossil fuels as usage rebounded strongly towards the end of 2020 and beginning of 2021, even surpassing 2019 levels.[5] Despite this resurgence, the demand for renewables is expected to continue increasing. The economic barriers to renewable energy technologies have declined significantly, with solar and wind power approaching a mere 2-3 cents per kilowatt-hr (kWh) in many countries.[6] Politically, initiatives such as the Paris Climate Accord have brought collective international efforts to counteract and mitigate the effects of climate change. Domestically here in the U.S., a

number of states have adopted serious initiatives to pledge near-total conversion to clean, renewable energy, most notably California and Hawaii which have both pledged 100% renewable energy goals by the year 2045.[7] Based on these collective initiatives, projections forecast that 22% of U.S. electricity will be generated by renewables in 2022.[8] It is evident that the potential for renewable energy growth will not slow down, as general consumers and the private sector seek a shift away from fossil fuel energy.

1.2 The Need for Adequate Energy storage

While the increase in adoption of renewable energy appears to be a trend that will not soon let up, there is a crucial aspect that is often overlooked that must be addressed in conjunction - energy storage. An effective electrical grid requires a certain degree of flexibility to be able to maintain balance between the demand for electricity from consumers and the supply of that electricity to them. Due to the inherent intermittent nature of renewables, there is an inability to maintain this balance, and as a result traditional methods of electricity generation are still required to bridge the gap. As detailed in Figure 1.1, the use of energy storage to smooth out this intermittency and provide electricity even at times of little to no output and high demand is a promising solution to this issue. However, only about 2.5% of electricity is dispatched via storage in the U.S., with these percentages being only slightly higher in some other countries.[9]

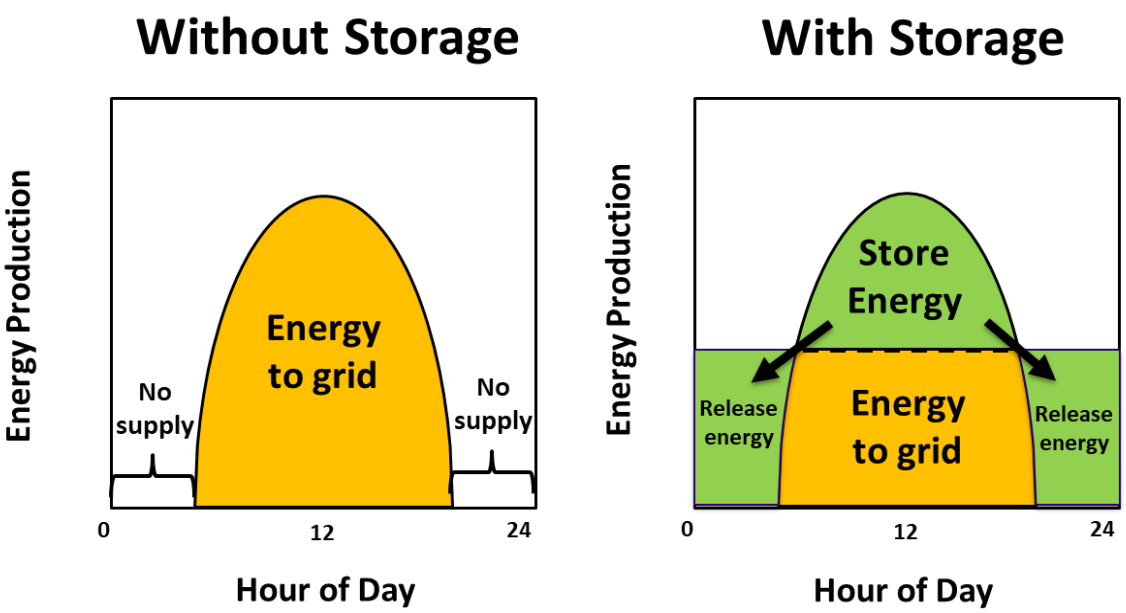

Figure 1.1. Diagram detailing the use of energy storage to supply electricity demand from times of little to no output from renewables.

This statistic causes concern as studies have suggested that significant grid destabilization could occur if the grid were to be comprised of more than 20% renewables without energy storage.[10] With reports suggesting that 80% of the worlds electricity generation could be derived from renewables by 2050, adequate grid-scale energy storage is crucial for this projection to even be possible.[11]

To date, a wide variety of energy storage technologies exist, which includes mechanical, electrical, chemical, and electrochemical storage.[12] These can be compared amongst each other based on their power ratings and discharge times, as seen in Figure 1.2.

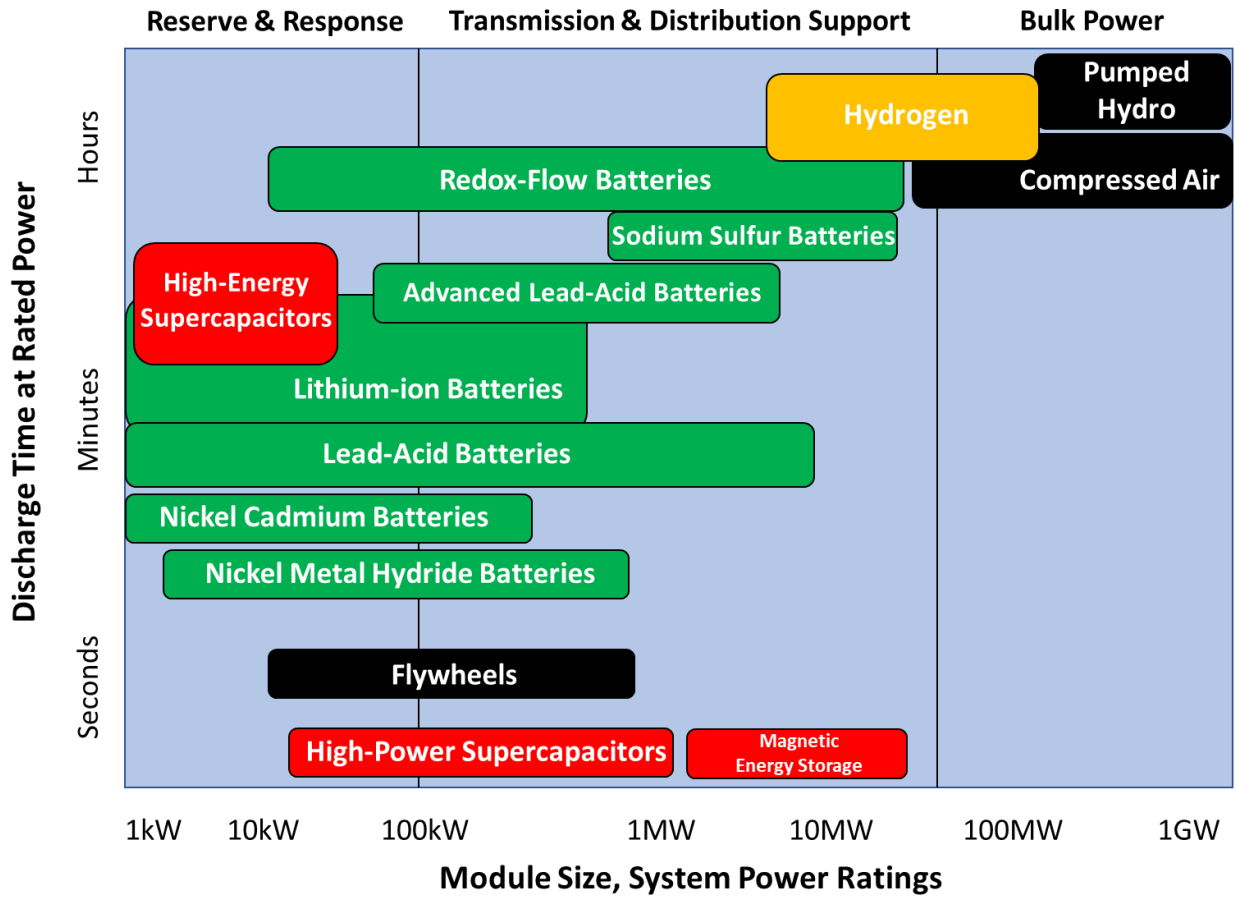

Figure 1.2. Comparison of available energy storage technologies based on power ratings and discharge times.

We see that many of these technologies have certain attributes that may favor particular applications. For instance, high-power super capacitors are most suitable when a large amount of power is needed for short amounts of time, such as compensating for short-duration voltage fluctuations and restarting collapsed power systems.[13] In contrast, other methods such as pumped hydro energy storage can discharge stable electrical power over much longer time scales. In mid-2017, pumped hydro accounted for approximately 96% of all stored energy.[11] However, the scalability of this technology comes into question as large bodies of water must be accessible

which also limits the potential for further reduction in system cost.[9] In addition, environmental concerns related to groundwater availability have been noted due to the volume of water necessary to maintain reservoir levels.[14]

A family of energy storage technologies that cover a wide range of applications and has shown great promise is batteries. Batteries take advantage of the ability to reversibly convert electrical energy to chemical energy through redox reactions that occur inside the cell between positive and negative electrodes. Many different battery materials and configurations exist, which give these energy storage technologies greater modularity over other choices. Current research trends focus on the development of novel, sustainable, more efficient materials, and methods for their fabrication, which forecasts lower costs, higher capacities and better performing systems. This promising outlook for continued development and cost reductions is an important factor to consider when selecting an appropriate storage technology for grid-scale use. At the moment, many battery systems struggle to penetrate the market due to high costs that limit full commercialization. Future innovations in materials used in batteries is key to supporting the successful integration of more renewable energy into the market.[15] It is important to note however that not one single technology alone could currently handle the demands of the grid to provide cheap and efficient energy storage and an effective strategy could be to use a combination of several technologies together.

1.3 Redox-Flow Batteries and Challenges for Grid Integration

Here, we will focus on one specific class of batteries that has gained significant notoriety for their attractiveness in grid-scale energy storage applications – Redox-Flow Batteries (RFBs).

A schematic of a RFB is detailed in Figure 1.3. RFBs consist of large external tanks or reservoirs which contain the positive and negative redox materials in liquid form. These are then circulated through a central cell stack where the respective redox reactions occur on inexpensive carbon-based electrodes. The positive and negative redox materials (i.e., catholyte and anolyte) are separated by a membrane whose purpose is to prevent cross contamination of the redox species while only allowing for the passage of charge-balancing ions.

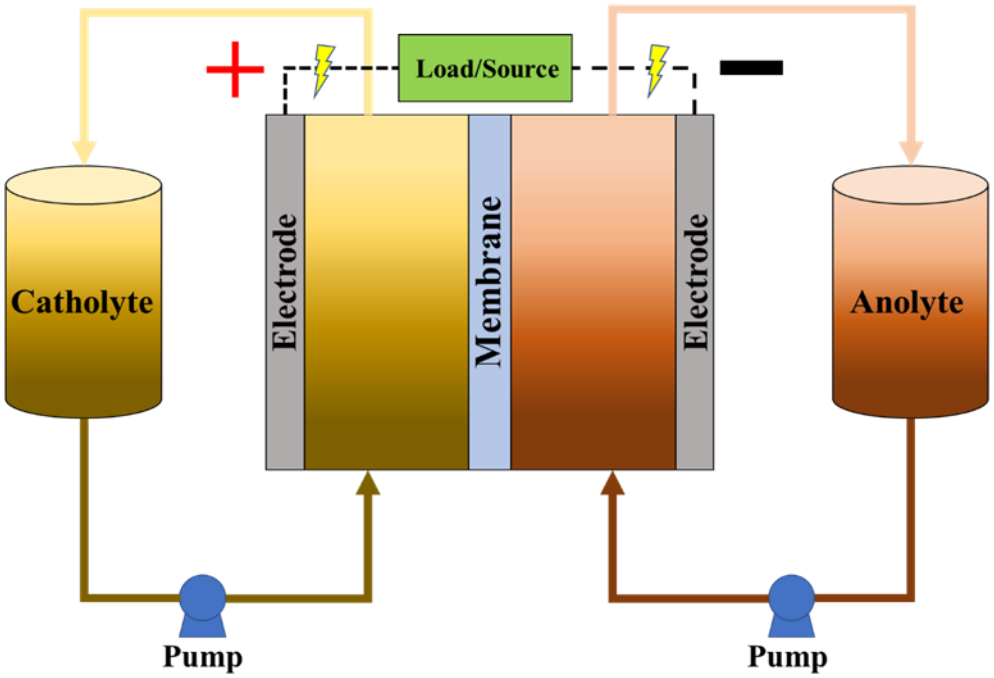

Figure 1.3. Schematic Illustration of a RFB. The RFB is distinguished by the external reservoirs which contain the liquid catholyte and anolyte solutions and are pumped through the central cell stack.

The unique advantage that RFBs possess over other types of batteries, particularly their solid-state counterparts (i.e Lithium-ion, Nickel-Metal-Hydride, etc.), is that the power and energy of the system are decoupled, allowing for a great range of scalability.[10,16] In other words, the energy of the system is dictated by the concentration or volume of the electrolyte active materials while the power is representative of the surface area of active sites in the cell. Furthermore, the choice of membranes and electrode materials must also be considered to provide sufficient power, as high resistances contributed by poorly conductive membranes and inadequate cell compression can have negative impacts. Additionally, because the electrodes of RFBs serve as only an active site for redox reactions with no intercalation of active material, they are not subjected to the same stress that electrodes from solid-state batteries undergo.[10,16,17] The complex manufacturing and closed-cell assembly of solid-state batteries is also not present, and while initial upfront capital costs tend to be higher, the low-maintenance and high service life of RFBs can reduce costs in the long run.[18] Safety is also an important consideration in which RFBs excel at, with the continuously circulating electrolyte through the cell providing an avenue for heat dissipation. These qualities make RFBs an excellent candidate for large-scale energy storage, with prototypes and near-commercial models readily being tested at the MW and MWh scales in the U.S., Japan, and Germany.[19]

To date, several different RFB chemistries have been proposed. Traditional chemistries have revolved around the use of metal ions or other elemental redox species soluble in highly acidic aqueous media, including iron, chromium, vanadium, polysulfides, bromine, cerium, manganese, and titanium.[20–24] However as the technology has progressed, more novel chemistries and classes of RFBs have been developed, including RFBs based on redox-active organic materials, and 'hybrid' or 'semi-solid' RFBs incorporating some characteristics of solid-state batteries.[25–30] Many of these advances are driven to address the challenges that RFBs face in

achieving full-grid integration and commercialization, despite the numerous qualities just mentioned. One major inhibitor is cost, as the Department of Energy has listed a target of $100 kWh for energy storage systems, with many of the most advanced RFB systems today falling short of that target, with some estimates as high as $320 kWh.[17,31,32] This high cost is a contribution of many factors but can mostly be attributed to the types of active materials used and the selection of ion-exchange membranes or porous separators. Despite the RFB's ability to decouple the power and energy of the system, compared to its solid-state competitors the energy density is quite low. Some of the highest energy density lithium-ion batteries have achieved over 600 Wh/L while current RFBs hover around a mere 40 Wh/L, which is primarily limited by the generally low solubility of the active redox species in aqueous media (~ 1-2 M).[30] Furthermore these RFBs must operate with full-cell potentials that stay within the stability window of aqueous solutions (~1.23V) to prevent electrolysis, requiring multiple cell stacks to be incorporated to meet power demands which adds more capital cost.[20] The stability of the active material is also important to ensure the long life-span of the battery, and issues with active material crossover through the membrane due to concentration gradients can be detrimental to capacity retention. To address this last issue, mixed-electrolyte solutions have been utilized to create a symmetric cell system to reduce the concentration gradients and driving forces for diffusion.[33] Indeed this avoids the actual issue at hand, whereby the selectivity of membranes in RFBs is rather poor, especially when the active materials are metal ions that may be a few angstroms in hydrated diameter, noting that for vanadium, bond distances in the hydrated state are around 2 angstroms or less.[34] To reiterate, the purpose of the membrane is to allow for the passage of charge balancing ions while keeping the active materials in their respective cell sides. While this may sound simple, it is actually quite difficult to achieve in practice. On many occasions, improving the performance of one aspect will

negatively affect the other. For example, creating membranes with a larger pore size will improve the ionic conductivity but the selectivity towards the active species will suffer. This has been the greatest challenge involved in membrane development.

The future of commercialization for RFBs will ultimately depend on innovations made at the materials level, as higher performing, cost-effective alternatives that can address these challenges are highly sought after. Consequently, as these materials become increasingly more complex, conventional methods of experimental investigation will soon become obsolete in thoroughly probing the possible design space. In this work, we present avenues for developing and investigating novel materials for RFBs, particularly, sol-gel ceramic membranes, organic redox active materials, and a new class of environmentally friendly and sustainable non-aqueous solvents. We also propose a new approach to accelerate electrochemical and physiochemical characterization of RFB materials using high-throughput experimental methods. Coupled with data-driven computational techniques for analysis and insight to inform future design considerations, this will work will aim to accelerate the advancement of RFBs for large-scale energy storage.

1.4 REFERENCES

1. Friedlingstein, P. *et al.* Global carbon budget 2019. *Earth Syst. Sci. Data* **11**, 1783–1838 (2019).
2. Friedlingstein, P. *et al.* Global Carbon Budget 2020. *Earth Syst. Sci. Data* **12**, 3269–3340 (2020).
3. IEA. *Assessing the effects of economic recoveries on global energy demand and CO2 emissions in 2021*. *Global Energy Review 2021* (2021).

4. IEA. *Renewable Energy Market Update: Outlook for 2021 and 2022*. *Renewable Energy Market Update* (2020).
5. Tollefson, J. COVID curbed carbon emissions in 2020 - but not by much. *Nature* **589**, 343 (2021).
6. IRENA. Global Energy Transformation. (2019).
7. Marlene Motyka. *2019 Renewable Energy Industry Outlook*. (2019).
8. Energy Information Administration (EIA). Short-Term Energy Outlook. *U.S. Dep. Energy* 4–6 (2021).
9. Dunn, B., Kamath, H. & Tarascon, J.-M. Electrical Energy Storage for the Grid: A Battery of Choices. *Science (80-.).* **334**, 928–935 (2011).
10. Weber, A. Z. *et al.* Redox flow batteries: A review. *J. Appl. Electrochem.* **41**, 1137–1164 (2011).
11. International Renewable Energy Agency. *ELECTRICITY STORAGE AND RENEWABLES: COSTS AND MARKETS TO 2030*. (2017).
12. Soloveichik, G. L. Battery Technologies for Large-Scale Stationary Energy Storage. *Annu. Rev. Chem. Biomol. Eng* **2**, 503–530 (2011).
13. Castro-Gutiérrez, J., Celzard, A. & Fierro, V. Energy Storage in Supercapacitors: Focus on Tannin-Derived Carbon Electrodes. *Frontiers in Materials* **7**, 217 (2020).
14. Saulsbury & James W. A Comparison of the Environmental Effects of Open-Loop and Closed-Loop Pumped Storage Hydropower HydroWIRES Initiative. (2020).
15. Larcher, D. & Tarascon, J.-M. Towards greener and more sustainable batteries for electrical energy storage. *Nat. Chem.* **7**, (2014).
16. Nguyen, T. & Savinell, R. F. Flow Batteries. *Electrochem. Soc. Interface* **19**, 54–56 (2010).
17. Wang, W. *et al.* Recent progress in redox flow battery research and development. *Adv. Funct. Mater.* **23**, 970–986 (2013).
18. Leung, P. *et al.* Progress in redox flow batteries, remaining challenges and their applications in energy storage. *RSC Adv.* **2**, 10125 (2012).
19. Sánchez-Díez, E. *et al.* Redox flow batteries: Status and perspective towards sustainable stationary energy storage. *J. Power Sources* **481**, 228804 (2021).
20. Zeng, Y. K., Zhao, T. S., An, L., Zhou, X. L. & Wei, L. A comparative study of all-vanadium and iron-chromium redox flow batteries for large-scale energy storage. *J. Power*

Sources **300**, 438–443 (2015).

21. Eckroad, S. & The Electric Power Research Institute. Vanadium Redox Flow Batteries: An In-Depth Analysis. **3**, 102 (2007).
22. Ge, S. H., Yi, B. L. & Zhang, H. M. Study of a high power density sodium polysulfide/bromine energy storage cell. *J. Appl. Electrochem.* **34**, 181–185 (2004).
23. Leung, P. K., Mohamed, M. R., Shah, A. A., Xu, Q. & Conde-Duran, M. B. A mixed acid based vanadium-cerium redox flow battery with a zero-gap serpentine architecture. *J. Power Sources* **274**, 651–658 (2015).
24. Wang, Y. Y., Lin, M. R. & Wan, C. C. A study of the discharge performance of the Ti/Fe redox flow system. *J. Power Sources* **13**, 65–74 (1984).
25. Wedege, K., Dražević, E., Konya, D. & Bentien, A. Organic Redox Species in Aqueous Flow Batteries: Redox Potentials, Chemical Stability and Solubility. *Sci. Rep.* **6**, 1–13 (2016).
26. Yang, B., Narayanan, S. R., Hoober-Burkhardt, L., Wang, F. & Surya Prakash, G. K. An Inexpensive Aqueous Flow Battery for Large-Scale Electrical Energy Storage Based on Water-Soluble Organic Redox Couples. *J. Electrochem. Soc.* **161**, A1371–A1380 (2014).
27. Petek, T. J., Hoyt, N. C., Savinell, R. F. & Wainright, J. S. Slurry electrodes for iron plating in an all-iron flow battery. *J. Power Sources* **294**, 620–626 (2015).
28. Narayanan, S. R. *et al.* A High Efficiency Iron-Chloride Redox Flow Battery for Large-Scale Energy Storage. *J. Electrochem. Soc.* **163**, A5118–A5125 (2015).
29. Li, Z. *et al.* Aqueous semi-solid flow cell: demonstration and analysis. *Phys. Chem. Chem. Phys.* **15**, 15833 (2013).
30. Duduta, M. *et al.* Semi-solid lithium rechargeable flow battery. *Adv. Energy Mater.* **1**, 511–516 (2011).
31. Wadia, C., Albertus, P. & Srinivasan, V. Resource constraints on the battery energy storage potential for grid and transportation applications. *J. Power Sources* **196**, 1593–1598 (2011).
32. Wei, X. *et al.* Materials and Systems for Organic Redox Flow Batteries: Status and Challenges. *ACS Energy Lett.* **2**, 2187–2204 (2017).
33. NASA. *NASA redox storage system development project, calendar year 1982*. *Nasa Tm-83469* **1**, (1983).
34. Krakowiak, J., Lundberg, D. & Persson, I. A coordination chemistry study of hydrated and

solvated cationic vanadium ions in oxidation states +III, +IV, and +V in solution and solid state. *Inorg. Chem.* **51**, 9598–9609 (2012).

Chapter 2. OVERVIEW OF KEY EXPERIMENTAL METHODS AND TECHNIQUES

2.1 ELECTROCHEMICAL TECHNIQUES

2.1.1 *Cyclic Voltammetry*

One of the first steps in investigating a new active material for use in secondary battery systems is to characterize its chemical and electrochemical reversibility. Chemical reversibility refers to the stability of the active material, which must be able to oxidize and reduce repeatedly as secondary batteries are expected to perform thousands of charge-discharge cycles.[1] The electrochemical reversibility is a description of the electron transfer kinetics of the reaction, where a low barrier to electron transfer in the reaction will ensure that the charge transfer is fast relative to the mass transfer.[2] One of the most powerful and commonly used electrochemical techniques to characterize the reversibility of an active material is Cyclic Voltammetry (CV).

In a typical CV experiment, a poteniostat or some other power source applies a potential to a working electrode relative to the potential of a reference electrode, of which it's potential is stable and known. This potential, positive or negative, modulates the energy of the electrons in the electrode. In a case where a more negative potential is applied, the electrons in the electrode are at a higher energy level than the lowest unoccupied molecular orbital (LUMO) of an active species in solution, causing a driving force for the electron to transfer to the species (reduction).[3,4] The opposite process (oxidation) occurs when a positive potential is applied to the electrode. A visual representation of this process is illustrated in Figure 2.1.

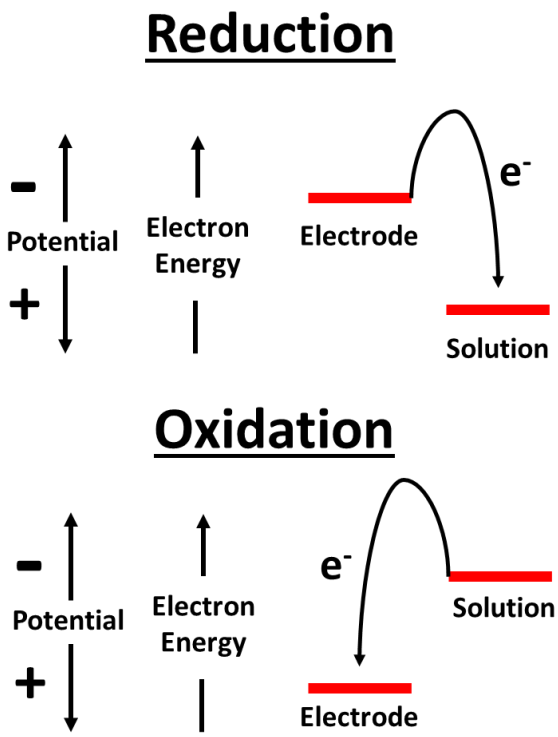

Figure 2.1. Energy diagram of oxidation and reduction reactions at electrodes.

Equilibrium between the oxidized and reduced species formed in CV experiments can be well described by equation 2.1, known as the Nernst Equation.

$$\mathrm{E} = E^{o} + \frac{rT}{nF} ln \frac{(C_{Ox})}{(C_{Red})} \qquad (2.1)$$

In the Nernst Equation, E is the cell potential, E^0 is the standard potential of the species, r is the universal gas constant (8.315 J mol^{-1} K^{-1}), T is the absolute temperature in Kelvin, n is the number of electrons transferred, F is Farraday's constant (96,485 C mol^{-1}), and C_{Ox} and C_{Red} refer to the concentration of the oxidized and reduced species at the surface of the electrode,

respectively. The concentrations of the oxidized and reduced species at the electrode will change as different potentials are applied during the experiment, as outlined in the process in Figure 2.1. Hence, the Nernst equation allows us to find the approximate concentration of both species at any potential, and in an ideal electrochemically reversible reaction, these changes occur almost instantly, which maintains electrochemical equilibrium of the system. A fast electron transfer process is what ensures that equilibrium is maintained. The experimental setup for a CV experiment is illustrated in Figure 2.2, where we use as an example the reversible redox couple between ferrocyanide and ferricyanide in equation 2.2.

$$[\mathrm{Fe(CN)_6}]^{4-} \rightleftarrows [\mathrm{Fe(CN)_6}]^{3-} + e^{-} \qquad (2.2)$$

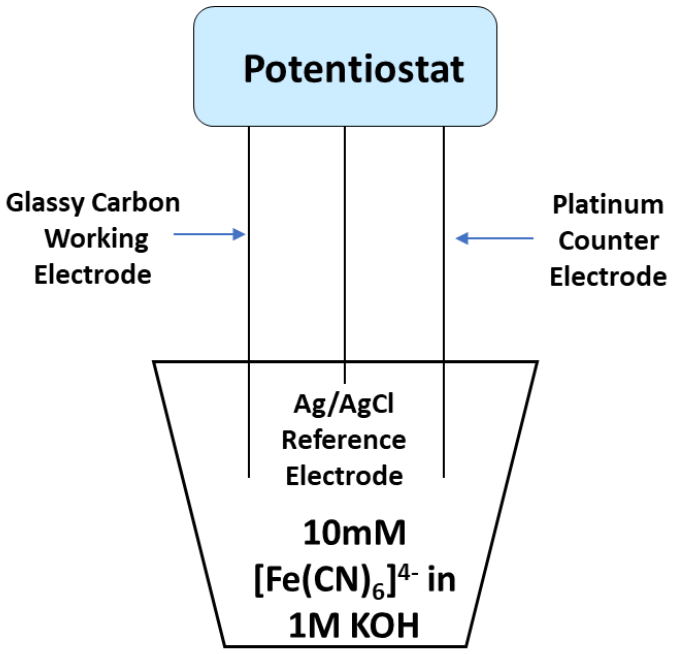

Figure 2.2. Experimental setup for cyclic voltammetry.

The electrochemical cell consists of a three-electrode design immersed in a solution of the ferrocyanide with 1M potassium hydroxide (KOH) as the supporting electrolyte. A supporting electrolyte is necessary to enhance the conductivity of the solution, and thereby minimizes the ohmic drop due to overpotential, which can significantly affect measurements. The three types of electrodes used in cyclic voltammetry are the working, reference, and counter electrodes. The working electrode is the electrode at which the electrochemical reaction of interest is occurring. It is important to polish this electrode after each experiment to ensure a clean electrode surface and prevent residues from previous measurements affecting the current one. The potential at this electrode is monitored relative to a reference electrode, which is an electrode of known potential where, ideally, the passage of current through the electrodes will not affect its reference potential.[5] Thus, the potential difference in the experiment is always measured between the working and reference electrodes. The counter electrode, also known as an auxiliary electrode, completes the electric circuit of the system. It is best to use counter electrodes that are inert to any electrochemical reactions that may occur, so that no undesired reactants make their way to the working electrode during the experiment. The specific electrodes used in this example experiment were a glassy carbon working electrode, a silver/silver chloride reference electrode, and a platinum counter electrode.

The result of this experiment gives the characteristic 'duck curve' voltammogram of the ferro-ferricyanide reaction in Figure 2.3. The potential is first swept in the positive direction, producing an anodic (oxidation) current where the ferrocyanide is oxidized to ferricyanide in the first peak. At a set potential chosen by the researcher, the signal is reversed and swept in the negative direction, producing a cathodic (reduction) current where the ferricyanide is reduced back to ferrocyanide at the second peak

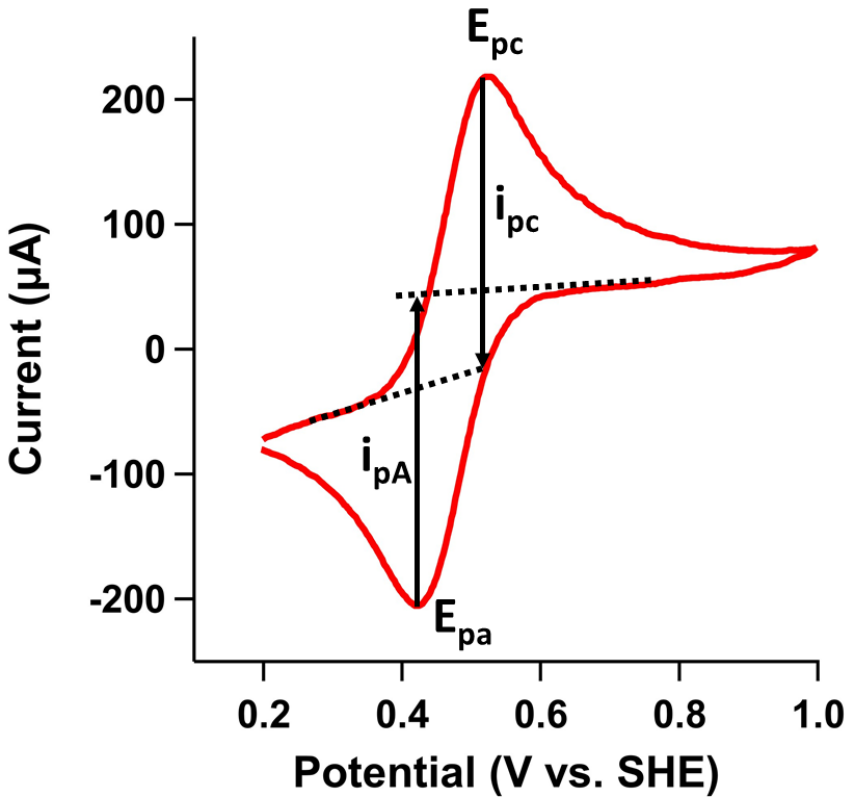

Figure 2.3. Cyclic voltammogram of the ferro/ferricyanide redox couple in 1M KOH.

When characterizing the reversibility of a CV, two important values are considered which is the peak potential difference, ΔE_p, and the ratio of the peak anodic and cathodic currents, i_{pA}/i_{pC}. For an electrochemically reversible reaction at 25ºC, the ΔE_p should be near 58/n mV, which is the theoretical value in a fully reversible system, where n is the number of electrons involved in the reaction (i.e. 1 for ferro-ferricyanide couple).[6] Deviations from this value will suggest that the electron transfer is slower than ideal. In addition, from these peak potentials, the redox potential E^o may be found, which lies at the halfway point between the peak potentials. The redox potential is important in characterizing the material's overall reducing or oxidizing capacity.[7] In other words, the redox potential of a material will indicate that materials affinity for either gaining or losing

electrons. Materials with higher redox potentials have a greater affinity for electrons, and which case are more likely to be reduced. In the opposite scenario, lower redox potential materials have less affinity for electrons and tend to be oxidized. For a chemically reversible reaction, the peak current ratio should be equal to 1.[3] Since currents are produced by the reactions that occur at the electrodes, the peak current produced by the oxidation of a species should ideally be the same for the peak current produced by the subsequent reduction of that same species. Significant deviations from unity may imply that an irreversible chemical reaction is occurring during the experiment, decreasing the number of species available for repeated oxidation and reduction. Frequently, these adverse chemical reactions will consume the species that have just been reduced or oxidized, causing the irreversibility on the reverse scan of the experiment. While more in-depth analysis can be performed with CV data, these basic characterizations here give adequate information to assess the potential for the use of materials in secondary batteries. However, the use of CV is not only limited to active materials but can also be applied to assess the stability of supporting electrolytes. This application will be discussed further in this chapter and subsequent chapters.

2.1.2 *Impedance Spectroscopy*

Electrochemical impedance spectroscopy (EIS) is a powerful technique that has been utilized across many fields for a wide array of applications, including but not limited to, battery performance, corrosion testing, biosensors, and non-invasive characterization of cell cultures .[8–11] While most of the important phenomena of interest for these applications can be investigated using more direct analytical methods, they are often slow and inefficient.[12] Using EIS to analyze these inherently electrochemical processes can greatly speed up the time frame of the experiment while still providing good accuracy. In contrast to other electrochemical measurements that push the

electrode far from its equilibrium via potential (or current) steps and sweeps, EIS applies a vanishingly small sinusoidal perturbation to the system and the resulting response to that perturbation is observed.[5] Here, we will be concerned mostly with using EIS to obtain effective resistances from membranes and electrolytes.

The impedance can be regarded as a 'generalized' electrochemical resistance, identical in that it defines the ability of circuit to resist the flow of electrical current, however not constrained by the limitation of Ohm's law to ideal resistors.[13] If a small sinusoidal potential signal (equation 2.3) is applied to perturb an electrochemical system, then its response in the 'linear regime' will also be a sinusoidal current (equation 2.4) but with an added phase shift (ϕ).

$$E_t = E_0 \sin(\omega t) \tag{2.3}$$

$$I_t = I_0 \sin(\omega t + \phi) \tag{2.4}$$

In equations 2.3 and 2.4 above, E_t is the potential at time t, I_t is the current response at time t, E_0 and I_0 are the amplitudes of the potential and current, ω is the radial frequency, and ϕ is the phase shift in radians. With these two expressions, we obtain an equation analogous to Ohm's law for a generalized impedance, Z.

$$Z = \frac{E_t}{I_t} = Z_0 \frac{\sin(\omega t)}{\sin(\omega t + \phi)} \tag{2.5}$$

However, since the impedance is a vector with a particular phase shift, it is typically resolved into its real and imaginary components.[5,14]

$$Z(\omega) = Z_{Re} - jZ_{Im} \quad (2.6)$$

Both the real (Z_{Real}) and imaginary (Z_{Imag}) components of the impedance are functions of the frequency. These impedances are most popularly displayed with a Nyquist plot, which plots the real impedance on the x-axis and the imaginary impedance on the y, with each impedance data point representing a measurement taken at an individual frequency. Figure 2.4 shows a Nyquist plot of a fully assembled RFB cell after performing EIS from 10Hz-300kHz.

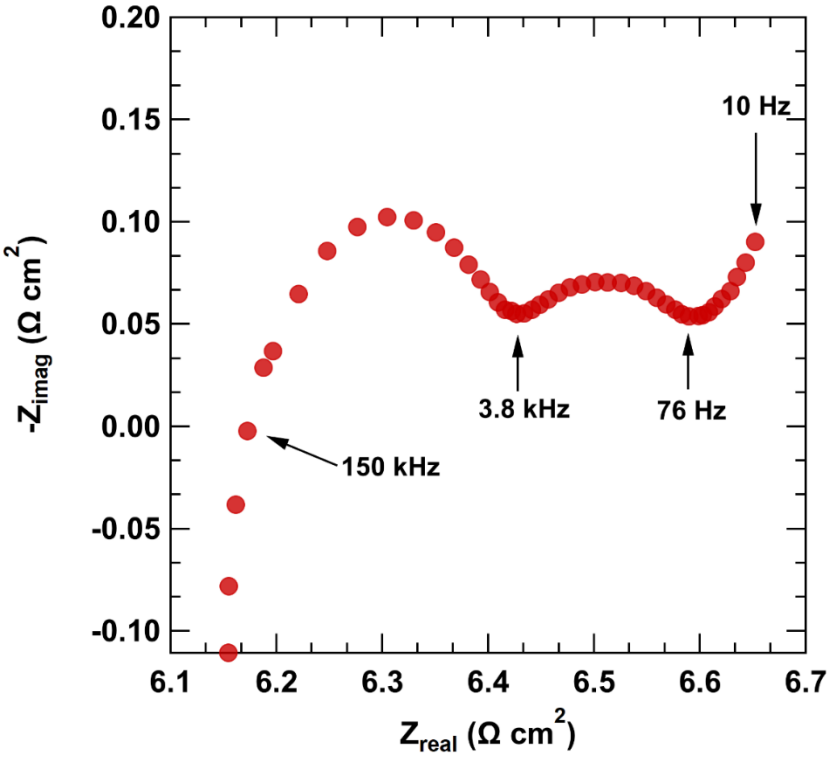

Figure 2.4. Impedance spectroscopy of a full-cell RFB.

Much information can be obtained from Nyquist plots of full electrochemical systems such as this. Particularly, the series of semicircles ending at 3.8kHz and 76Hz give information about charge transfer resistances from the redox reactions occurring in the cell. Other features, such as the 'tail' observed after 76Hz up to 10Hz give information about resistances related to the diffusion of the species. Typically, the mass transfer controlled regions of the spectra are found at low frequencies while the kinetically controlled regions are found at high frequencies.[15]

In addition to performing EIS on full electrochemical cells, it is often advantageous to also investigate the elements of the RFB cell individually, such as the membrane or the electrolyte solutions. Using a 4-electrode experimental setup as shown in Figure 2.5, impedance spectra of the bare electrolyte solution and solution plus the membrane can also be taken. This unconventional configuration is ideal for this application, as the Lugin capillaries can measure currents extremely close to the membrane and position the electrodes at the exact place of interest, which in this application is the membrane. With one Lugin capillary belonging to the reference electrode and the other belonging to the working electrode, placing both capillaries immediately near the membrane also allows for the reference electrode to be near the working, yet also being able to avoid adverse effects from ohmic drops in the electrolyte.

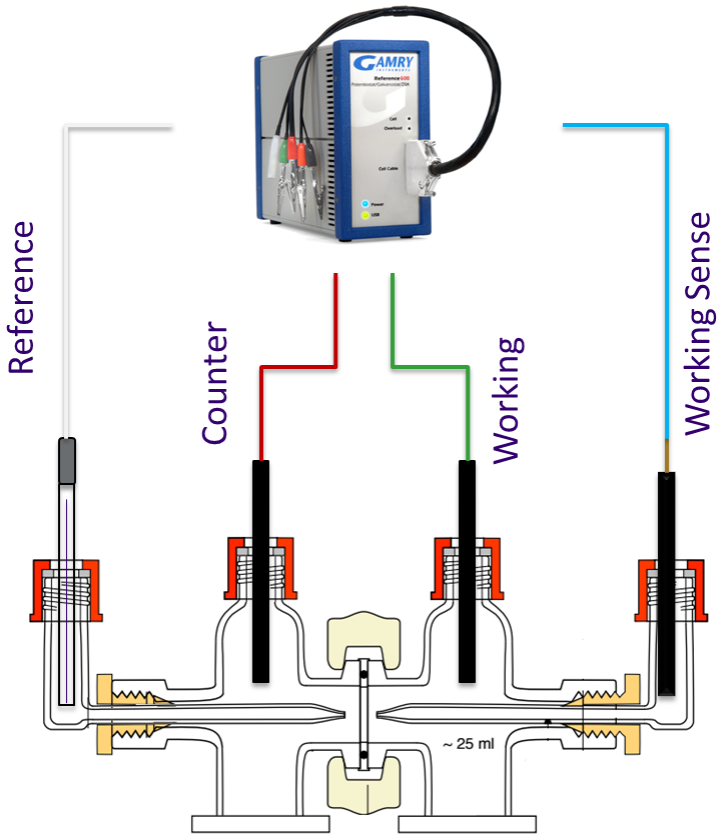

Figure 2.5. Experimental setup for 4-electrode impedance spectroscopy of membranes.

Figure 2.6 shows a Nyquist plot of EIS data from a 3M Hydrochloric acid (HCl) solution and a Nafion 212 membrane using the 4-electrode setup of Figure 2.5. The experiment is performed twice, once without the membrane and once with the membrane. Note that the shape of these plots is rather different than what is shown in Figure 2.4. Since there is no redox active material contained here, and only a supporting electrolyte, we would not expect to see features that would correlate with that. The specific part of the curve we are most concerned with is the high frequency portion where the curve intersects with the zero axis of the imaginary impedance. At this point, only the pure ohmic resistance of the system is observed.[16] When the resistance with

the electrolyte solution plus Nafion 212 membrane ($R_{membrane}$) is subtracted from the measurement with only the electrolyte ($R_{electrolyte}$) and multiplied by the exposed area, A, the effective area specific resistance (ASR) of the membrane in ohms cm^2 be obtained.

$$ASR = \left(R_{membrane} - R_{electrolyte}\right) * A \tag{2.7}$$

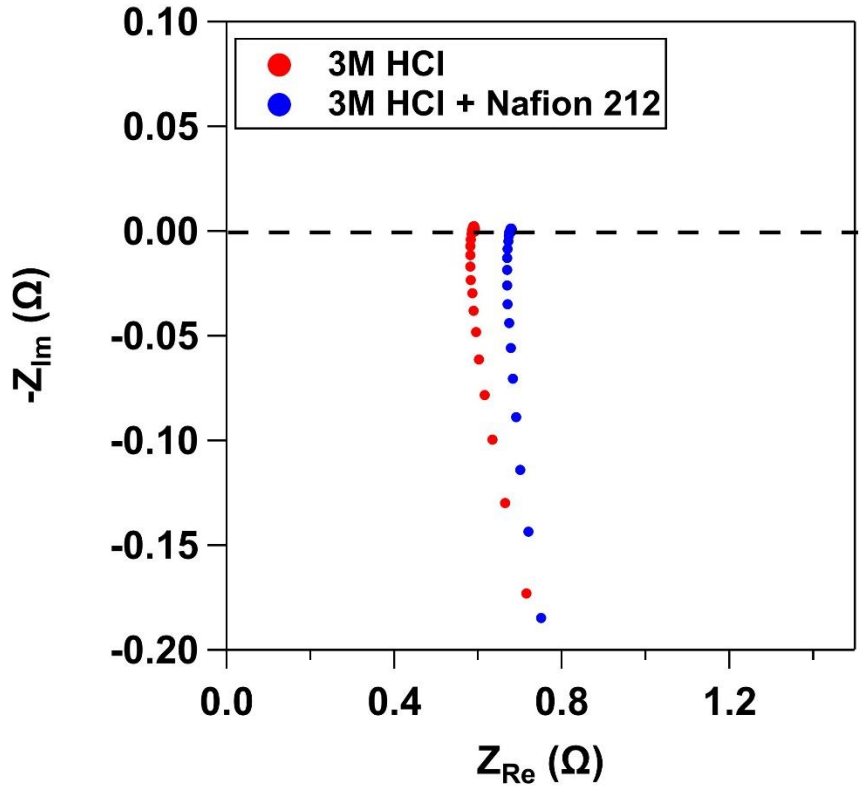

Figure 2.6. Nyquist plot generated from 3-eelctrode impedance spectroscopy.

2.1.3 *Chronopotentiometry*

Chronopotentiometry (CP) is a galvanostatic electrochemical technique in which a constant controlled current is applied to an electrochemical cell and the potential is recorded as a function

of time.[5,17] The potential at the working electrode will adjust to a value in which the flux of active species in the reaction is sufficient enough to sustain the current.[18] Multiple steps with various constant currents can be applied to investigate the effect on the resulting potentials. CP is typically applied towards studying various reaction mechanisms and kinetics, including notable applications such as measurement of antioxidant activity, rates of electrodeposition, and species diffusion coefficients.[19–21] While the systems investigated usually involve some specific electroactive material or species, it is also possible to assess the stability window of supporting electrolytes without redox species, as has been demonstrated recently.[22,23] Whereas previously when active materials were investigated, the potential would be dictated by the flux of the electrochemical reaction from the redox species, now the potential would be dictated by a flux caused by the electrochemical degradation of the supporting electrolyte. By applying multiple steps of anodic (positive) and cathodic (negative) currents, it is possible to probe the electrochemical degradation of a supporting electrolyte at both extremes. In standard aqueous based electrolytes, these would coincide with the oxygen evolution reaction (OER) at positive potentials and the hydrogen evolution reaction (HER) at negative potentials. When applying this technique towards non-aqueous electrolytes, the actual mechanism of the degradation reactions may not be known, however gaining insight on where the potential limits for these reactions occur is still extremely valuable to determine. Figure 2.7 demonstrates a CP experiment applied towards a 1M KOH electrolyte solution. A series of anodic currents were applied in steps, specifically, 1mA, 0.75mA, and 0.5mA. These steps were then repeated but at negative currents to probe the cathodic region of electrolyte stability.

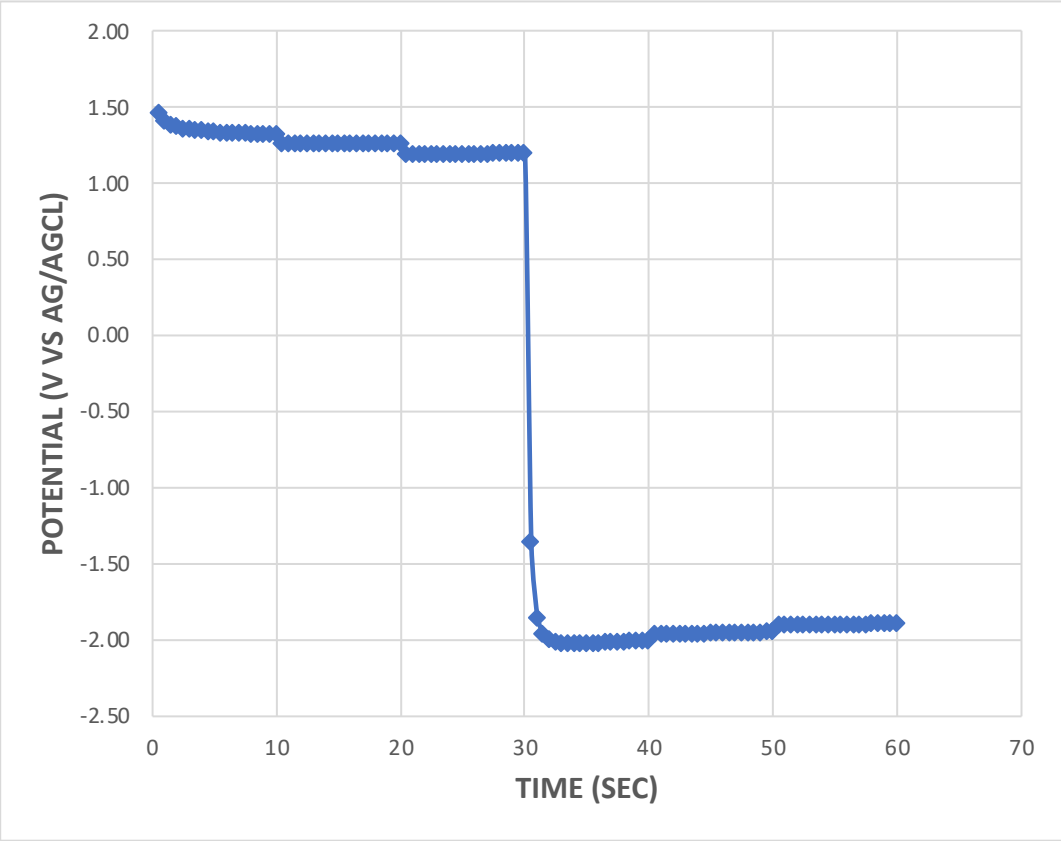

Figure 2.7. Multi-step CP experiment on 1M KOH.

To obtain the limiting cathodic and anodic potentials for the electrolyte solution, a slope extrapolation method is utilized. For each current step, the potentials are averaged over the last two seconds of the measurement, as the potentials will equilibrate over time. These potentials are then plotted against the corresponding current densities, and a line of best fit is then extrapolated to the line of zero current. The intersection at the line of zero current indicates the estimated anodic and cathodic limiting potentials for the electrolyte and is found by taking each of the equations and setting the current, y, equal to zero and solving for the potential, x, as demonstrated in Figure 2.8 below for the 1M KOH solution. The positive and negative potential limits determined by CP

are approximately 1.08 V and -1.78 V, respectively, which match up quite well for potential limits of 1M KOH solutions determined using CV.[24]

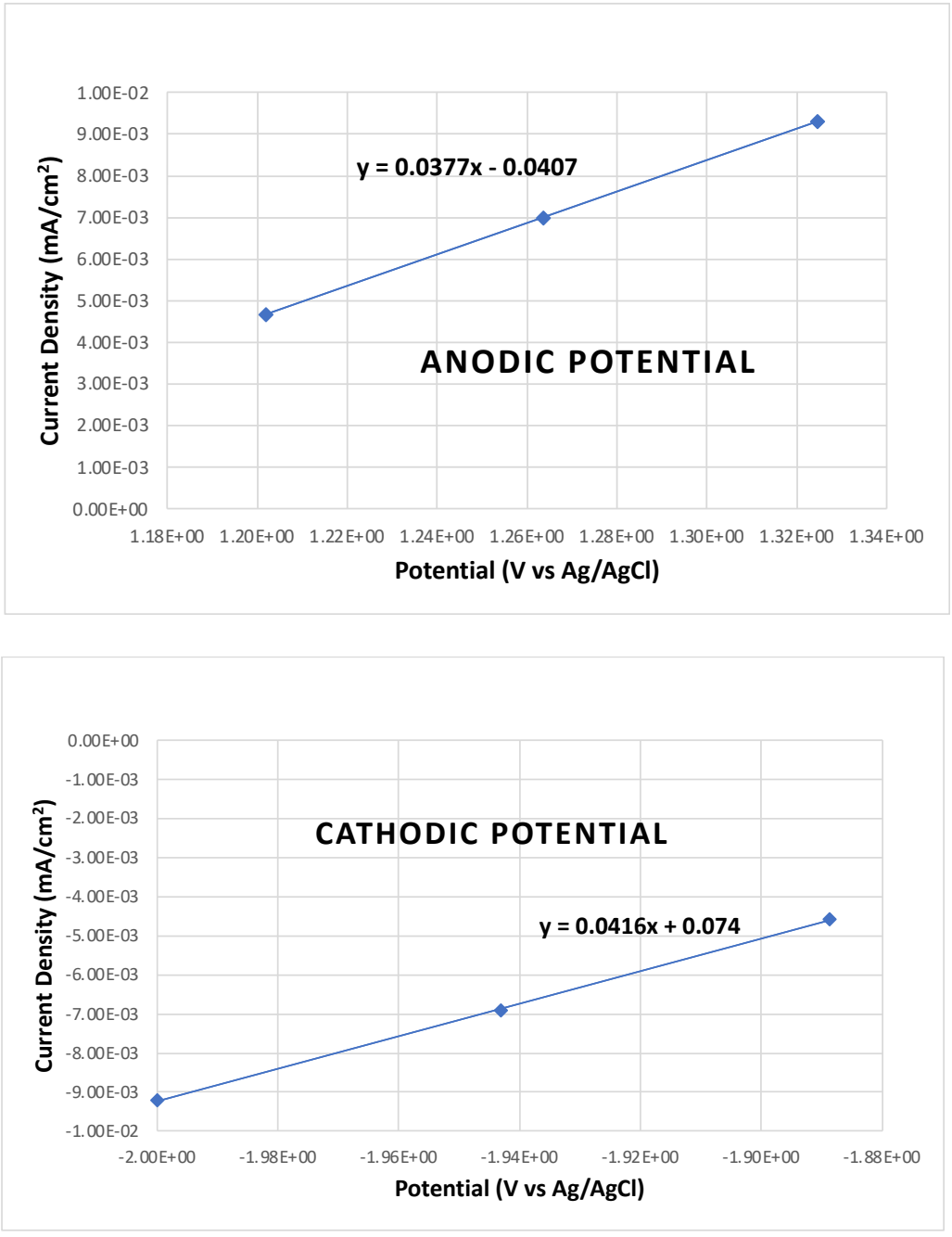

Figure 2.8. Slope extrapolation method for limiting potentials. Top: Anodic potential limit extrapolation. Bottom: Cathodic potential limit extrapolation.

2.1.4 *Full-Cell RFB Measurements*

Figure 2.9. Image of full-cell RFB during charge-discharge operation.

After individual RFB components have been screened and tested via specific electrochemical techniques, it is important to assess the performance of the system in its full cell configuration. Testing of a small-scale RFB model is a crucial step in probing the candidacy of a particular redox couple or hardware configuration to succeed if scaled-up to the grid-scale level. Perhaps the most important full-cell measurement that can be performed is a charge-discharge experiment using a battery cycler or analyzer. Figure 2.9 shows an image of a full-cell RFB during

a charge-discharge experiment. The cell is noted in the center of the frame, where the two reservoirs containing the electrolytes and active materials on opposite sides. These solutions are circulated through the cell by a peristaltic pump, and electrical connections from the cell to a potentiostat are made to carry out the electrochemical cycling. These experiments are typically performed by setting a constant current, for charging and discharging the system, between voltage limits that specify when the current must be reversed. Representative voltage vs. time curves from a charge-discharge experiment of a RFB along with efficiencies during that time is shown in Figure 2.10, where a 0.1M anthraquinone sulfonate concentration was used as the anolyte and 0.1M ferrocyanide concentration as the catholyte, both in a 5M urea + 0.1M NaCl supporting electrolyte.

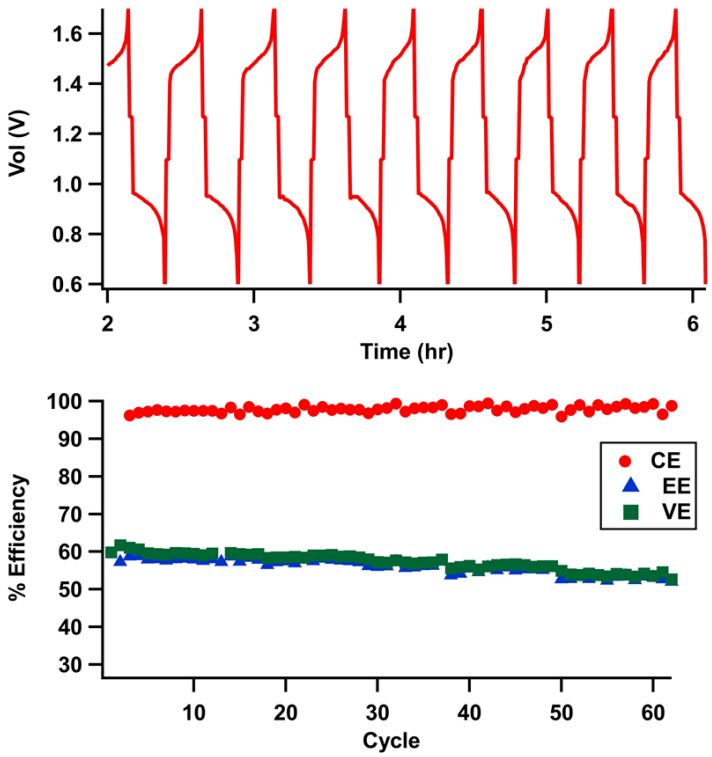

Figure 2.10. Top: Voltage vs. time curves of a constant-current charge-discharge experiment. Bottom: Efficiencies from charge-discharge experiment.

The three efficiencies that are used to characterize the charge-discharge performance of a RFB are the coulombic efficiency (CE), energy efficiency (EE), and the voltaic efficiency (VE).[25] The coulombic efficiency is the ratio of the amount of charge passed during the discharge step, $Q_{discharge}$, to the amount of charge passed during charging steps, Q_{charge}. The energy efficiency is the ratio of the integrals of the discharge power, $P_{discharge}$, and charging power, P_{charge}, with respect to time. Finally, the voltaic efficiency is the ratio of the energy and coulombic efficiency.

$$CE = \frac{Q_{discharge}}{Q_{charge}} * 100\% \tag{2.8}$$

$$EE = \frac{\int P_{discharge} dt}{\int P_{charge} dt} * 100\% \tag{2.9}$$

$$VE = \frac{EE}{CE} * 100\% \tag{2.10}$$

In addition to these efficiencies, the theoretical values for charge capacity and energy density of the RFB can be calculated prior to performing charge-discharge cycling. These can then be compared with the actual capacities obtained in experiments. The charge capacity is equal to the concentration of the limiting active material, $[C_{active}]$, in mol L^{-1}, multiplied by the number of electrons involved in the electrochemical reaction, n, and Faraday's constant, F, in Ah mol^{-1}. The energy density is then found by multiplying the charge capacity by the open circuit voltage, OCV, of the RFB.

$$charge\ capacity\ (Ah\ L^{-1}) = C * n * F \tag{2.11}$$

$$energy\ density\ (Wh\ L^{-1}) = charge\ capacity * OCV \tag{2.12}$$

2.2 Small and Wide-Angle Scattering

Small and wide-angle scattering techniques are a powerful way to probe structural and molecular characteristics in a non-destructive manner. In addition, scattering can provide information across a variety of length-scales ranging from atomic to micrometer. Small-angle scattering typically provides information from 1nm to 200 nm, and wide-angle scattering (sometimes used interchangeably with diffraction) can further probe smaller structures, particularly crystalline ones.[26,27] In this thesis, we will be mostly concerned with utilizing scattering to probe structural information of membranes and micellar formations of redox materials in electrolyte solutions. Nonetheless, scattering has been a popular choice for many areas, such as protein research, biomaterials, colloidal systems, and polymers.[28–31]

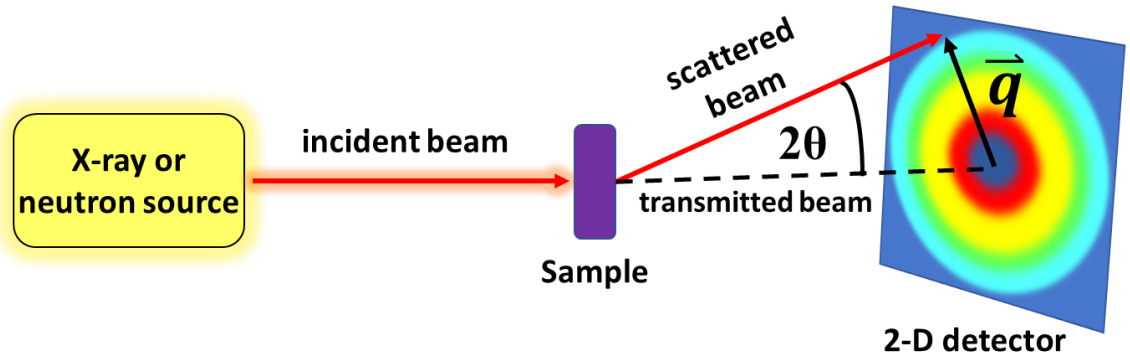

Figure 2.11. Diagram of x-ray and neutron scattering.

Figure 2.11 above shows an illustration of a generalized scattering experiment. An incident beam from a source, either x-ray or neutrons, is monochromated to a specific wavelength (λ), collimated to form a parallel non-divergent beam and directed towards the sample of interest. Most of this incident beam will simply be transmitted through the sample or absorbed, but a fraction of

the beam will specifically interact with the sample and scatter at an angle of 2θ.[32] The resulting scattering vector, *q*, and scattering intensity *I* as a function of angle, is then captured on a 2-D detector. The intensity is then averaged and plotted as a function of the scattering vector (q), which is proportional to the scattering angle (θ) and is calculated from equation 2.13.

$$q = 4\pi \frac{\sin(\theta)}{\lambda} \tag{2.13}$$

Bragg's Law also provides an avenue for the interpretation of features in the intensity that occur at specific values of the scattering vector. For example, intense scattering would occur at Bragg's angles if there is a periodic spacing *d* present in the structure of the sample of interest.[26] This is useful in cases where defined peaks are present to estimate particle sizes or pore sizes, most notably in wide-angle scattering, and equation 2.14 can be used to interpret that spacing or distance observed at a particular value of q.

$$q = \frac{2\pi}{d} \tag{2.14}$$

While the theory used for the interpretation of x-ray and neutron scattering data is based on the same principles, there are key distinctions between the two that should be discussed. X-rays interact with the electron clouds of atoms while neutrons interact with the nucleus.[33] Because of this, neutrons are able to penetrate much deeper into a sample than x-rays do, allowing for the possibility of complex *in-situ* apparatuses that result in minimal loss of energy.[34] Interestingly, while the scattering length is proportional to the atomic number for x-rays, the scattering length for neutrons do not show a direct proportionality with respect to the type of nucleus. Indeed, these values can vary drastically, most notably in the scattering lengths for the nuclei of hydrogen and deuterium which are $-3.74*10^{-15}$ m and $6.67*10^{-15}$ m, respectively.[32] This characteristic gives a

unique ability to isolate specific portions of a particle by contrast matching which varies ratios of hydrogen and deuterium in a sample. While this is a significant advantage for neutrons scattering, both techniques are invaluable for structural characterization in a wide variety of applications.

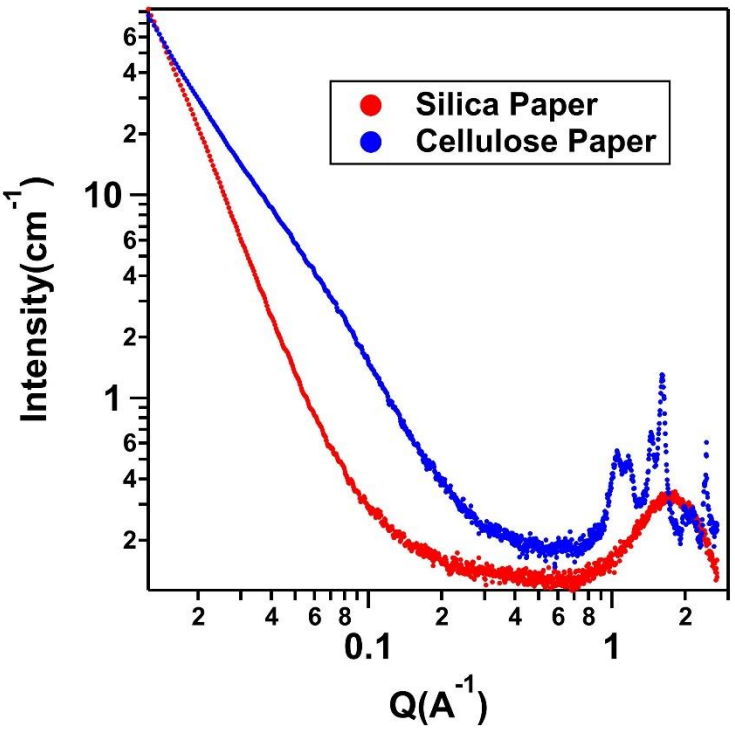

Figure 2.12. SWAXS of silica and cellulose paper substrates.

A typical representation of a scattering plot is seen in Figure 2.12 above, with the intensity of the scattered beam *I* on the y-axis and the scattering vector *q* on the x-axis. Shown is a combined small-angle x-ray scattering (SAXS) and wide-angle x-ray scattering (WAXS) of silica and cellulose paper substrates used for ceramic membrane fabrication. This combined small + wide angle x-ray scattering (SWAXS) approach is useful in obtaining complimentary information from both length scales, with the small-angle portion found in the low q region and the wide-angle

portion at high q.[35] In the SAXS region, the scattering intensities of both substrates are rather similar but vary in slope as they reach higher q values. While no other discernable features are seen in this region, the WAXS region shows distinct peaks for both samples. The structure of the cellulose paper is clearly crystalline in nature due to the sharp jagged peaks present, while the silica paper instead has a single broad peak. More applications of SWAXS to RFB membrane and micellar electrolyte structures using small-angle neutron scattering (SANS) will be introduced.

2.3 Membrane Permeability Determination

Characterization of membranes via their permeability towards certain species in electrolyte provides insight into their performance under full-cell conditions. Permeability measurements are usually performed in some sort of dual compartment static cell, such as an H-cell, where two solutions with a varying concentration gradient are separated by a membrane. Permeabilities of the species through the membrane will depend on several factors, including the pore sizes of the membrane relative to the size of the permeating species. In addition, the nature of the membrane itself may further enhance or inhibit permeability. Ion-exchange membranes contain surface charges that would prevent the passage of oppositely charged ions. Uncharged porous membranes operating on size exclusion effects (sometimes referred to as 'separators') lack charge exclusion but are still useful in several applications. An ideal membrane design would incorporate both size and charge exclusion for maximum selectivity, which in other words describes the ability of a membrane to exclude the passage of particles, ions, molecules, etc.

Figure 2.13 shows a schematic of an H-cell used for permeability experiments. Compartment 1 of the H-cell contains a solution of active material and supporting electrolyte. Compartment 2 only contains supporting electrolyte, which creates a concentration gradient for

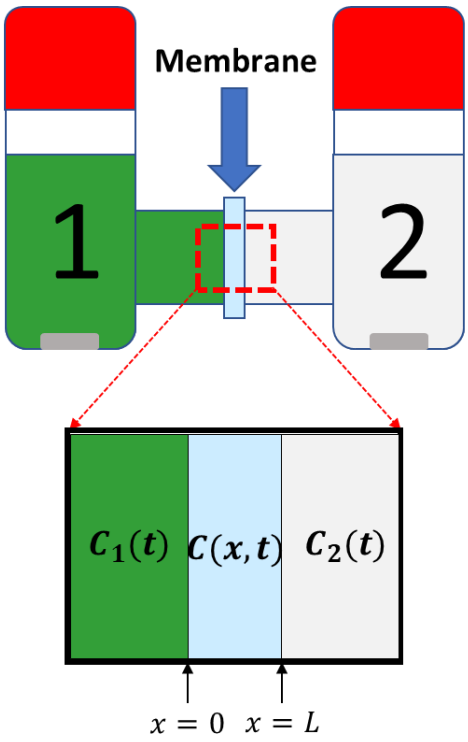

Figure 2.13. Schematic of H-cell for permeability experiments.

diffusion of the active material across the membrane in the center. Additional supporting electrolyte may sometimes be added to compartment 2 to match the ionic strength of compartment 1 and prevent significant water crossover. Modeling this system as a pseudosteady diffusion approximation based on Fick's law, we obtain an expression for the concentration, C_2, at a time, t,

$$C_2(t) = \frac{C_0}{2}(1 - e^{\frac{-t}{t_p}}) \qquad (2.15)$$

where C_0 is the initial concentration in compartment 1 at time zero and t_p is the process time scale.[36] The process time scale can be found by the rate of change in concentration in compartment 2 over time, and plugged in to equation 2.16 below to calculate the permeability, P, where A is the

exposed membrane area, V is the volume of the solutions in the compartments, and L is the thickness of the membrane.

$$P = \frac{VL}{2At_p} \tag{2.16}$$

Prior to performing the experiment, a series of dilutions of known concentration are measured for their absorbance using an Ultraviolet-visible (UV-vis) spectrophotometer. A calibration curve can then be made to find the extinction coefficient, ε, from Beer's law,

$$A = \varepsilon l C \tag{2.17}$$

where A is the absorbance, l is the pathlength of light from the cuvette cell, and C is the known concentration. Once the extinction coefficient for a particular species is found, the concentration of aliquots taken from the receiving compartment in the H-cell over time can be found and used to determine the process time constant and the permeability. Absorbance curves can be seen below in Figure 2.14 for potassium ferrocyanide in 1M KOH electrolyte, with the resulting calibration curve for peaks obtained at 325 nm. Lastly, figure 2.15 shows the results of a permeability experiment where the Fe3+ concentration is plotted as a function of time.

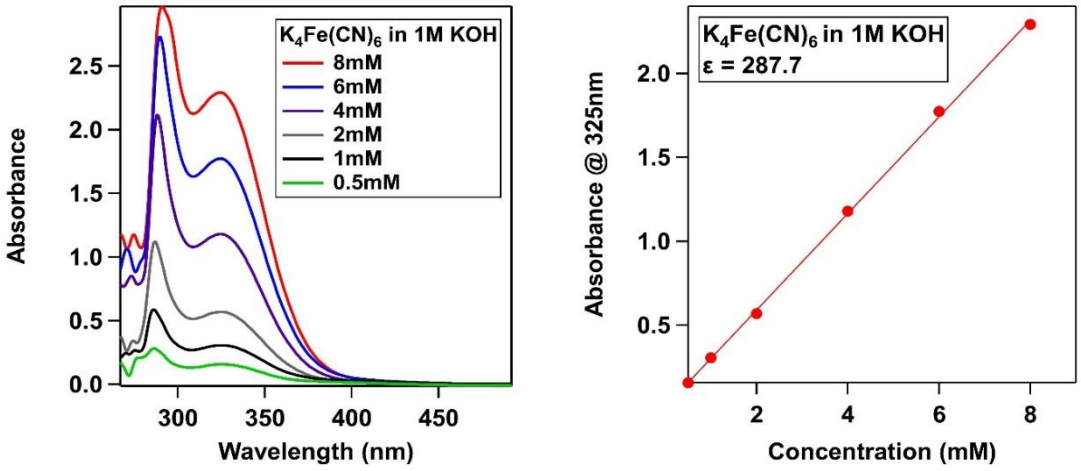

Figure 2.14. Left: Absorbance spectra of ferrocyanide in 1M KOH. Right: Calibration curve.

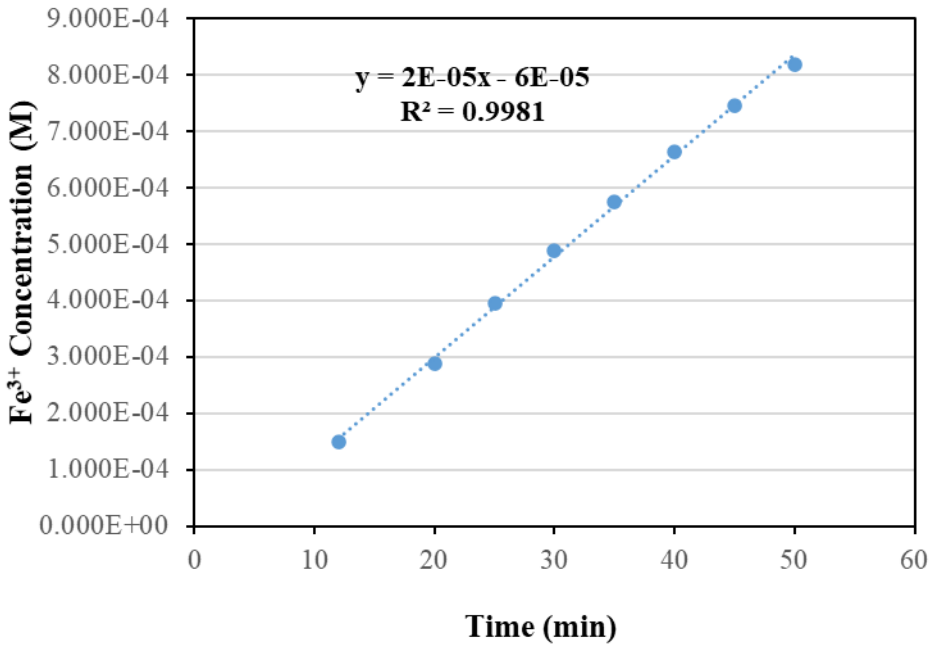

Figure 2.15. Concentration vs. time plot of permeability experiment with Fe^{3+}.

2.4 REFERENCES

1. Scherson, D. A. & Palencsár, A. The Electrochemical Society Interface • Spring 2006 Batteries and Electrochemical Capacitors. *Electrochem. Soc.* pp 17--22 (2006).
2. Klingler, R. J. & Kochi, J. K. Electron-transfer kinetics from cyclic voltammetry. Quantitative description of electrochemical reversibility. *J. Phys. Chem.* **85**, 1731–1741 (1981).
3. Elgrishi, N. *et al.* A Practical Beginner's Guide to Cyclic Voltammetry. *J. Chem. Educ.* **95**, 197–206 (2018).
4. Compton, R. G. *Understanding Voltammetry*. (Imperial College Press, 2011).
5. Bard, A. J. *et al. ELECTROCHEMICAL METHODS Fundamentals and Applications*. *Electrochemistry. I. Faulkner, Larry R* (2001). doi:10.1016/B978-0-12-381373-2.00056-9
6. Mabbott, G. A. An introduction to cyclic voltammetry. *Journal of Chemical Education* **60**, 697–702 (1983).
7. Søndergaard, M. Redox Potential. in *Encyclopedia of Inland Waters* 852–859 (Academic Press, 2009). doi:10.1016/B978-012370626-3.00115-0
8. Murbach, M. D. & Schwartz, D. T. Analysis of Li-Ion Battery Electrochemical Impedance Spectroscopy Data: An Easy-to-Implement Approach for Physics-Based Parameter Estimation Using an Open-Source Tool. *J. Electrochem. Soc.* **165**, A297–A304 (2018).
9. Deffo Ayagou, M. D. *et al.* Electrochemical impedance spectroscopy of iron corrosion in H2S solutions. *Electrochim. Acta* **282**, 775–783 (2018).
10. Honeychurch, K. C. Printed thick-film biosensors. in *Printed Films: Materials Science and Applications in Sensors, Electronics and Photonics* 366–409 (Woodhead Publishing, 2012). doi:10.1533/9780857096210.2.366
11. Price, D. T. MEMS and electrical impedance spectroscopy (EIS) for non-invasive measurement of cells. in *MEMS for Biomedical Applications* 97–119 (Woodhead Publishing, 2012). doi:10.1533/9780857096272.2.97
12. Cogger, N. D. & Evans, N. J. *An introduction to electrochemical impedance measurement*. *Solarton Ltd., Farnborough, UK* (1999).
13. Gamry Instruments. Basics of Electrochemical Impedance Spectroscopy. (2006).
14. Bockris, J., Reddy, A. & Gamboa-Aldeco, M. *Modern Electrochemistry : Fundamentals of*

Electrodiscs. (KLUWER ACADEMIC PUBLISHERS, 2002).

15. Orazem, M. E. & Tribollet, B. *Electrochemcial Impedance Spectroscopy*. (2008).
16. Yang, R. *et al*. Nonionic zeolite membrane as potential ion separator in redox-flow battery. *J. Memb. Sci.* **450**, 12–17 (2014).
17. Lingane, P. J. & Peters, D. G. Chronopotentiometry. *Crit. Rev. Anal. Chem.* **1**, 587–634 (1971).
18. Zoski, C. G. *Handbook of Electrochemistry*. (Elsevier, 2007).
19. Kinyua Muthuri, L., Nagy, L. & Nagy, G. Chronopotentiometric method for assessing antioxidant activity: A reagentless measuring technique. *Electrochem. commun.* **122**, 106907 (2021).
20. Bodor, S., Zook, J. M., Lindner, E., Tóth, K. & Gyurcsányi, R. E. Chronopotentiometric method for the assessment of ionophore diffusion coefficients in solvent polymeric membranes. *J. Solid State Electrochem.* **13**, 171–179 (2009).
21. Gavande, S. S. *et al*. Comparative analysis of electrodeposited cobalt oxide thin films by chronoamperometry and chronopotentiometry modes for supercapacitor application. in *AIP Conference Proceedings* **2265**, 030615 (AIP Publishing LLC AIP Publishing, 2020).
22. Wessells, C., Ruff, R., Huggins, R. A. & Cui, Y. Investigations of the electrochemical stability of aqueous electrolytes for lithium battery applications. *Electrochem. Solid-State Lett.* **13**, A59 (2010).
23. Whitacre, J. F. *et al*. An Autonomous Electrochemical Test Stand for Machine Learning Informed Electrolyte Optimization. *J. Electrochem. Soc.* **166**, A4181–A4187 (2019).
24. Lin, K. *et al*. Alkaline quinone flow battery. *Science (80-.).* **349**, 1529–1532 (2015).
25. Davies, T. & Tummino, J. High-Performance Vanadium Redox Flow Batteries with Graphite Felt Electrodes. *C* **4**, 8 (2018).
26. Windsor, C. G. An introduction to small-angle neutron scattering. *J. Appl. Crystallogr.* **21**, 582–588 (1988).
27. Lamba, D. Wide Angle X-Ray Scattering (WAXS). *Encycl. Membr.* (2016). doi:10.1007/978-3-642-40872-4
28. Kikhney, A. G. & Svergun, D. I. A practical guide to small angle X-ray scattering (SAXS) of flexible and intrinsically disordered proteins. *FEBS Letters* **589**, 2570–2577 (2015).
29. Murthy, N. S. Scattering techniques for structural analysis of biomaterials. in

Characterization of Biomaterials 34–72 (Woodhead Publishing, 2012). doi:10.1533/9780857093684.34

30. Kotlarchyk, M. & Chen, S. H. Analysis of small angle neutron scattering spectra from polydisperse interacting colloids. *J. Chem. Phys.* **79**, 2461–2469 (1983).
31. Shibayama, M. Small-angle neutron scattering on polymer gels: Phase behavior, inhomogeneities and deformation mechanisms. *Polymer Journal* **43**, 18–34 (2011).
32. Lindner, P. (Peter) & Zemb, T. (Thomas). Neutron, X-rays and Light. Scattering Methods Applied to Soft Condensed Matter. *Mater. Today* **5**, 38 (2002).
33. Shull, C. G. & Wollan, E. O. X-ray, electron, and neutron diffraction. *Science (80-.).* **108**, 69–75 (1948).
34. Rinaldi, R., Liang, L. & Schober, H. Neutron Applications in Earth, Energy, and Environmental Sciences. 1–14 (2008). doi:10.1007/978-0-387-09416-8_1
35. Bras, W., Koizumi, S. & Terrill, N. J. Beyond simple small-angle X-ray scattering: developments in online complementary techniques and sample environments. *IUCrJ* **1**, 478–491 (2014).
36. Deen, W. *Analysis of Transport Phenomena*. (Oxford University Press, 2012).

Chapter 3. TOWARDS LOW-COST SOL-GEL SILICA COMPOSITE MEMBRANES FOR THE IRON-CHROMIUM REDOX-FLOW BATTERY

3.1 Background and Motivation

The membrane inside a RFB arguably plays the most critical role in its operation. The membrane is responsible for separating the active species on each side of the RFB while selectively allowing for the passage of charge balancing ions. Cross contamination of the active species can lead to an overall degradation and permanent loss of capacity. However, symmetric RFBs, such as the All-Vanadium RFB (VRFB) can mitigate detrimental crossover effects since the same ion species is present in both sides of the battery, leading only to a loss of efficiency. This attribute has aided the VRFB in becoming the most studied and developed RFB to date.[1] However, the vanadium electrolyte is non-sustainable and expensive, as ore extraction and mining in South Africa, China, and Russia account for a majority of produced vanadium.[2] This contributes to a total system cost of \$325-\$500 kWh^{-1} for VRFB, much higher than the DOE's cost target of \$100 kWh^{-1}.[3] Currently, the cost of RFB's is too high to implement widespread commercialization. In addition, the membrane itself can contribute up to 40% of the total RFB cost.[4] To further promote and amplify the commercialization of RFBs, the cost must be reduced dramatically.

The Iron-Chromium RFB (ICRFB) has the potential to overcome this economic barrier to RFB commercialization due to the utilization of inexpensive and abundant iron and chromium

active materials. The active material can be as low as \$17 kWh^{-1} with a total system cost of \$137 kWh[1.5] The equations below show the reactions occurring at the positive and negative electrodes, corresponding to the catholyte (iron) and anolyte(chromium) reactions, respectively.

$$Positive\ Electrode:\ Fe^{2+} \rightleftarrows Fe^{3+} + e^{-} \qquad E^0 = +0.77\ V \tag{3.1}$$

$$Negative\ Electrode:\ Cr^{3+} + e^{-} \rightleftarrows Cr^{2+} \qquad E^0 = -0.41\ V \tag{3.2}$$

$$Overall:\ Fe^{2+} + Cr^{3+} \rightleftarrows Fe^{3+} + Cr^{2+} \qquad E^0 = 1.18\ V \tag{3.3}$$

Despite the economic benefit of the asymmetric ICRFB, it is plagued by detrimental effects due to crossover contamination. Being the first true RFB developed by NASA in the late 70's, this issue was noted early on, and despite efforts at developing new membranes to combat the crossover, it was decided to instead employ a mixed electrolyte solution.[6] However, while this does reduce the rate of crossover by effectively reducing the concentration gradient between the anolyte and catholyte, the RFB is merely operating at an already degraded state in terms of capacity. Indeed, the capacity decay over time may be much less drastic using mixed electrolyte solutions, yet this state would eventually be reached anyways in the asymmetric configuration. The most used membrane for RFBs is Nafion, which is manufactured by DuPont. It is regarded highly for its good chemical stability, mechanical flexibility, and high conductivity. However, it possesses poor ion selectivity due to its relatively large pore size of about 2.5-3 nm.[1,7] While the ICRFB has been revived and increasingly studied within the past years, little has been done to address the need for a much more selective membrane.[5,8,9] The inability to develop a membrane with appropriate selectivity to prevent active species crossover and only allow the passage of

charge balancing ions is a fundamental engineering issue that is yet to be solved. For the economic viability of the ICRFB to be realized, the need for a superior performing membrane must be addressed.

Here we present the potential for low-cost sol-gel silica composite membranes as a replacement for Nafion in the ICRFB. The sol-gel process involves the conversion of a molecular precursor into a colloidal solution, which then proceeds to form the network that will eventually become the composite ceramic membrane. The molecular precursor is typically an inexpensive metal alkoxide, which undergoes hydrolysis and is followed by a series of condensation reactions.[10] The sol-gel process is attractive since one can proceed from the starting precursor directly to the product, enabling close control for specific properties that are desired.[11] Thus, it is possible to achieve much smaller, angstrom level pore sizes if the correct combination of starting materials are utilized. In addition, ceramic composites possess excellent chemical and thermal stability. In this regard, sol-gel silica composite membranes are an attractive option for use in ICRFBs.

3.2 Experimental Methods

3.2.1 *Membrane Synthesis*

Membranes are prepared via the sol-gel process using tetraethyl orthosilicate (TEOS) (98% Aldrich) as a silica based molecular precursor. The substrate for the membrane consists of either silica or cellulose paper with a polymer edging to prevent its fracture during RFB assembly. In some membranes, the substrate was soaked in a sodium silicate solution (SS) (27% Aldrich) prior to coating with the sol. Polystyrene sulfonic acid (PSS) (18% Aldrich) was also tested as a catalyst for the sol-gel reaction, added at a 1:1 volume ratio with TEOS when utilized. PSS can also

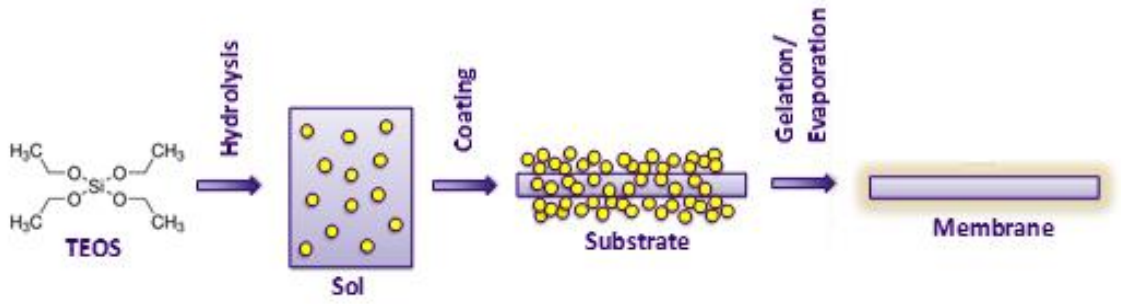

Figure 3.1. Membrane synthesis via sol-gel process

increase membrane conductivity and toughness. Following the coating process, the membranes dried for 24 hours under ambient pressure and temperature. Edged membranes were then soaked in 3M HCl for 12 hours to equilibrate in the supporting RFB electrolyte. Unedged membranes were used for structural characterization purposes.

3.2.2 *Structural Characterization*

To probe the structure of our silica composite membranes, small and wide-angle x-ray scattering (SWAXS) was performed. X-ray scattering techniques have been extensively used in the literature to investigate the structure of sol-gel materials.[12] The SWAXS was performed in-house using the SAXSess instrument system by Anton-Paar, operated in line collimation mode with a Cu *Kα* x-ray source having a wavelength of 1.54 angstroms. The data was converted to absolute scale by using a high-density polyethylene standard, as has been performed previously for laboratory scale x-ray scattering instruments.[13]

3.2.3 *Performance Characterization*

Potentiostatic electrochemical impedance spectroscopy (PEIS) was used in a 4-electrode setup to obtain the resistance of the membranes. The setup was identical to that described in chapter

2, where a modified H-cell contained the membrane with 3M HCl on each side, and the use of Lugin capillaries to measure potentials near the membrane was implemented. The electrodes used were a 3mm glassy carbon working sense electrodes, graphite working and counter electrodes, and an Ag/AgCl reference electrode. PEIS was conducted at a frequency range of 10-10^6 Hz with potentials of 0V DC and 5mv AC. A small excitation signal (1-10mV) is common in the literature in order to maintain pseudo linearity of the system.[14] The solution plus membrane resistances were determined in a Nyquist plot by the intersection of the curve with the zero axis, where the imaginary portion of the impedance is zero and only the ohmic resistance of the system is observed. The membrane area specific resistance (ASR) is then obtained by subtracting the bare solution resistance from the solution plus membrane resistance.

Membrane performance in terms of active species crossover was characterized by the permeability of Cr^{3+} and Fe^{3+} ions. The diffusion driven experiment was carried out in an H-cell, where the left compartment contained either 1M Cr^{3+} or Fe^{3+} ions as $CrCl_3$ and $FeCl_3$ (98%, 99% Aldrich) in 3M HCl and the right compartment contained 1M Al^{3+} ions as $AlCl_3$ (98% Fisher). The $AlCl_3$ is necessary to balance the ionic strength and reduce osmotic pressure across the membrane. Aliquots of 1mL in volume were extracted from the permeate side over periods of time and replaced with fresh $AlCl_3$ solution. The absorbance of the samples was measured using a Thermo Scientific UV-visible spectrophotometer at wavelengths between 250 and 550 nm, with a cuvette pathlength of 1cm, which enabled for the sample concentration to be calculated from a calibration curve. The permeability was obtained from the rate of change of concentration in the right compartment over time, described in equation 2.15 in Chapter 2.

3.3 RESULTS AND DISCUSSION

3.3.1 *Structural characterization from SWAXS*

After performing SWAXS on the silica composite membranes, some interesting features were found as seen in Figure 3.2. First, the only membrane that was not pre-coated with SS has a much different structure than the rest. The PSS TEOS Silica membrane has a very broad peak in the low q region from about 0.02 to 0.2. This indicates that larger, more widely distributed structures are present in the membrane. In the literature, other similar (almost identical) scattering plots in sol gel materials containing sulfonated polymers have shown this broad peak and it has been attributed to clusters of ionomers.[15–17] In contrast, all other membranes showed a much different structure, with well-defined peaks in the high q region at about 0.6 inverse angstroms. This indicates that these membranes have a much narrower distribution of particle sizes, which are much smaller than those observed in the broad peak of the PSS TEOS silica membrane. The SS seems to have a significant effect on the structure of these membranes. Even more interesting, the SS TEOS membrane on cellulose paper looks extremely similar to the counterpart when it is prepared on a silica paper substrate. The bare silica and cellulose paper substrates have different morphologies (Figure A2), most notably the sharp jagged peaks in the very high q region getting down to the molecular structure which is crystalline in the cellulose paper. Yet, we see all three of these membranes possess similar peaks, and even the crystallinity in the high q region of the SS TEOS cellulose membrane is reduced. The intensity of the peaks with the membranes pre-coated with SS varies, with the SS PSS TEOS silica membrane having the lowest intensity. Scattering and diffraction studies on silica gels have shown lower intensity peaks to correspond to higher

surface area and more ordered and organized structures with smaller pore sizes, which may be present here.[18]

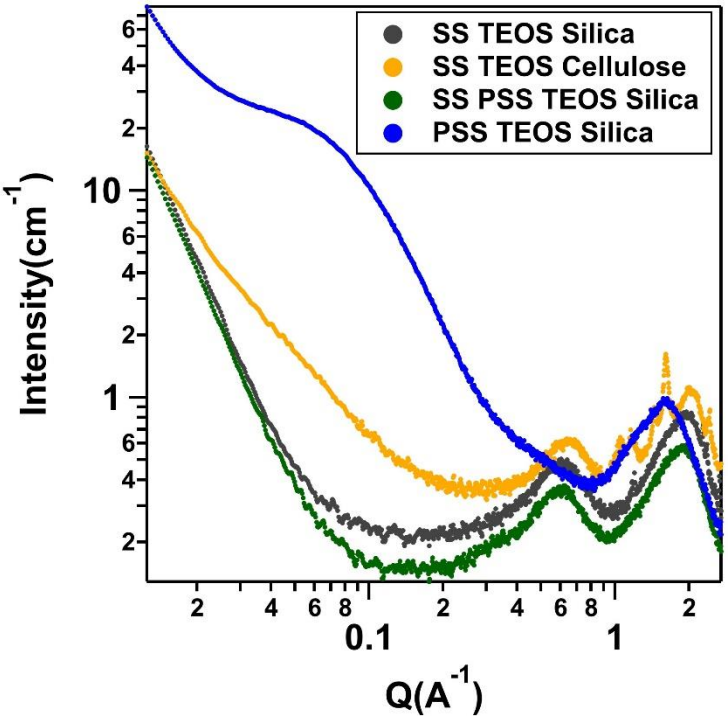

Figure 3.2. SWAXS of ceramic composite membranes.

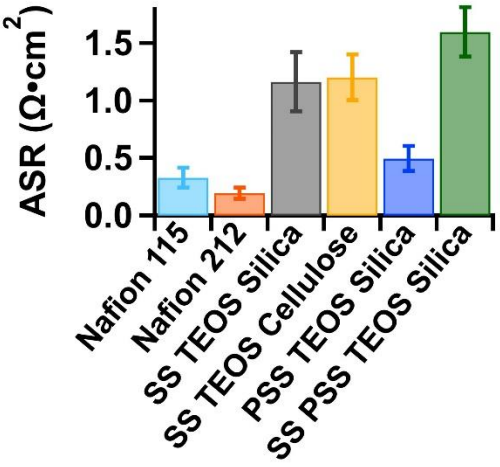

Figure 3.3. ASR of Nafion and ceramic composite membranes.

3.3.2 *Membrane ASR*

Figure 3.3 shows the ASR of our composite membranes compared to Nafion 212 and 115. Both Nafion membranes possessed very low ASRs, due to the nature of their structure with proton conducting sulfonic acid groups[19] and in addition to their hydrated thicknesses of only 0.06mm and 0.15 mm for Nafion 212 and 115, respectively. All silica composite membranes possessed higher ASRs than Nafion. The PSS TEOS membrane on silica paper substrate possessed the closest ASR to Nafion. This membrane was relatively thin at 0.2-0.23 mm and PSS has been incorporated in the literature for increased conductivity in other membranes, most notably for fuel cell applications.[20] Both SS TEOS membranes on silica and cellulose paper substrates had similar values for ASR and increased thicknesses between 0.28-0.35 mm, yet the membrane on silica paper was slightly less resistive. The highest ASR is seen in the SS PSS TEOS membrane, which was coated in the SS solution prior to dipping in the PSS TEOS sol. This membrane had a much glassier appearance than the other silica composites, which were rather opaque, in addition to an increased thickness of about 0.45-0.5 mm. A correlation between the thickness of the membrane and the ASR is noticed. Figure 3.4 below shows representative images of the edged sol-gel ceramic membranes

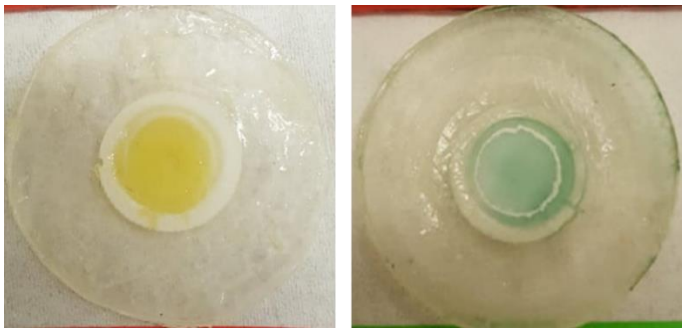

Figure 3.4. Images of edged sol-gel ceramic membranes. Images were taken after permeability experiments, where the left was tested with Fe^{3+} and the right was tested with Cr^{3+}.

3.3.3 *Cr^{3+} and Fe^{3+} Permeability*

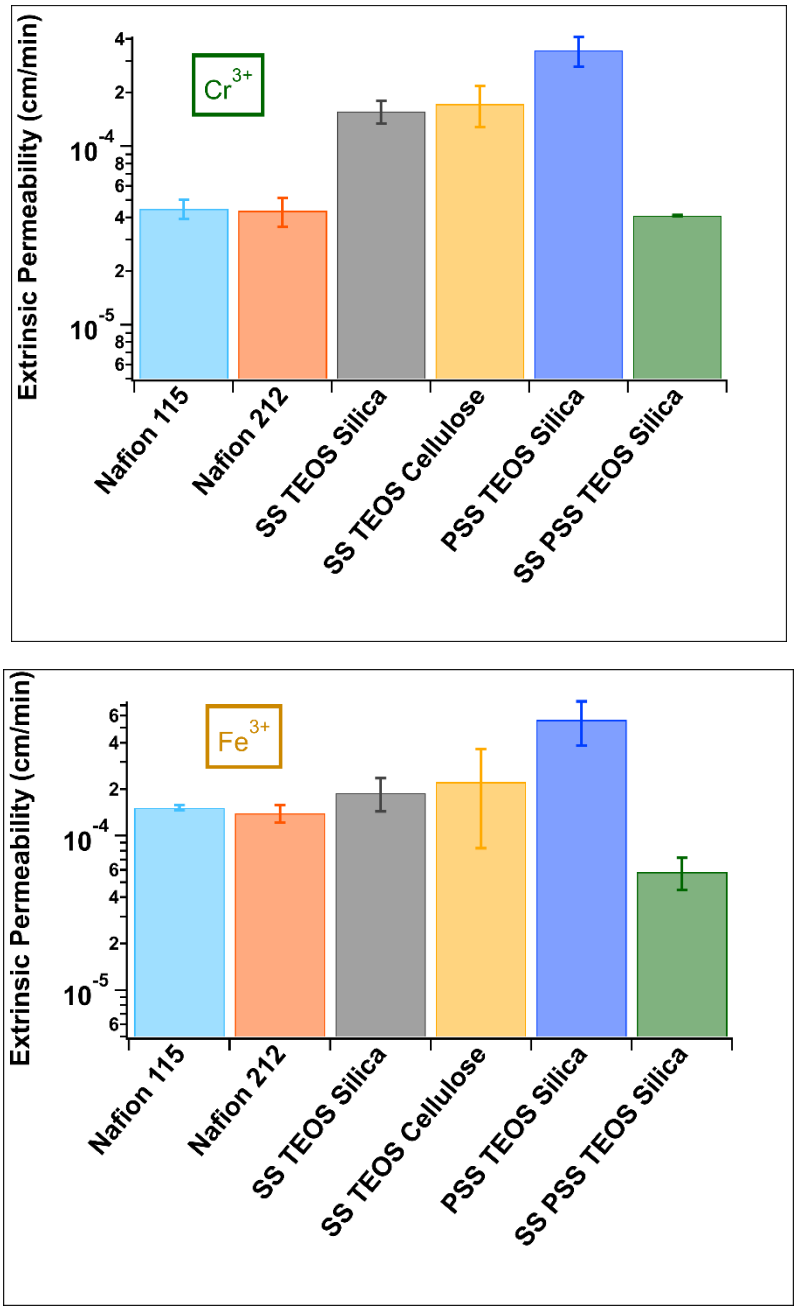

Figure 3.5. Permeability of Cr^{3+} (top) and Fe^{3+} (bottom) ions.

Figure 3.5 shows the extrinsic permeability of Cr^{3+} and Fe^{3+} ions in the Nafion and silica composite membranes. A lower value of permeability is desired. It is important to note that defects in the membrane such as microcracks can be a large contributor to the permeabilities seen here. Regardless of the membrane, permeabilities are lower for Cr^{3+} than for Fe^{3+}. This can be attributed to several factors on a molecular level. The structure of the hydrated Cr^{3+} ion is well defined up to the 4th hydration shell and exhibits very good stability with regards to the exchange of water molecules from its hydration shell to the bulk.[21] In contrast, the hydrated Fe^{3+} ion is well defined up to about only the 3rd hydration shell and is less stable.[22] Also, the size of the Cr^{3+} hydration shell is larger than that for Fe^{3+}, with Cr^{3+} having a radial distance of 5.1 angstroms in its second hydration shell, compared to approximately 2 angstroms for Fe^{3+}.[21–23] Both Nafion membranes possessed better permeability than the SS TEOS membrane on silica and cellulose substrates and the PSS TEOS membrane on silica substrate. Amongst those three, both SS TEOS membranes performed similarly, with the silica substrate performing slightly better, while the PSS TEOS membrane performed worse. The SS is rather viscous, and possibly aids in forming a much more filled and dense membrane structure than the PSS. In addition, the water content in the PSS is much higher than in the SS (82% vs ~60%) which may dilute the TEOS further. The SS PSS TEOS membrane on silica substrate matched the Cr^{3+} permeability and exceeded the Fe^{3+} permeability of both Nafion membranes. As mentioned, this membrane had a glassier appearance, and the effect of both the substrate curing with SS and addition of PSS seemed to have a positive impact on the permeability. If we look back at the SWAXS plot in Figure 3.2, a subtle trend can be noticed tying the positions and intensities of the peaks to the permeabilities. The PSS TEOS Silica was characterized with larger more widely distributed structures from the SWAXS, and subsequently had the worst permeability. From there on down, each membrane performed better than the one

before it, supporting the hypothesis that the SS has a significant effect on the structure, and that the lower intensities could mean higher surface areas and lower pore sizes. In addition, plotting the permeabilities vs the ASR of the membranes in Figure 3.6 shows a trend for the silica composite membranes where an increase in ASR will lead to a decrease in permeability and vice versa.

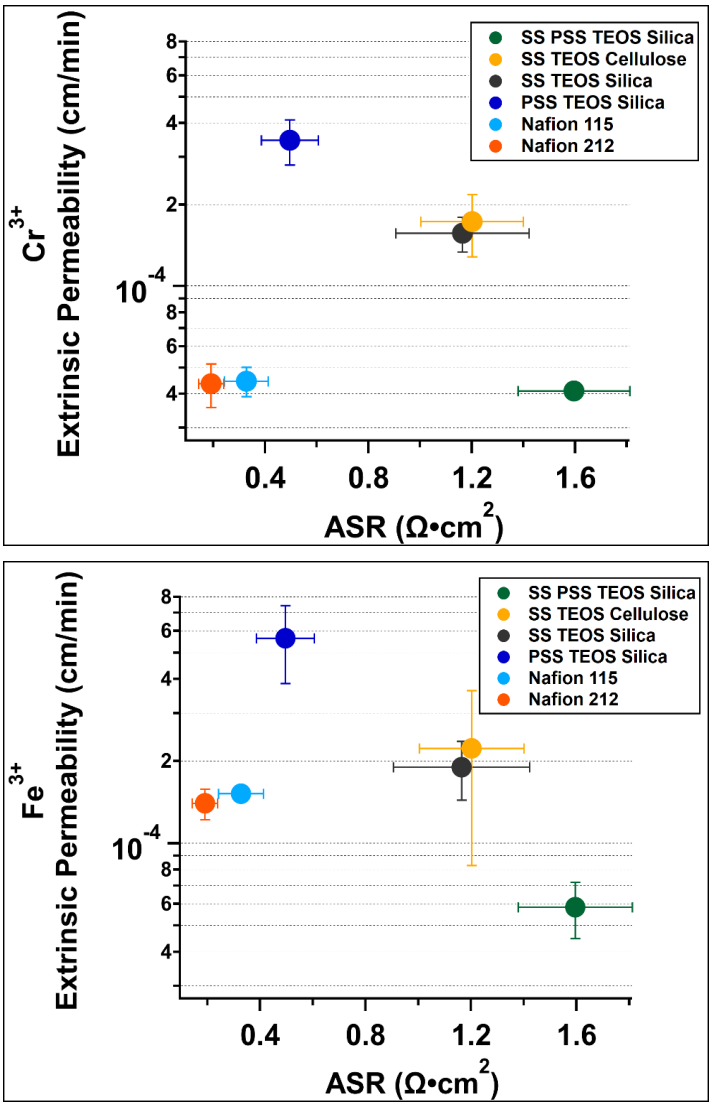

Figure 3.6. Permeability vs. membrane ASR for Cr^{3+} (top) and Fe^{3+} (bottom) ions.

3.4 Conclusions and Future Work

Composite silica membranes have been synthesized via the sol-gel process at low cost, and their potential to compete with high cost perfluorinated membranes, such as Nafion, has been demonstrated. Improvement in terms of the composite membrane ASR is necessary, however the potential for lower permeability is most attractive due to the detrimental crossover effects of the ICRFB. The need for a much more highly selective membrane is evident, and without one the economic potential for the ICRFB to cannot be practically realized. First steps would include investigating a much larger design space to find optimal sol-gel formulas based on composition of the materials used.

Developing a ceramic anion exchange membrane could facilitate the exclusion of cations by not only size, but also charge exclusion. One method of doing so is utilizing titianium (IV) tetraisopropoxide (TTIP) instead of TEOS. The titania membranes can maintain a substantial positive charge, but work must be done to improve the synthesis process to prevent the formation of precipitates. In addition, Ludox CL has been investigated to use as a pre-coating agent for the substrates. Ludox CL is a solution of colloidal silica, with each particle coated with a layer of alumina to convert it to a positive charge. Ultimately, the major end goal would be to test the ceramic composite membranes in a full-cell RFB. However, the use of these sol-gel ceramic membranes should not only be limited to RFB applications, as the contributions in this work have gone on to support efforts for ceramic desalination membranes produced by the company Membrion. This work consisted of a significant portion of US patent number 10,525,417, titled “Nanoporous Ceramic Membranes, Membrane Structures and Related Methods, which was

worked on alongside Membrion while in the early startup stages of the company. This work has proven to be a valuable contribution to the greater membrane and separator industry.

3.5 REFERENCES

1. Li, X., Zhang, H., Mai, Z., Zhang, H. & Vankelecom, I. Ion exchange membranes for vanadium redox flow battery (VRB) applications. *Energy Environ. Sci.* **4**, 1147 (2011).
2. Polyak, D. *Mineral Commodity Summaries, Vanadium*. *U.S. Geological Survey* (2021).
3. Crawford, A. *et al.* Comparative analysis for various redox flow batteries chemistries using a cost performance model. *J. Power Sources* **293**, 388–399 (2015).
4. Eckroad, S. & The Electric Power Research Institute. Vanadium Redox Flow Batteries: An In-Depth Analysis. **3**, 102 (2007).
5. Zeng, Y. K., Zhou, X. L., An, L., Wei, L. & Zhao, T. S. A high-performance flow-field structured iron-chromium redox flow battery. *J. Power Sources* **324**, 738–744 (2016).
6. NASA. *NASA redox storage system development project, calendar year 1982*. *Nasa Tm-83469* **1**, (1983).
7. Xu, Z. *et al.* Proton-Selective Ion Transport in ZSM-5 Zeolite Membrane. *J. Phys. Chem. C* **120**, 26386–26392 (2016).
8. Zeng, Y. K., Zhao, T. S., An, L., Zhou, X. L. & Wei, L. A comparative study of all-vanadium and iron-chromium redox flow batteries for large-scale energy storage. *J. Power Sources* **300**, 438–443 (2015).
9. Zeng, Y. K., Zhou, X. L., Zeng, L., Yan, X. H. & Zhao, T. S. Performance enhancement of iron-chromium redox flow batteries by employing interdigitated flow fields. *J. Power Sources* **327**, 258–264 (2016).
10. Colleoni, C. *et al.* Delayed luminescence induced by complex domains in water and in aqueous solutions. *Phys. Chem. Chem. Phys.* (2014). doi:10.1039/c5cp03420e
11. Livage, J., Henry, M. & Sanchez, C. Sol-gel chemistry of transition metal oxides. *Prog. Solid State Chem.* **18**, 259–341 (1988).
12. Brinker, C. J. & Scherer, G. W. Sol-Gel Science. doi:10.1186/1471-2105-8-444
13. Fan, L., Degen, M., Bendle, S., Grupido, N. & Ilavsky, J. The absolute calibration of a small-angle scattering instrument with a laboratory X-ray source. *J. Phys. Conf. Ser.* **247**, (2010).
14. Gamry Instruments. Basics of Electrochemical Impedance Spectroscopy. (2006).

15. Park, S.-M., Choi, Y.-W., Yang, T.-H., Park, J.-S. & Kim, S.-H. A study on sulfonated poly(arylene ether sulfone) membranes containing two different types of SiO2 for a high temperature and low-humidified polymer electrolyte fuel cell. *Korean J. Chem. Eng.* **30**, 87–94 (2013).

16. Brennan, A. B. & Wilkes, G. L. Structure Property Behavior of Sol-Gel Derived Hybrid Materials - Effect of a Polymeric Acid Catalyst. *Polymer (Guildf).* **32**, 733–739 (1991).

17. Mendil-Jakani, H., Zamanillo Lopez, I., Legrand, P. M., Mareau, V. H. & Gonon, L. A new interpretation of SAXS peaks in sulfonated poly(ether ether ketone) (sPEEK) membranes for fuel cells. *Phys. Chem. Chem. Phys.* **16**, 11243–11250 (2014).

18. Brahmi, D., Merabet, D., Belkacemi, H., Mostefaoui, T. A. & Ouakli, N. A. Preparation of amorphous silica gel from Algerian siliceous by-product of kaolin and its physico chemical properties. *Ceram. Int.* **40**, 10499–10503 (2014).

19. Mauritz, K. A. & Moore, R. B. State of understanding of Nafion. *Chem. Rev.* **104**, 4535–4585 (2004).

20. Sahu, A. K. *et al.* Effect of varying poly(styrene sulfonic acid) content in poly(vinyl alcohol)-poly(styrene sulfonic acid) blend membrane and its ramification in hydrogen-oxygen polymer electrolyte fuel cells. *J. Memb. Sci.* **319**, 298–305 (2008).

21. Bowron, D. T. & Díaz-Moreno, S. Solvent Structure and the Extended Range Hydration of Cr^{3+} in Aqueous Solution. *J. Phys. Chem. B* **113**, 11858–11864 (2009).

22. Kumar, P. V. & Tembe, B. L. Solvation structure and dynamics of the Fe^{2+} –Fe^{3+} ion pair in water. *J. Chem. Phys.* **97**, 4356–4367 (1992).

23. Amira, S., Spångberg, D., Probst, M. & Hermansson, K. Molecular Dynamics Simulation of Fe 2+ (aq) and Fe 3+ (aq). *J. Phys. Chem. B* **108**, 496–502 (2004).

Chapter 4. FLUORENONE BASED ANOLYTE FOR AN AQUEOUS ORGANIC REDOX-FLOW BATTERY

4.1 BACKGROUND AND MOTIVATION

While membranes in RFBs contribute a significant portion to the cost of the system, the choice of active materials used also significantly influences costs. Traditional RFBs have been based on redox couples of metal ions[1–4] and the current state-of-the-art RFB is based on the all-vanadium chemistry, but the high cost of this electrolyte material still limits widespread commercialization of RFBs and their incorporation into the grid.[5]

Recently, the use of redox active organic materials in RFBs has gained widespread attention.[6] These organic materials possess several advantages over their metal ion counterparts such as low cost, high abundance, molecular diversity, and tunability to achieve desired properties such as redox potential, solubility, and stability.[7] Many of these are also naturally occurring in the environment or already produced at scale for several other applications, with their potential for incorporation into RFBs just now being tapped. To date, a number of RFBs based on organic materials have been proposed, including quinones[8–10], TEMPO radicals[11–13], and viologen derivatives[14,15]. Previously, non-aqueous organic flow batteries were also proposed utilizing 9-fluorenone as an anolyte, which showed very negative redox potentials resulting in overall cell voltages surpassing 2V.[16,17] Furthermore, the cost of 9-fluorenone has been labeled to be as low as

$0.36 /mol , compared with vanadium at $1.50-$1.90 /mol.[18] Despite these attributes, non-aqueous organic RFBs still face numerous challenges including poor ionic conductivity and flammability.[19]

In this work, we present aqueous organic flow batteries based on fluorenone anolytes. A common method to increase the solubility of organic molecules in aqueous media is the addition of polar and/or ionizable functional groups. Here, carboxylic acid functionalization enables solubility of the core fluorenone molecule under alkaline conditions. Three fluorenone carboxylic acid (FCA) isomers, 9-fluorenone-1-carboxylic acid (F1CA), 9-fluorenone-2-carboxylic acid (F2CA) and 9-fluorenone-4-carboxylic acid (F4CA) were screened and assessed for their use in a full-cell cycling experiment. Ultimately, F2CA was chosen for full-cell cycling and paired with a ferro/ferricyanide redox-couple in 1M KOH with an overall cell voltage of 1.18 V. However, considerable capacity loss was observed within the first few cycles, in addition to a pH-dependent reversibility that limited its use to highly alkaline (pH 14) conditions. While the results show that F2CA is still not an optimal material in its current form, insight into the positional effects of functional groups is gained and the potential for further modification and molecular engineering of fluorenone-based RFB anolytes is noted.

4.2 EXPERIMENTAL METHODS

4.2.1 *Materials*

9-fluorenone-1-carboxylic acid (F1CA) (98%), 9-fluorenone-2-carboxylic acid (F2CA) (96%) and 9-fluorenone-4-carboxylic acid (F4CA) (98%) were purchased from TCI America. Potassium hexacyanoferrate (II) trihydrate (98.5%) and potassium ferricyanide (99%) were purchased from Sigma-Aldrich. The RFB hardware (Flow-Battery Flex Stack), ELAT hydrophilic carbon cloth, and Nafion 212 membrane were all purchased from the Fuel Cell Store.

4.2.2 *Solubility*

Room temperature saturated solutions of each FCA isomer were prepared by adding excess material to 1mL of 1M, 0.1M, and 0.01M KOH until visible precipitates formed. The solutions were equilibrated, filtered, and diluted as necessary to measure the optical absorbance using a Thermo Scientific Evolution 300 UV-Visible Spectrophotometer. These were then compared to calibration curves prepared by measuring the absorbance of a series of dilutions of known concentration from each isomer to obtain the maximum solubility.

4.2.3 *Cyclic Voltammetry*

Cyclic voltammetry (CV) measurements were obtained on a Gamry Reference 600 potentiostat utilizing a three-electrode setup. The electrodes were all purchased from Basi and consisted of a MF-2012 glassy carbon working electrode with 3.0 mm diameter, a MF-2013 platinum counter electrode with 1.6 mm diameter and a RE-5B Ag/AgCl (3M NaCl) reference electrode (+ 213 mV vs. SHE).

4.2.4 *Full-Cell Measurements and Charge-Discharge cycling*

The RFB consisted of 20mL of 0.5M F2CA in 2M KOH and 50mL of 0.3M $K_4Fe(CN)_6$ + 10mM $K_3Fe(CN)_6$ in 1M KOH, as the negative and positive electrolytes, respectively. Commercially available RFB hardware (Flow-Battery Flex Stack) was utilized with a 10 cm^2 active area, Viton rubber gaskets and with interdigitated graphite flow fields. ELAT hydrophilic carbon cloth was used as the electrode, pretreated by heating in a furnace at 500 °C for 6 hours. Nafion 212 was used as the membrane, equilibrated in 0.1M KOH for 6 hours prior to testing.

Galvanostatic charge/discharge cycling was performed using an 8-Channel battery tester (MTI, China) working at a current density of 5 mA/cm^2, with cutoff charging/discharging voltages

at 1.4V and 0.6V. A Cole-Parmer L/S peristaltic pump was used to circulate the electrolyte solutions through the RFB at a flowrate of 80 mL/min. Open circuit potential measurements were performed at various states of charge (SOC) in addition to polarization curves at 50% and 100% SOC. 100% SOC was obtained by potentiostatic charging at 1.4V until the magnitude of the current density dropped below 10 mA/cm^2. Electrochemical Impedance Spectroscopy (EIS) was performed at 50% state of charge at a frequency range of 10Hz-300kHz

4.3 Results and Discussion

4.3.1 *Solubility of FCA Isomers*

With the addition of a carboxylic acid functional group, solubility of the core fluorenone molecule is enabled under alkaline conditions due to acid-base reactions that form the carboxylate anion in solution. The solubility of the FCA isomers at different pH values was measured via UV-Vis and is shown in Figure 4.1. All isomers had the highest solubility in 1M KOH, with F2CA being the highest at 0.8M followed by F1CA at 0.76M and F4CA at 0.65M. These maximum solubilities would correspond to maximum theoretical capacities of 21.4 AhL-1, 20.4 AhL-1, and 17.4 AhL-1 for F2CA, F1CA, and F4CA, respectively. While the difference in functional group position varied the solubility slightly at pH 14, all isomers observed nearly an order of magnitude decrease in solubility at pH 13 and nearly two orders of magnitude decrease at pH 12. It is evident that a large hydroxyl ion concentration is necessary to fully deprotonate the carboxyl group, which limits the practical use of these molecules to pH > 14, which was also observed for other carboxyl functionalized organic materials.[20]

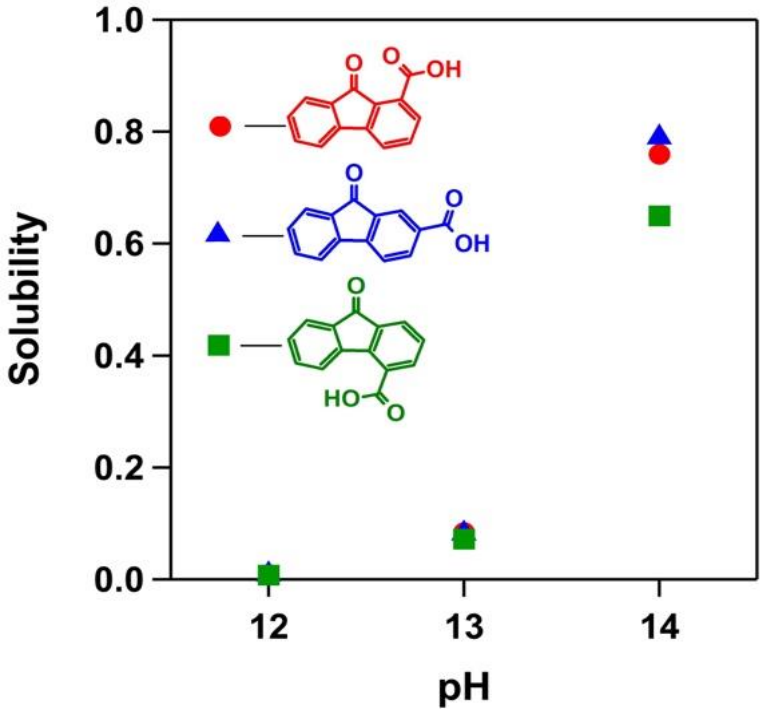

Figure 4.1. Maximum solubility of FCA isomers in pH 12, 13, and 14 KOH solutions.

4.3.2 *Electrochemical Characterization*

CV of F2CA (Figure 4.2B) and F4CA (Figure 4.2C) in 1M KOH revealed similar redox potentials of approximately -690 mV *vs* SHE. The peak separation of 51 mV for F2CA was close to the value of 57 mV/n, where n = 1 for a one step, one electron transfer. The peak separation for F4CA was significantly larger at 93 mV. Additionally, F2CA had a higher peak current ratio of 0.69 compared to 0.41 for F4CA. Further experiments with varying scan rate and 100 repeated cyclic voltammograms showed good reversibility for both molecules (Figure 4.3). The CV of F1CA (Figure 4.2A) revealed chemical irreversibility after a very negative reduction peak at -812 mV *vs* SHE. The positioning of the carboxyl group on the molecule clearly influences its redox reversibility. Based on these results, F2CA was chosen to proceed with full-cell performance measurements and charge discharge cycling.

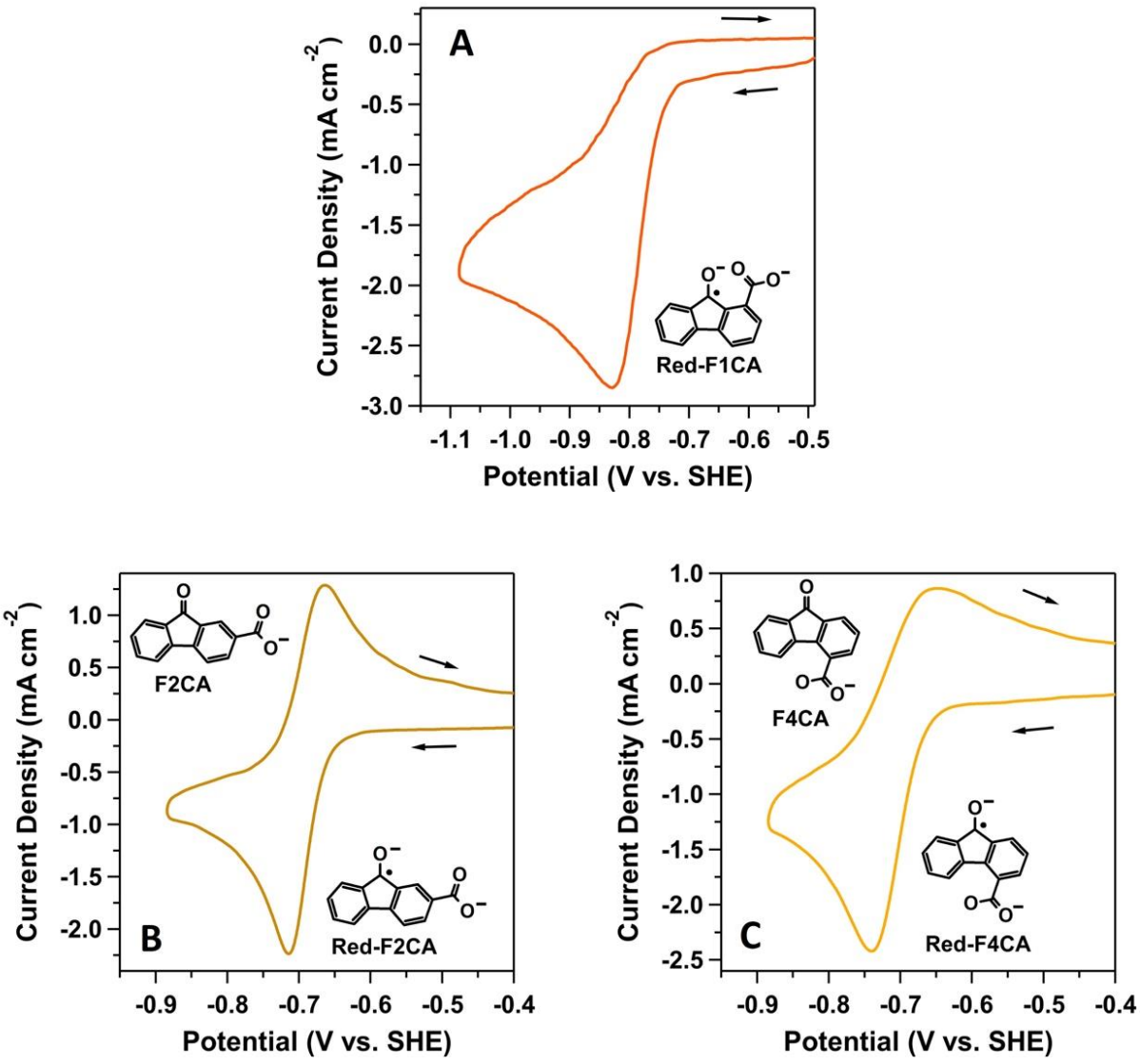

Figure 4.2. CV of FCA isomers in 1M KOH. A: 10mM F1CA. B: 10mM F2CA. C: 10mM F4CA.

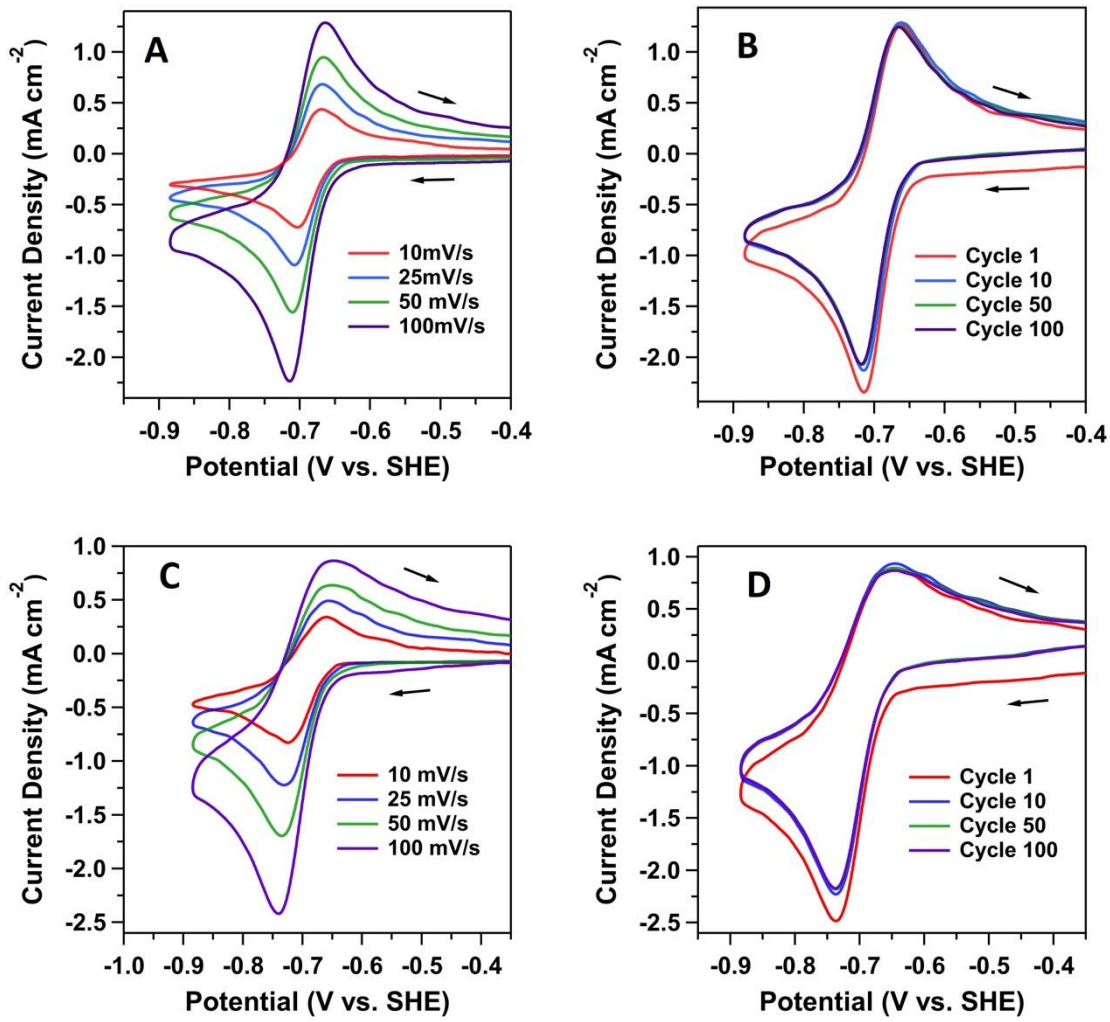

Figure 4.3. CV of F2CA (A, B) and F4CA (C, D) isomers in 1M KOH with varying scan rates and cycles.

4.3.3 *Full-Cell Performance and Charge-Discharge Cycling*

The RFB consisted of 20mL of 0.5M F2CA in 2M KOH and 50mL of 0.3M $K_4Fe(CN)_6$ + 10mM $K_3Fe(CN)_6$ in 1M KOH, as the negative and positive electrolytes, respectively. Pairing the F2CA with a ferro/ferricyanide redox couple gives an open circuit potential of 1.18 V with a theoretical charge capacity of 13.4 AhL^{-1} corresponding to a total theoretical energy density of 3.4 WhL^{-1}. Open circuit potential of the full cell was measured across various SOC, beginning at 1.1V at 10% SOC and then climbing to 1.18 V at 50% SOC before shooting up to 1.34 V at 100% SOC (Figure 4.4B). Polarization curves demonstrate the cell potential and power density vs. current density at 50% and 100% SOC (Figure 4.4C). At 100% SOC the peak power density is 26 $mWcm^{-2}$, which is considerably lower than that of other aqueous organic RFBs.[21] In addition, the limiting current density at 100% SOC is only 30 mA/cm^2. EIS taken at a frequency range of 10Hz to 300 kHz reveals the cell area specific resistance of 6.17 Ωcm^2, given by the intersection of the zero axis with the high frequency portion of the curve at approximately 150 kHz (Figure 4.4D). The abundance of negatively charged hydroxyl ions in 1M KOH results in the ionic conductivity of Nafion 212 to be considerably lower than in acidic media since it is a perfluorinated cation-exchange membrane.[22] This could clearly be a cause for the increased cell resistance and low limiting current density of the system.

Galvanostatic charge/discharge cycling was performed at 5 mA/cm^2 with upper and lower potential limits of 1.4 V and 0.6 V. Significant capacity loss was observed after only the first few cycles, losing approximately 90% its capacity and eventually leveling off. While efficiencies dipped slightly during this loss of capacity, they later increased and generally remained steady as seen in Figure 4.5 B. Crossover of active species in asymmetric RFBs has been a common culprit for capacity loss in various systems, however this is unlikely to have caused the capacity losses

observed here as only minor amounts of material were observed, through UV-Vis spectroscopy, in opposite reservoirs after cycling.

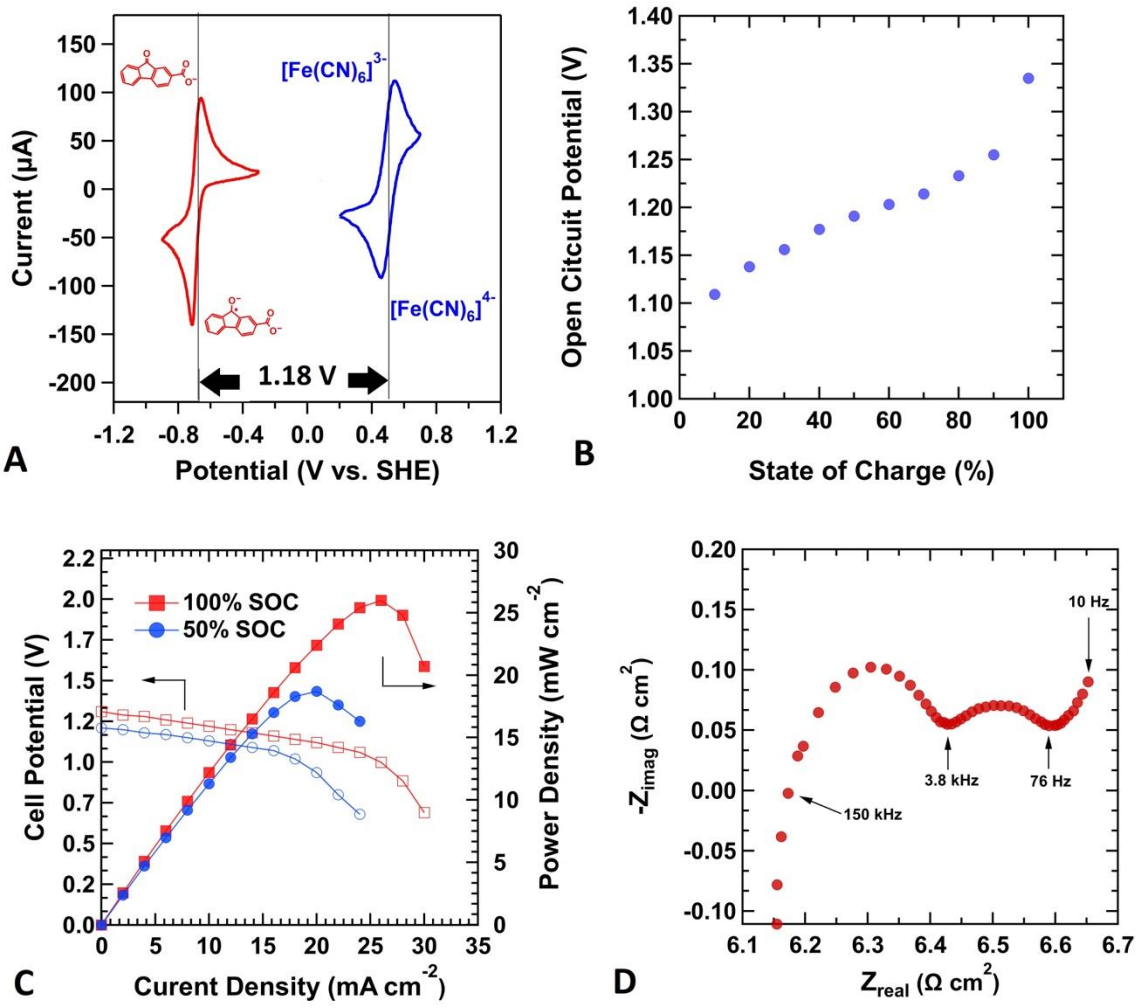

Figure 4.4. Full-cell measurements of F2CA RFB. A: Open cell potential of the F2CA/ferrocyanide RFB. B: Open circuit potential of the full cell at various SOC. C.: Polarization curves demonstrating the cell potential vs current density and power density at 50% and 100% SOC. D: EIS on the full-cell at a frequency range of 10 Hz-300 kHz.

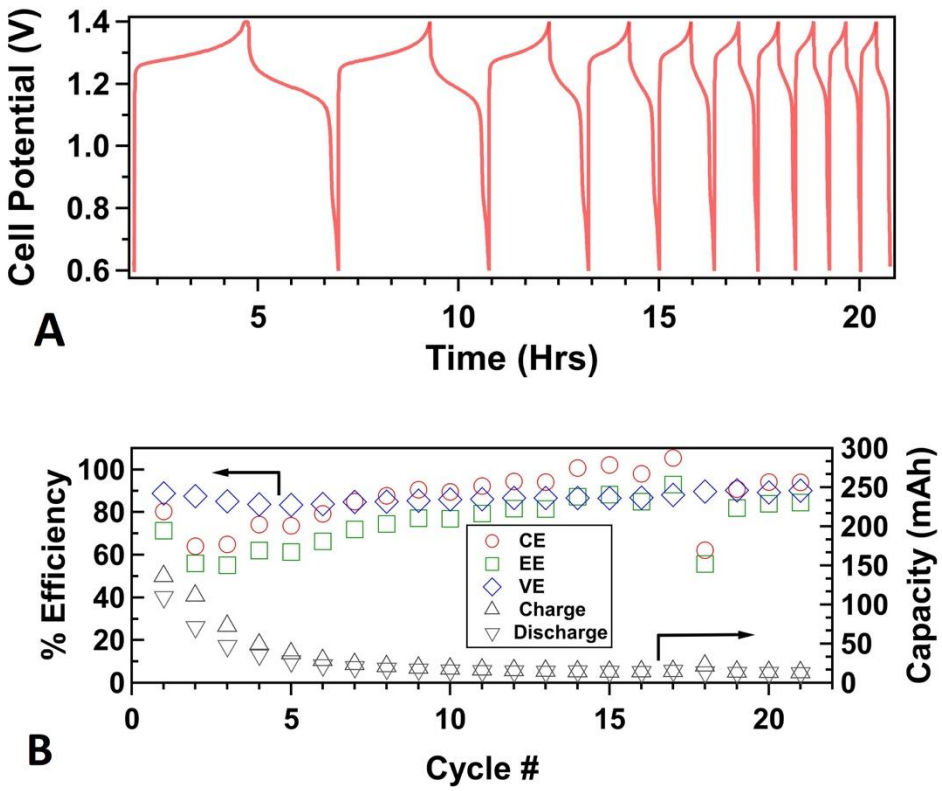

Figure 4.5. A. Charge/discharge cycling curves of the F2CA/Ferrocyanide RFB. Only the first ten cycles are shown. B. Performance efficiencies and charge/discharge capacities over 21 cycles.

4.3.4 *Dependence on Reversibility on pH and Potential Range*

Further analysis of the electrochemical behavior of F2CA was conducted in order to understand underlying mechanisms leading to capacity losses observed during full-cell cycling. Cyclic voltammograms scanned down to -1.3 V relative to SHE resulted in the appearance of a second reduction peak at ~1.08 V. This second reduction was found to be irreversible and also led to a decrease in the redox reversibility of the main peak at ~0.7 V, corresponding to the formation of the F2CA radical-anion (Figure 4.6A). CV curves collected over 100 cycles over the extended potential range demonstrated a severe decrease in peak heights, a majority of which occurred

between cycles one and ten (Figure 4.6B). These results suggest that there is a secondary reaction of the F2CA radical anion that leads to the formation of a chemically irreversible species. At the time of writing, the nature of this reaction and the new chemical species remains unknown.

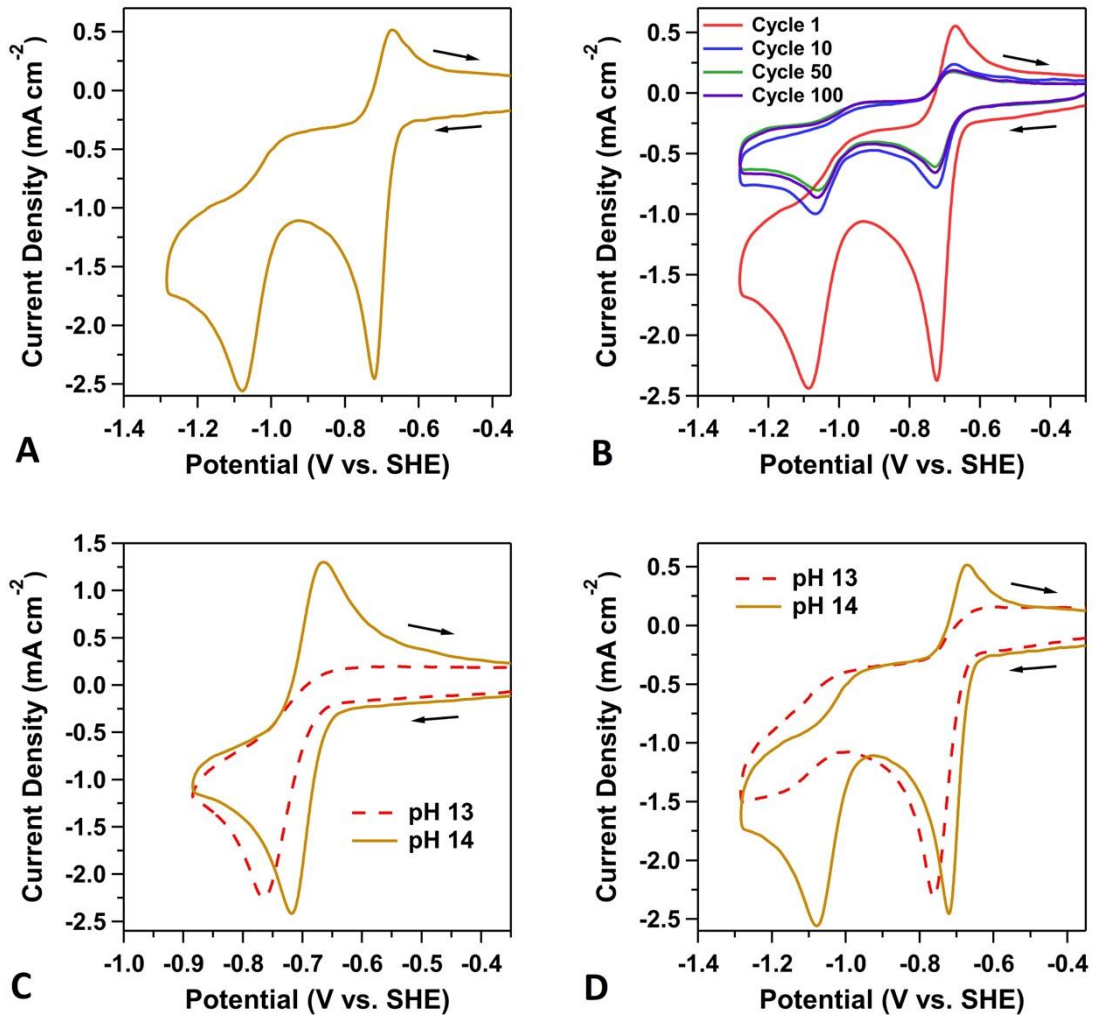

Figure 4.6. CV of F2CA at varying potential ranges and pH. A: CV of 10mM F2CA at extended potential range. B: 100 subsequent CV cycles of 10mM F2CA at extended potential range. C: CV of 10mM F2CA in pH 13 compared to pH 14. D: CV of 10mM F2CA at extended potential range in pH 13 compared to pH 14.

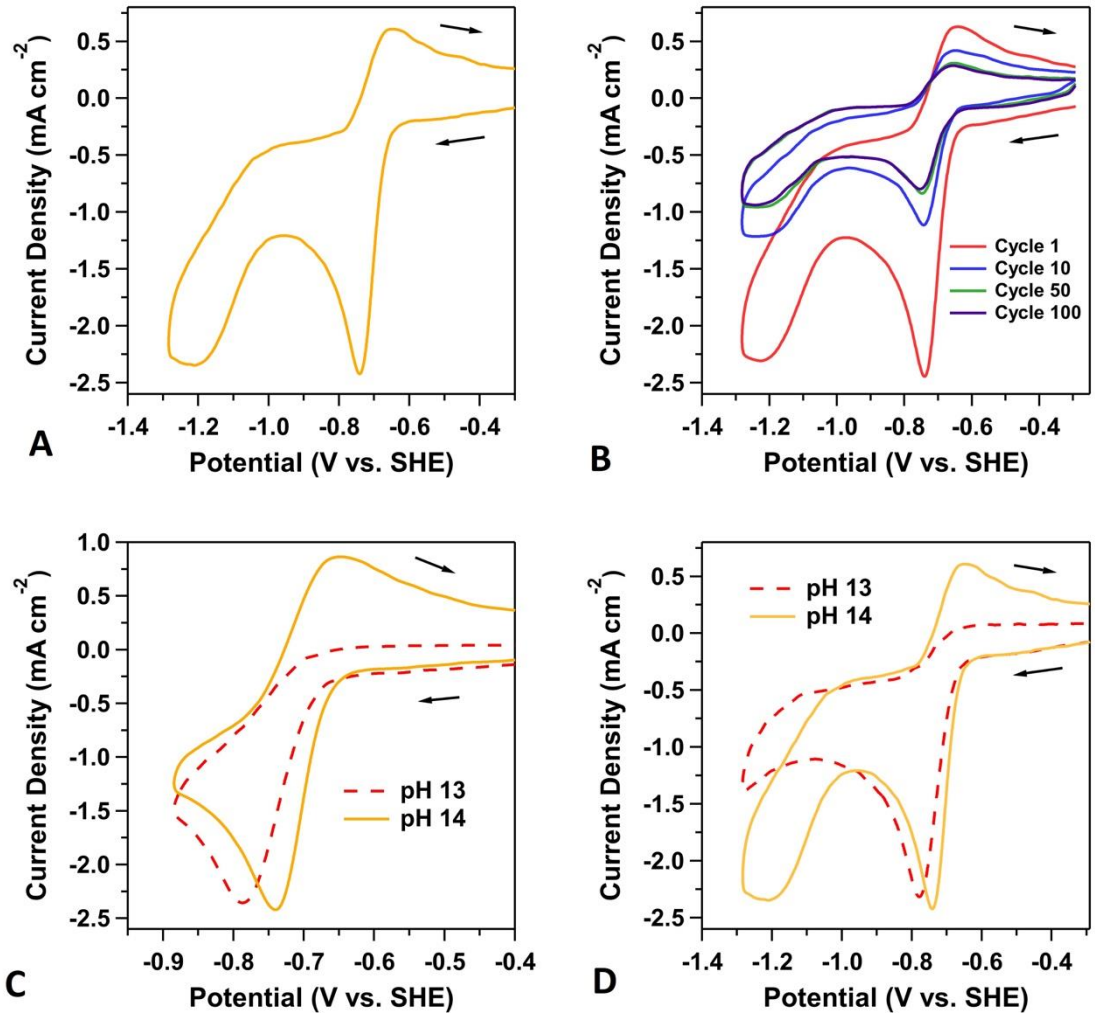

Figure 4.7. CV of F4CA at varying potential ranges and pH. A: CV of 10mM F4CA at extended potential range. B: 100 subsequent CV cycles of 10mM F4CA at extended potential range. C: CV of 10mM F4CA in pH 13 compared to pH 14. D: CV of 10mM F4CA at extended potential range in pH 13 compared to pH 14.

Furthermore, it was also observed that the F2CA completely loses reversibility in solutions below pH 14, as seen in Figure 4.6 C. In 0.1M KOH (pH 13) the CV curve resembles more closely that of F1CA which was found to be irreversible even at pH 14. Other aqueous organic RFBs under alkaline media have reported losses in electrochemical reversibility with variations in pH, but a

complete loss of chemical reversibility was not observed.[23] Near identical behavior was found with F4CA as seen in figure 4.7. From these observations, it is evident that the redox reversibility of FCA molecules is strongly correlated to their ionization state.

It was noted earlier that the FCA isomers achieved maximum solubility when they were fully deprotonated. In this situation, to be fully deprotonated requires that the pH be higher than the pKa of the molecule. It would also appear that full deprotonation of the molecule is necessary for reversible redox behavior. This in turn raises the question of why F1CA still behaved irreversibly. The change between the pKa of fluorenone (pKa -6.6) and its reduced radical anion form (pKa 6.3) is quite significant.[24] This could suggest that redox reversibility could be lost if the pKa of the reduced radical anion form becomes lower than the pH of the environment. However, it also important to consider the contribution to the molecule's pKa by addition of polar functional groups. Not only does the specific type of functional group, in this case a carboxyl group, contribute to the pKa but also the specific location of the functional group on the molecule.[25] Therefore, it is possible that for F1CA, the position of the carboxyl group closest to the carbonyl, along with the change in pKa to the radical anion form, results in the overall pKa of the molecule being higher than the solution's pH. While F2CA and F4CA are reversible at pH 14, changing the solution to pH 13 is enough for protonation of the radical anion leading to a loss in reversibility. Also, the second reduction peak observed at very negative potentials disappears at pH 13, suggesting that it is also dependent on the molecule being fully deprotonated (Figure 4.6D). These hypotheses could explain the drastic capacity losses observed during full-cell cycling. It is possible that these irreversible reduction reactions are occurring during cell cycling and leading to the formation of irreversible chemical species. In addition, it is also possible that pH values could vary during cycling, leading to the irreversible behavior that is observed in CV.

4.3.5 *Conclusions and Future Work*

An aqueous organic RFB based on a fluorenone anolyte was investigated with polar carboxylic acid functional groups that enabled significant solubility in alkaline media. Preliminary screening of three FCA isomers indicated varying solubilities and redox behavior. An isomer containing the carboxyl group on the second position, F2CA, was chosen to continue testing with the full-cell battery system. Paired with a ferro/ferricyanide redox couple, this RFB produced an open cell potential of 1.18 V. Performance characteristics of the full-cell system indicated low peak power density and low limiting current density. Charge/discharge cycling revealed significant capacity loss within the first few cycles. Subsequent analysis of the F2CA redox behavior indicated dependences of the reversibility on pH and potential, which vary based on the position of the carboxyl group on the molecule. While the RFB in its current state is not yet feasible for large-scale energy storage due to capacity loss, the use of fluorenone is promising to achieve high cell potentials and low-cost RFBs. Further investigation and improvements through molecular engineering with other polar functional groups and electrolyte formulations is recommended. Particularly, the electrochemical stability of the FCA isomers should be investigated to have a deeper understanding of the chemical mechanisms at play that may have similar consequences in other novel active material selections. At the initial publication of this work, this was the only study to have implemented the use of fluorenone in an aqueous RFB but has now provided the foundation on which to successfully utilize fluorenone. Recently, Feng et al. took into account the conclusion in this work that molecular engineering to reduce the pKa could fully deprotonate the fluorenone molecule and enable reversible redox behavior in aqueous electrolytes. A number of fluorenone derivatives with varying functional groups were synthesized in an attempt to reduce

the pKa, and those that moved on to full-cell cycling experiments performed extremely well and confirmed the attractiveness and potential of fluorenone as an energy storage molecule.[26]

4.4 REFERENCES

1. Zeng, Y. K., Zhou, X. L., An, L., Wei, L. & Zhao, T. S. A high-performance flow-field structured iron-chromium redox flow battery. *J. Power Sources* **324**, 738–744 (2016).
2. Leung, P. K., Ponce-De-León, C., Low, C. T. J., Shah, A. A. & Walsh, F. C. Characterization of a zinc-cerium flow battery. *J. Power Sources* **196**, 5174–5185 (2011).
3. Petek, T. J., Hoyt, N. C., Savinell, R. F. & Wainright, J. S. Slurry electrodes for iron plating in an all-iron flow battery. *J. Power Sources* **294**, 620–626 (2015).
4. Narayanan, S. R. *et al.* A High Efficiency Iron-Chloride Redox Flow Battery for Large-Scale Energy Storage. *J. Electrochem. Soc.* **163**, A5118–A5125 (2015).
5. Nguyen, T. & Savinell, R. F. Flow Batteries. *Electrochem. Soc. Interface* **19**, 54–56 (2010).
6. Shah, A. A. *et al.* Recent developments in organic redox flow batteries: A critical review. *J. Power Sources* **360**, 243–283 (2017).
7. Chen, H., Cong, G. & Lu, Y. C. Recent progress in organic redox flow batteries: Active materials, electrolytes and membranes. *J. Energy Chem.* (2018) doi:10.1016/j.jechem.2018.02.009.
8. Huskinson, B. *et al.* A metal-free organic-inorganic aqueous flow battery. *Nature* **505**, 195–198 (2014).
9. Yang, B., Hoober-Burkhardt, L., Wang, F., Surya Prakash, G. K. & Narayanan, S. R. An Inexpensive Aqueous Flow Battery for Large-Scale Electrical Energy Storage Based on

Water-Soluble Organic Redox Couples. *J. Electrochem. Soc.* **161**, A1371–A1380 (2014).

10. Yang, B. *et al.* High-Performance Aqueous Organic Flow Battery with Quinone-Based Redox Couples at Both Electrodes. *J. Electrochem. Soc.* **163**, A1442–A1449 (2016).
11. Wei, X., Nie, Z., Wang, W., Liu, T. & Sprenkle, V. A Total Organic Aqueous Redox Flow Battery Employing a Low Cost and Sustainable Methyl Viologen Anolyte and 4-HO-TEMPO Catholyte. *Adv. Energy Mater.* **6**, 1501449 (2015).
12. Winsberg, J. *et al.* Aqueous 2,2,6,6-Tetramethylpiperidine-N-oxyl Catholytes for a High-Capacity and High Current Density Oxygen-Insensitive Hybrid-Flow Battery. *ACS Energy Lett.* **2**, 411–416 (2017).
13. Winsberg, J. *et al.* TEMPO/Phenazine Combi-Molecule: A Redox-Active Material for Symmetric Aqueous Redox-Flow Batteries. *ACS Energy Lett.* **1**, 976–980 (2016).
14. Debruler, C., Hu, B., Moss, J., Luo, J. & Liu, T. L. A Sulfonate-Functionalized Viologen Enabling Neutral Cation Exchange, Aqueous Organic Redox Flow Batteries toward Renewable Energy Storage. *ACS Energy Lett.* **3**, 663–668 (2018).
15. Hu, B. & Liu, T. L. Two electron utilization of methyl viologen anolyte in nonaqueous organic redox flow battery. *J. Energy Chem.* **27**, 1326–1332 (2018).
16. Wei, X. *et al.* Radical Compatibility with Nonaqueous Electrolytes and Its Impact on an All-Organic Redox Flow Battery. *Angew. Chemie - Int. Ed.* **54**, 8684–8687 (2015).
17. Kwon, G. *et al.* Multi-redox Molecule for High-Energy Redox Flow Batteries. *Joule* **2**, 1771–1782 (2018).
18. Wei, X. *et al.* Materials and Systems for Organic Redox Flow Batteries: Status and Challenges. *ACS Energy Lett.* **2**, 2187–2204 (2017).
19. Gong, K., Fang, Q., Gu, S., Li, S. F. Y. & Yan, Y. Nonaqueous redox-flow batteries:

Organic solvents, supporting electrolytes, and redox pairs. *Energy Environ. Sci.* **8**, 3515–3530 (2015).

20. Lin, K. *et al.* A redox-flow battery with an alloxazine-based organic electrolyte. *Nat. Energy* **1**, (2016).
21. Ding, Y., Zhang, C., Zhang, L., Zhou, Y. & Yu, G. Molecular engineering of organic electroactive materials for redox flow batteries. *Chem. Soc. Rev.* **47**, 69–103 (2018).
22. Mauritz, K. A. & Moore, R. B. State of understanding of Nafion. *Chem. Rev.* **104**, 4535–4585 (2004).
23. Yang, Z. *et al.* Alkaline Benzoquinone Aqueous Flow Battery for Large-Scale Storage of Electrical Energy. *Adv. Energy Mater.* **8**, 1–9 (2018).
24. Todres, Z. V. *Organic ion radicals: chemistry and applications*. *Choice Reviews Online* vol. 40 (2013).
25. Hollingsworth, C. A., Seybold, P. G. & Hadad, C. M. Substituent effects on the electronic structure and pKa of benzoic acid. *Int. J. Quantum Chem.* **90**, 1396–1403 (2002).
26. Feng, R. *et al.* Reversible ketone hydrogenation and dehydrogenation for aqueous organic redox flow batteries. *Science (80-.).* **372**, 836–840 (2021).

Chapter 5. REDOX-ACTIVE DEEP EUTECTIC SOLVENTS FOR REDOX-FLOW BATTERIES

5.1 Background and Motivation

While Chapter 4 focused on various redox active materials for use in RFBs, another important area of research are the solvents that enable these active materials to be present in solution. Currently, the choice of solvents for RFBs can be categorized as either aqueous or non-aqueous. Both have their respective advantages and disadvantages. Aqueous based RFBs are praised for the low cost, simplicity, and good ionic conductivity of the solvents.[1–4] However, their shortcomings include a limited active material solubility (generally < 1M for organics), corrosiveness due to extreme pH conditions, and a limited potential window that is dictated by water electrolysis.[3,5] Non-aqueous RFBs on the other hand are not limited by water electrolysis and possess much larger potential windows with greater active material solubility, yet suffer from poor ionic conductivity, flammability, and an increased costs.[3,6–8] The boundary between these two solvent classifications is being pushed to include more complex, unique systems that can potentially address the drawbacks present in both, with a strong emphasis on making sure these lie within the framework of 'green' and sustainable chemistry.[9] An alternative solvent category that is commonly considered is that of room temperature ionic liquids (RTILs), which are molten organic salts that are liquid below 100°C.[10] RTILs have found numerous applications aside from energy storage, such as catalysis, separation and extractions, carriers for pharmaceuticals, and within the food industry.[11–13] While RTILs possess numerous reputable qualities for use as solvents in RFBs,

including good ionic conductivity and solubility of organic species, their extreme sensitivity to impurities significantly drives up manufacturing costs.[9] In addition, their environmental friendliness and safety has come into concern lately, questioning just how well they fit into the framework of 'green' chemical solvents.[14]

As an alternative to RTILs, the popularity of deep eutectic solvents (DES) has increased substantially over the last decade. These new solvents have many of the desirable qualities of RTILs but without the drawbacks that were just mentioned. A DES is composed of two materials that, when mixed in specific molar ratios, undergo a depression in the freezing point of the mixture that is significantly lower than that of both individual materials.[9,15] DES have often been labeled as a subset of RTILs, when in reality the two are quite different. DES are classified as eutectic mixtures between Lewis or Bronsted acids and bases, whereas RTILs are formed primarily from a specific type of discrete anion or cation.[16] Here, we will mostly be concerned with DES that are formed between organic quaternary ammonium salts (QAS) and organic hydrogen bond donors (HBD), known as type III DES, some of which are displayed in Figure 5.1 and Table 5.1 below.

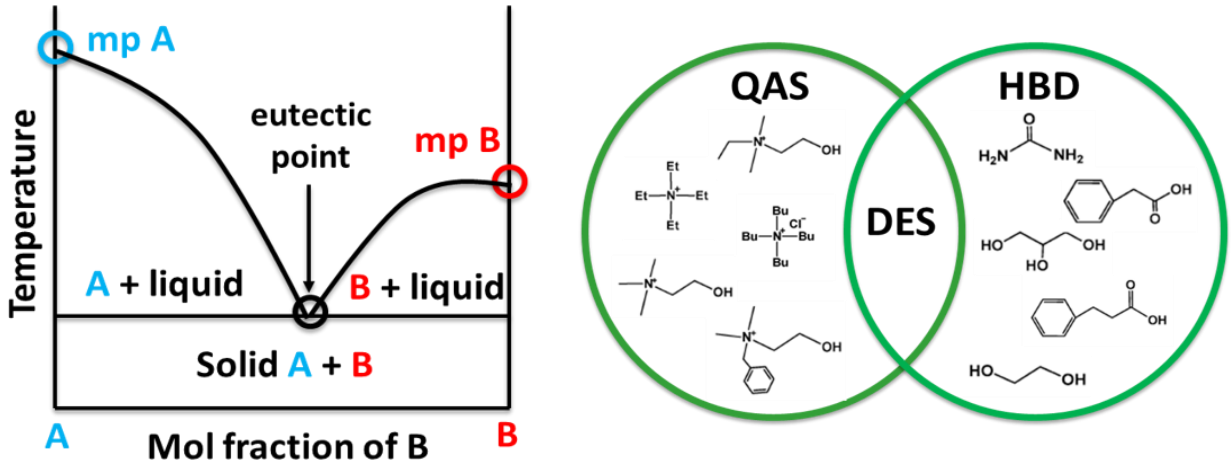

Figure 5.1. Left: Eutectic formation between two components. Right: Structures of some QAS and HBD that form DES.

Table 5.1. Freezing points of various choline chloride-based DES.

QAS	HBD	Molar Ratio	Freezing Point	Ref.
ChCl	Urea	1 : 2	12°C	[17]
ChCl	Ethylene Glycol	1 : 2	-66°C	[18]
ChCl	Glycerol	1 : 2	-40°C	[19]
ChCl	Phenylacetic Acid	1 : 2	25°C	[20]
ChCl	Phenylpropionic Acid	1 : 2	20°C	[20]
ChCl	Citric Acid	1 : 1	69°C	[20]
ChCl	Benzoic Acid	1 : 1	95°C	[20]
ChCl	Imidazole	3 : 7	56°C	[21]
ChCl	Resorcinol	1 : 4	87°C	[22]

Compared to most RTILs, a majority of DES are composed of environmentally safe and non-toxic materials that are inexpensive and widely mass produced. Table 5.1 shows a list of common DES based on choline chloride, which is a salt primarily used in animal feed. The freezing points of these DES can range quite drastically, where we see the ChCl:ethylene glycol (EG) DES freezing at -66°C and ChCl: benzoic acid freezing at 95°C. There has been some debate over whether certain DES where one of the components is already initially in the liquid state, such as with ethylene glycol or glycerol, actually constitute a true DES.[23] In general, like RTILs, DES freezing points lie near or below 100°C. Ideally, the goal is to have freezing points as close to room temperature as possible. Recently, studies have investigated the use of DES in lithium-ion batteries, noting its attractiveness as a replacement for flammable and more expensive solvents

typically used with this storage technology.[24,25] The favorable transport properties and ionic conductivities gives good promise for this application moving forward. Perhaps one of the most intriguing benefits of using DES is their ability to enhance solubilization across a wide range of materials. CO_2 extraction and separation of metal ions from water using common DES has been a popular area of investigation.[15,26,27] The pharmaceutical field has been looking at DES as a potential medium for drug solubilization and delivery, with some astonishing results. It was reported that drug solubilization in simple DES formulations yielded a 5 to 22,000 fold increase in concentration when compared to pure water.[28]

The DES solubilization strategy has recently been adopted also for RFBs in an effort to increase the energy density of the system, albeit initial efforts resorted to the use of inorganic metal redox species.[29–31] While the use of DES in RFBs is still in its infancy, the incorporation of ROM's into DES is something that has largely been unexplored, despite the significant implications that this could have. When looking more closely at the structure of ROMs, particularly those used in aqueous systems, many of these can also be considered as HBDs. Therefore, there lies the possibility of incorporating ROMs into the DES, which we call redox-active deep eutectic solvents (RDES). These could exist as a binary system where the ROM directly forms a eutectic with another species, or with the addition of a ROM into an established DES that forms a ternary system, as shown in Figure 5.2.

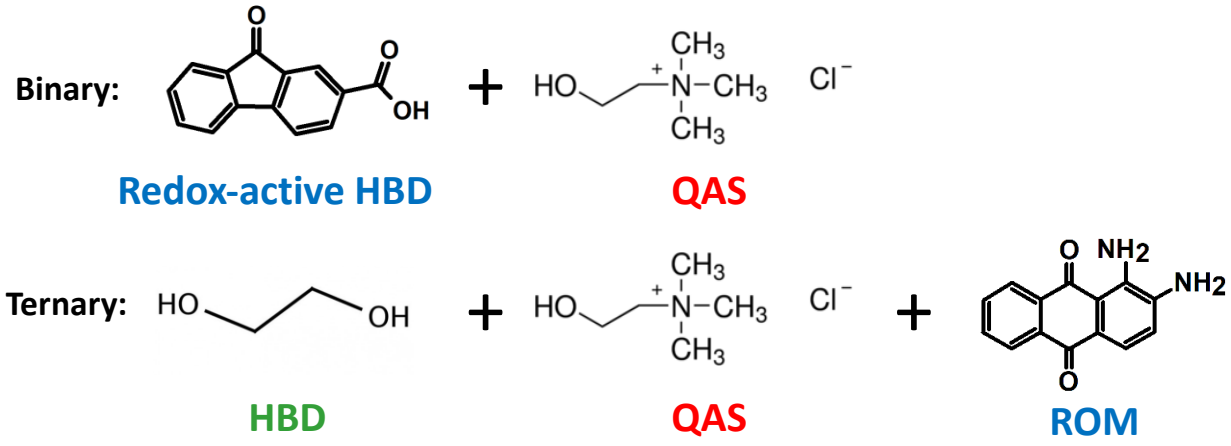

Figure 5.2. Structures of possible binary and ternary RDES.

Two notable studies have explored the incorporation of ROMs into DES, and both reported increased solubilities, which directly correlates to increases in energy density.[32,33] Thus, exploring the use of ROMs in conjunction with DES electrolytes for RFBs could be impactful to the technology. However, major challenges exist for developing ideal combinations of ROMs and DES electrolytes. In addition to the very large design space that is available for ROMs, the literature states that the number of possible DES rivals the number of estimated ILs (>10^{18} unique combinations).[34,35] Yet, despite the simple synthesis process for DES, current experimental efforts and methods have been slow to make a significant dent in fully exploring these new materials. It will be impossible to probe the entire design space via experiments alone, and as such, computational methods have become a powerful tool to provide further insight where experiments may fall short. It is imperative to synergistically use simulations, molecular dynamics, and data science to bridge this knowledge gap. However, a common theme amongst computational studies on DES is the lack of experimental data available to make significant strides in developing generalized predictive models, which is largely the result of a lack of chemical diversity in the literature as many DES systems studied are still overwhelmingly based on ChCl.[36–38] A deeper

understanding of DES is also necessary as they are still poorly understood, especially when determining their feasibility and behavior as electrolytes.[39] The hydrogen bond network formed in DES has direct impact on several key electrolyte properties, which can be influenced by several factors such as molecular weights, QAS anions, and functional groups. However, many of the features that lead to ideal DES electrolytes may not be intuitive to determine, and therefore the development will require optimization, functional design, and new methods to efficiently explore the vast chemical space.

The use of high-throughput experimentation and data-driven strategies for the discovery and optimization of materials has gained significant traction over the past few years, including several studies focusing on electrolytes.[40–43] To our knowledge however, these methods have not been applied towards DES for energy storage. In this chapter, we will explore the use of ROMs and DES electrolytes for RFBs, presenting our approach using high-throughput and data-driven strategies. First, our work evaluates the electrochemical properties of common DES and we demonstrate the preparation of binary and ternary RDES. Afterwards, the use of cheminformatics and engineering metrics is presented as a strategy to probe and outline the design space for DES. High-throughput experimentation strategies begin with modifying the synthesis process for DES to enable rapid sample preparation using open-source, automated liquid handling robots. Electrochemical characterization is then performed in a parallel and high-throughput manner using screen-printed electrodes (SPEs), which requires minimal sample volume and facilitates data collection and analysis. We have demonstrated that this significantly speeds up sample preparation to the order of seconds and allows for a systematic, combinatorial sequence to exploring DES. Embracing these strategies will then allow for future efforts to incorporate machine learning and iterative exploratory campaigns into the design of experiments (DOE) to more efficiently arrive at

new knowledge that will facilitate the design of DES electrolytes, and subsequently RDES, with optimum properties.

5.2 Preliminary Exploration of RDES

A preliminary exploration of RDES was conducted to demonstrate the 'proof of concept' feasibility of these new electrolytes. It was initially desired to demonstrate the increased electrochemical potential windows of DES, which is a major advantage compared to aqueous electrolytes. Four common DES were synthesized by weighing the starting materials at the appropriate molar ratios and heating in a vial until a uniform liquid formed. The four DES consisted of ChCl in a 1:2 molar ratio with Ethylene Glycol (EG), Glycerol (GL), Phenylacetic acid (PAA), and 3-Phenylpropionic acid (PPA). CV was performed at a 100mV/s scan rate on each of the DES using a glassy carbon working electrode with 3mm diameter, a platinum counter electrode, and a silver/silver chloride reference electrode. The results of the CV can be seen in Figure 5.3. When CV is performed on active materials, it is desired to see the formation of peaks corresponding to the redox reactions that occur when an active material transitions between oxidation states. However, when a supporting electrolyte is investigated, reactions corresponding to electrochemical events are not desired. The emergence of significant peaks would indicate an instability of the material, and inhibit it’s use as a supporting electrolyte or electrochemical applications. Looking at the CVs of the DES chosen, the curves are relatively flat in the region between -1.75V and +0.5V. At increased potentials, some peaks are observed, however the magnitude of these peaks is relatively small, between 50 and 100 μA, and thus do not appear to be a significant electrochemical reaction. These DES possess stable potential windows of at least 2.5V, which is about twice as high as that of conventional aqueous electrolytes.

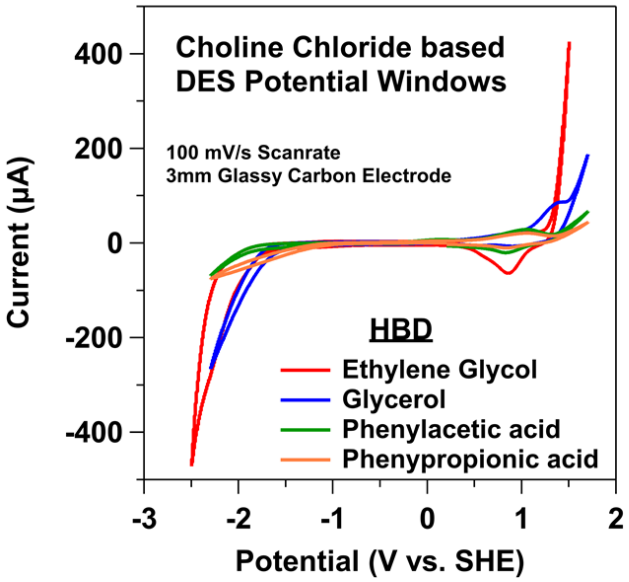

Figure 5.3. CV of four ChCl based DES.

It was also desired to incorporate ROMs to form binary and ternary RDES. First, Ternary RDES were formed based on the 1:2 ChCl: EG DES by addition of a small amount (10mM) of ROM. The ROMs included 1,2-diaminoanthraquinone (1,2-DAAQ), 2-amino-9-fluorenone (2-AF), and 2-hydroxy-1,4-naphthoquinone (2-HONQ), which are organic molecules used previously for colorimetric and fluorometric studies in addition to a natural dye.[44–46] Binary RDES were attempted with the same ROMs listed above using ChCl with molar ratios of 1:2 ChCl:ROM. When heated to the melting point of the ROM, the formation of a liquid state was not observed, instead there was a decomposition of the ROM. However, when attempted with a new candidate, 9-fluorenone-1-carboxylic acid (F1CA), the formation of a liquid was observed. Figure 5.4 and Table 5.2 show images of the RDES and their respective structures.

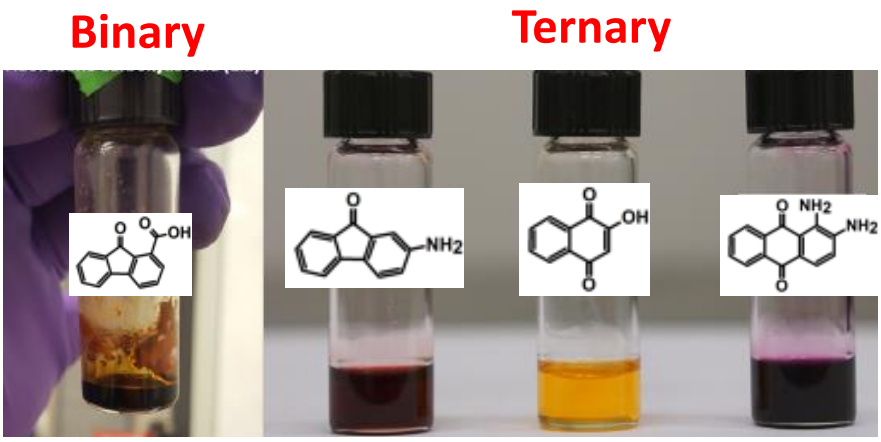

Figure 5.4. Images of binary and ternary RDES formed in the laboratory.

Table 5.2. Structures of choline chloride based binary and ternary RDES.

	ROM	QAS (ChCl)	HBD (EG)
Binary	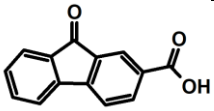 F1CA	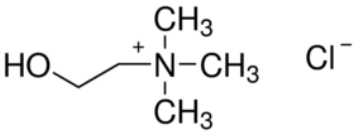	**N/A**
Ternary	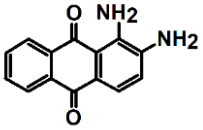 1,2-DAAQ	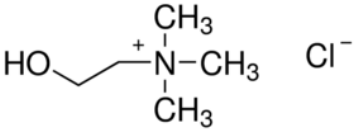	
	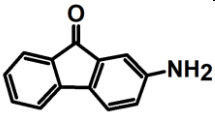 2-AF	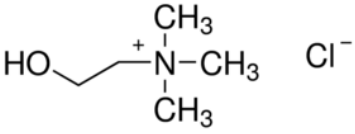	
	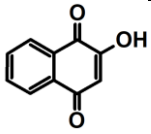 2-HONQ	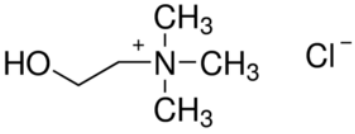	

All of the ternary RDES remained liquid at room temperature, however this was expected as only small amounts of ROM were added and the 1:2 ChCl:EG DES freezes at -66°C. The binary DES formed remained liquid for only a short amount of time after removing it from the heat source. It cannot definitively be concluded that what was formed here was indeed a binary RDES, yet it was intriguing that this sample formed a liquid and the others did not. Nonetheless, this possibility showed promise.

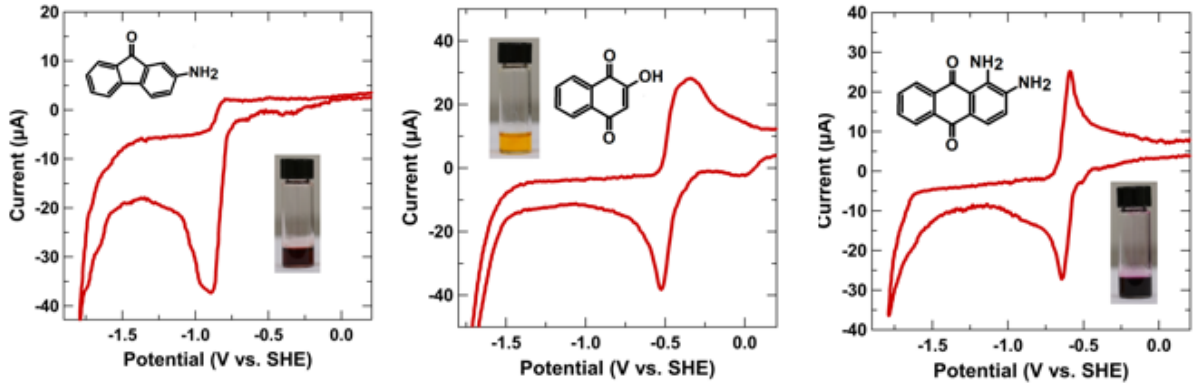

Figure 5.5. CV of ternary RDES. Left: 2-AF. Center: 2-HONQ. Right: 1,2-DAAQ.

Reversibility of the binary RDES was characterized by CV in a standard 3-electrode setup and is shown in Figure 5.5. The 2-AF displayed irreversible behavior, in which only a reduction peak at approximately -0.8 V vs SHE was observed. The CV is rather similar to other irreversible fluorenone CVs discussed earlier in other chapters. The 2-HONQ RDES was pseudo reversible displaying peak couples, yet the reduction peak was much sharper and more pronounced while the oxidation peak was very broad. The 1,2-DAAQ RDES displayed good reversibility with sharp and pronounced reduction and oxidation peaks. Both the RDES based on the 2-HONQ and 1,2-DAAQ ROMs could be categorized as anolytes due to their negative redox potentials. Radical based redox

species such as these have been known to interact with non-aqueous solvents to form unwanted intermediates which could lead to capacity fading under full-cell conditions, which should be taken into consideration.[47] On another note, some studies have suggested that ChCl may degrade after prolonged electrochemical cycling.[48] More in-depth analysis is imperative to gain further insight into possible failure mechanisms.

Following these experiments, it was desired to observe the effects that a high concentration of ROM would have on a ternary RDES, and how this would differ from the pure DES. The four previous DES utilized in Figure 5.1 were chosen. Two ROM called 4-hydroxy-2,2,6,6-tetramethylpiperidin-1-oxyl (4-HO-TEMPO) and 9-fluorenone (FL) were intuitively chosen as candidates for a high concentration RDES. 4-HO-TEMPO has been demonstrated to have good solubility in aqueous systems due to its small size, also showing positive redox activity as a catholyte.[2] This would complement the previous experiments well as the RDES tested were all considered as anolytes. The FL molecule has been seen many times in this paper, and now it will be utilized without any polar functional groups attached. The purpose of this was to shed light as to whether a hydrogen bond donating group is necessary for a ROM to form a RDES. In the case where it is not necessary, this greatly opens the design space of possible ROM candidates, with the potential to incorporate redox pairs that traditionally exist separately in aqueous or non-aqueous systems. As a starting point, CVs of 10mM 4-HO-TEMPO and FL were conducted in 1:2 ChCl:EG DES to compare to those in figure 5.5. The CV of 4-HO-TEMPO demonstrated good reversibility with an extremely high redox potential of approximately 0.9 V vs. SHE. Theoretically, if this was to be utilized as a catholyte and paired with the anolyte 1,2-DAAQ in a full-cell configuration, the open circuit potential for this system would reach nearly 1.5 V. As for FL, it

ultimately received the same fate as the amino functionalized version, producing an irreversible CV, indicating that a similar unwanted reaction mechanism may be occurring.

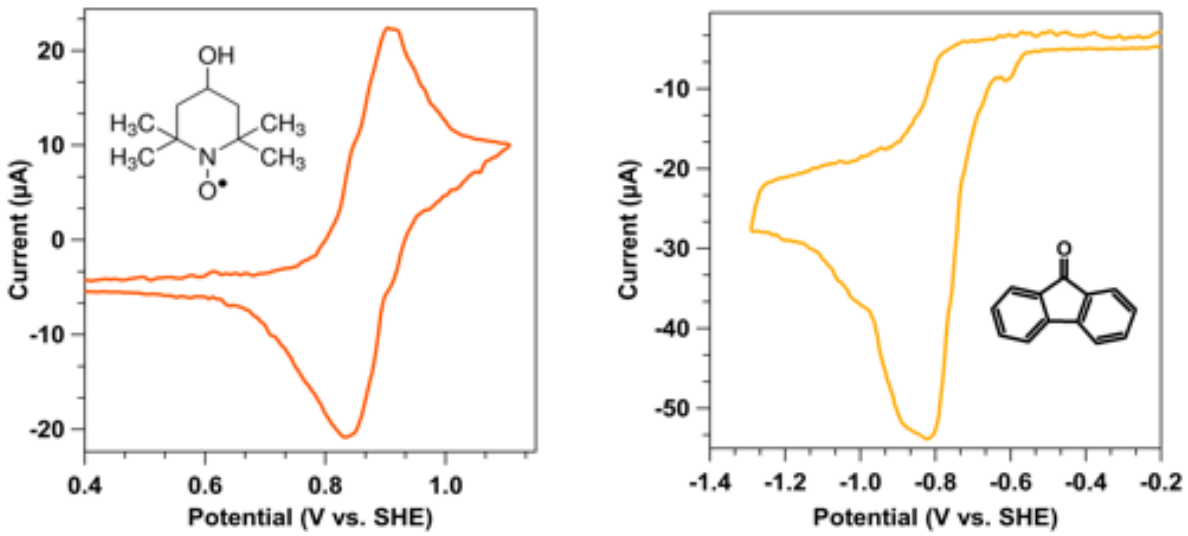

Figure 5.6. CV of 4-HO-TEMPO and FL ternary RDES.

High concentration RDES were made by adding enough 4-HO-TEMPO and FL to 1mL of DES in a vial to constitute a 1.5 M concentration of the ROM. To accelerate the dissolution process, a stir bar was added to the vial and placed in a sand bath on a hotplate at 55°C. The 1.5 M 4-HO-TEMPO fully dissolved in all the DES (ethylene glycol, glycerol, PPA, PAA). As for the FL, a full 1.5M concentration was only achieved in the DES based on PPA and PAA. After the high concentration RDES was formed, the samples were allowed to equilibrate at room temperature (~21°C), and it was observed whether the RDES froze. The results are shown in Table 5.3.

Table 5.3. Physical state of high-concentration RDES at room temperature.

ROM	QAS (ChCl)	HBD	Room Temperature State
4-HO-TEMPO 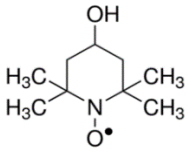	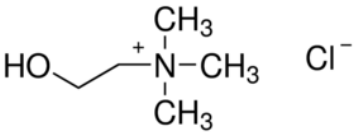	EG 	**Solid**
	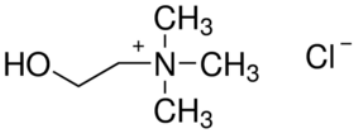	Glycerol 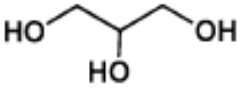	**Solid**
	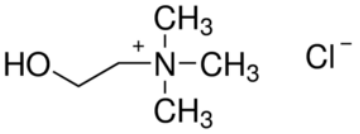	PPA 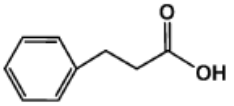	**Gel**
	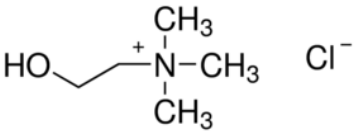	PAA 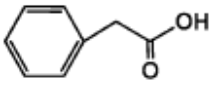	**Liquid**
FL 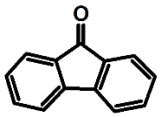	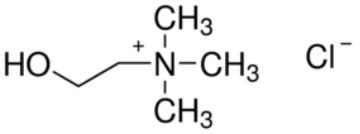	PPA 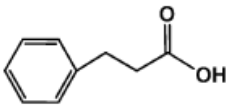	**Solid**
	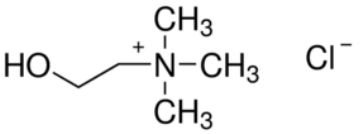	PAA 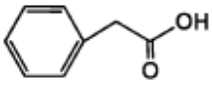	**Solid**

While a 1.5M FL RDES was possible with PPA and PAA based DES at elevated temperatures, they both solidified once allowed to equilibrate to room temperature. Still, it is interesting that the solubility for this ROM was more favorable with the PPA and PAA. In contrast, a 1.5M RDES concentration was obtained with 4-HO-TEMPO with all of the pure DES. Ethylene glycol and glycerol-based DES solidified at room temperature, while the PPA based DES was classified as forming a gel since it appeared to possess both solid and liquid qualities. The real surprise however was that the RDES formed with 4-HO-TEMPO and PAA remained in the liquid state. Referring to Table 5.1, the PPA based pure DES has the highest freezing point (25°C) out of all the other DES used for this experiment. One may have guessed that this RDES would have surely solidified due to the high concentration of ROM and slightly cold environment of the room (18°-19°C), yet this was clearly not the case. This is proof that interactions between the ROM and pure DES are very likely to occur in RDES and whose physical properties may significantly deviate from literature values specified for the pure DES. Thus, it is insufficient to assume that the properties of a pure DES will remain consistent after a ROM is added. Experiments therefore should be conducted at multiple molar ratios of each component to get a true view of how the properties for a RDES change at varying compositions.

The use of RDES as cost effective and high energy density materials for RFBs shows promise from these preliminary explorations. However, this represents such a miniscule portion of the possible design space. The next section will discuss in detail the proposed high-throughput experimental techniques, parallel analysis, and data science methods that will accelerate the characterization and screening process for these materials moving forward.

5.3 Data-Driven Strategies to Outline Design Space

In many situations where the design space for a materials problem is incredibly large and knowledge of these materials is limited, approaches to outlining the design space can provide insight for developing design of experiments (DOE).[49,50] With regards to DES, possible candidates for HBD consist of large families of molecules such as alcohols, polyols, amides, carboxylic acids, etc., and in addition many different QAS exist with varying alkyl chain lengths and anion species. Despite the rich materials space for DES, the diversity of candidates studied in the literature is rather low. Our goal here was to probe the commercially available design space for these materials via a cheminformatics campaign, prior to performing any experimental procedures. This would allow for the informed selection of a set of possible candidates to investigate. Moreover, demonstrating the application of engineering metrics and design constraints to filter and rank materials aids in assuring the most promising candidates are highlighted for experimental investigation. The ability to effectively outline a material design space is essential to DOE development, and while our investigation is focused on DES, we present this approach as a strategy that can be applied to virtually any materials problem.

The first step in this process was to procure a basis set of known QAS and HBD that have been successfully used in the literature to form DES. The National Institute of Standards and Technology (NIST) is an excellent resource for publicly available material databases, and their ILThermo database contains extensive data for DES.[51] In total over 2,000 datapoints were obtained for several physiochemical properties across a variety of DES. In addition to ILThermo, a DES melting point dataset was obtained from a concise review text.[52] The datasets were all compiled, and 36 unique QAS and 75 unique HBD were extracted.

A starting point from which to identify similar but non-intuitive QAS and HBD that have not been described in the literature was now possible. The concept was to perform an iterative structural based similarity search across each of the QAS and HBD in the basis set. This would require a platform capable of efficiently applying cheminformatics methods and subsequently querying a large chemical database. For this reason, PubChem's open-source Python wrapper (PubChemPy) and Power User Gateway Representational State Transfer (PUG-REST) was chosen due to its relative simplicity and ability to access PubChem's data and services. PubChemPy allows for Python based interaction to retrieve chemical identifiers, physiochemical property data, and perform chemical similarity searches, among other uses.[53] While PubChemPy is a wrapper for their PUG-REST API, the PUG-REST itself can be utilized via a URL-based format and is complimentary in this application to retrieve other data of interest that is not readily accessible by PubChemPy.[54,55] Compound id's (CID), which are PubChem's unique identifiers, were obtained for the basis set. From these CID's, virtually any information available in PubChem's database can be queried. SMILES strings, which are common linear notations to describe chemical structures, were used to initiate a 2D structural similarity search for each material in the basis set. The PubChem similarity search begins by converting the SMILES strings to molecular fingerprints, which are another popular method to represent chemical structures using binary vectors.[56] Here, each vector position represents a chemical substructure or feature, whose absence or presence is denoted with a 0 or 1, respectively. While several variations of molecular fingerprints exist, PubChem uses their own variation which consists of a binary vector of length 881, with predetermined substructures in each vector position.[57] After the fingerprints are obtained, they are then compared to the fingerprints of all other compounds available in the PubChem database and their similarity is judged by the Tanimoto scoring index. The Tanimoto index

considers the proportion of substructures or features that are shared between the two compounds to give a score of similarity. While many other methods to quantify molecular similarity exist, the Tanimoto index is one of the most highly regarded.[58] A threshold can be specified in the PUG-REST API for the similarity search to only return compounds that are above a specific similarity score. In our search, a similarity threshold of 85% was used to ensure a balance between results that are adequately similar from the initial compound, but still yield some diversity. In addition, the search was specified to return a maximum of 3,000 results per search to avoid timing out the request on PubChem's servers.

The search resulted in 68,127 and 4,705 complimentary HBD and QAS candidates that were returned from the initial basis set. After growing the space of potential candidates significantly, it was necessary to constrain it according to metrics that are important to our application. For example, only candidates that are readily and commercially available for procurement were to be considered, to avoid the need for synthesis. In this regard, vendor information was extracted from the PubChem database and scripts were developed to filter candidates that were not commercially available. The ability to characterize the environmental and human health hazards of the candidates is another metric deemed important for this work, and therefore safety information from the Globally Harmonized System of Classification and Labelling of Chemicals (GHS) was also extracted. Those candidates that had no GHS safety information available in the database were filtered and removed. Figures 5.7 and 5.8 below show the subsequent growth and constraint of the design spaces for the QAS and HBD. The visualization was created by representing each of the candidates using Morgan fingerprints. Unlike the PubChem fingerprints used for the similarity search, each bit in the vector for Morgan fingerprints is not constrained to a predefined structure, but instead uses a complex algorithm to generate the

bit vector.[59] The length of the vector can also be specified, and a length of 2,048 bits was selected to obtain more structural information on the candidates. To project this high dimensional information on a two-dimensional space, Principal Component Analysis (PCA) was used, which is a popular dimensionality reduction technique for visualization.[60,61] The final basis set after applying constraints resulted in 3,477 HBD and 185 QAS.

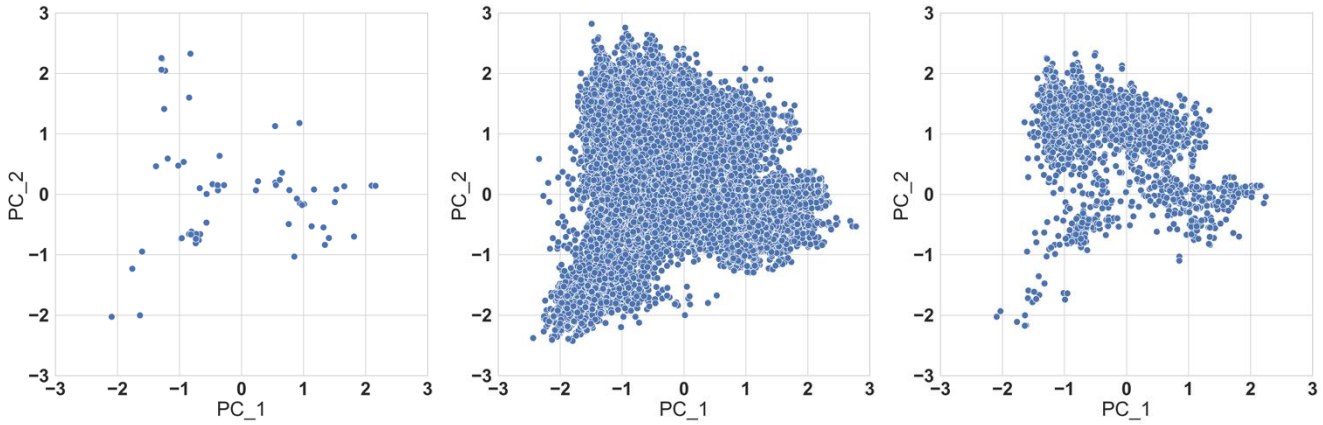

Figure 5.7. Cheminformatics campaign for HBD species. Left: Web-scraped candidates. Center: Candidates from similarity search. Right: Final candidates after applying constraints.

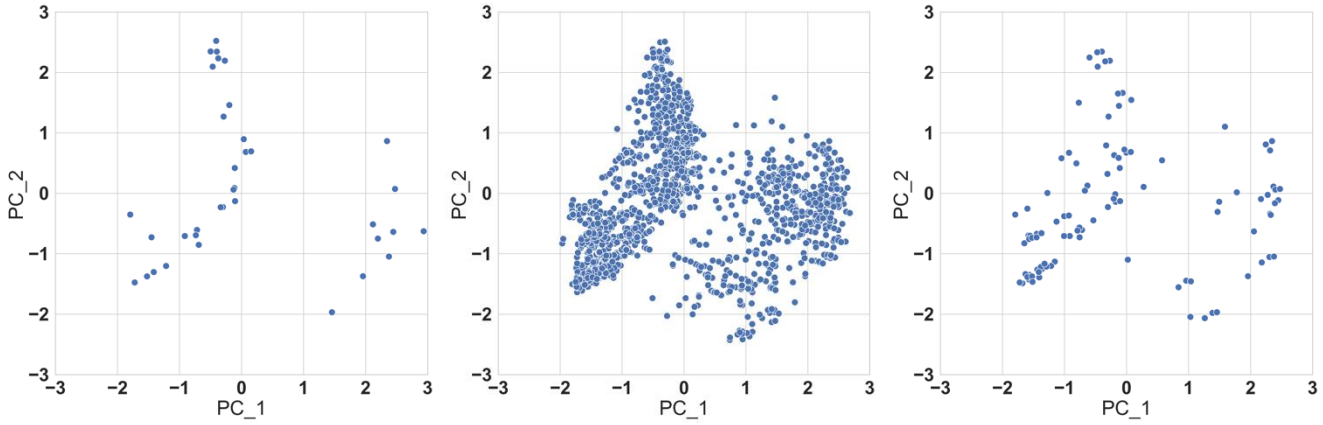

Figure 5.8. Cheminformatics campaign for QAS species. Left: Web-scraped candidates. Center: Candidates from similarity search. Right: Final candidates after applying constraints.

With the final design space being defined, a ranking system based on various engineering metrics was developed to highlight the candidates with the most favorable properties and characteristics. The ranking system considered scores based on GHS safety hazards (health, environmental, physical) and chemical intuition from the candidates in terms of their molecular weight. GHS safety scores were developed based on previous examples in the literature, with regards to the specific hazard codes and the severity of the hazard they represented.[62] As for the molecular weight, QAS and HBD with lower molecular weights will generally possess lower melting points as a DES, and so this was a favored characteristic. The molecular weights and GHS safety scores were all normalized, and a modified digital logic method was utilized to assign a pre-factor to each of the metrics, which determines the weight that each metric contributes towards the rankings. The pre-factor is assigned based on a comparative importance of each of the metrics with each other. For example, health hazards were regarded as the most important metric compared to the others, and as such received the highest pre-factor. This digital logic method has been commonly used for ranking engineering metrics for a wide variety of material sections.[63]

With each of the candidates now ranked in the design space, it is possible to visualize this molecular space along with each of the candidates' rankings. However, we see from the previous visualization that while the size of the molecular space is apparent, clusters or groupings of candidates by their molecular structures are not. This is because the PCA that was applied only utilized the two most important principal components, resulting in some loss of the structural information contained in the Morgan fingerprints. To recover that information, it is necessary to increase the variance by increasing the number of principal components. However, that once again poses a challenge in terms of visualizing a high-dimensional space. To solve this problem, a non-linear dimensionality reduction technique called t-distributed stochastic neighbor embedding (t-

SNE) was proposed, which is better suited for describing greater variance in data.[64,65] The number of principal components in the PCA that was applied to the original dataset of Morgan fingerprints was increased to 50 and reduced to a two-dimensional plot with t-SNE. Figure 5.9 below shows the resulting t-SNE plots with the HBD and QAS. As for the HBD, clearly distinct clusters of molecules with similar structure are observed. The clusters in the QAS are not as clear given the smaller number of molecules in that dataset, yet some distinctions can be made. In addition to these plots, an accompanying python script was written to interactively visualize the space and directly select areas to view the molecular structures and corresponding rankings. With this work, the design space for the future high-throughput experimentation methods has now been outlined.

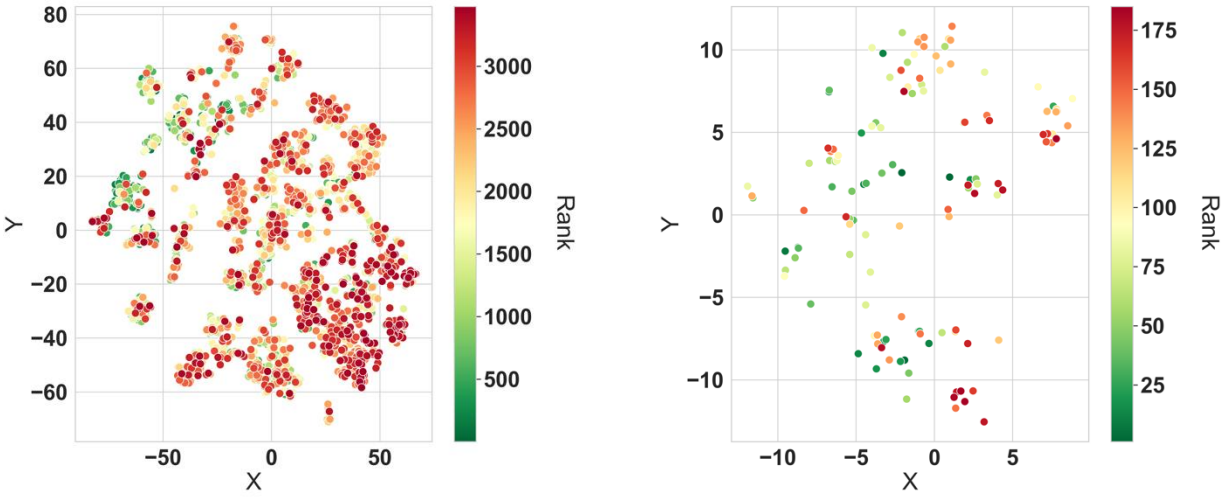

Figure 5.9. t-SNE plots of HBD (left) and QAS (right) molecules in the final basis set.

5.4 HIGH-THROUGHPUT EXPERIMENTATION METHODS FOR DES

5.4.1 *High-Throughput DES Synthesis*

An advantage of DES is that their synthesis is relatively straightforward, simple, and cost effective. Samples are prepared in the traditional method by adding the pure QAS and HBD components together in vials at the appropriate molar ratio. While some of these components are liquid in their pure form (i.e., ethylene glycol, glycerol, trifluoroacetic acid) the majority are solids. Samples are then heated and stirred until they result in a uniform liquid and are allowed to cool. While the approach is suitable for investigating a small quantity of DES at a time, this method quickly becomes inefficient when attempting to explore a larger combinatorial space. Instead, a platform to synthesize DES in a high-throughput and parallel manner has been developed. The synthesis of DES can be adapted to a high-throughput process by first preparing concentrated stock solutions of QAS and HBD in volatile solvent, with either water or ethanol being utilized depending on which yielded the greatest solubility for the starting material. Generally, a solubility of 1M or greater is sufficient, but higher concentrations are desirable as that will result in the use of lower volumes of stock for each synthesis. Next, instead of manually mixing the components, a liquid handling robot such as the Opentrons OT-2 can be utilized to prepare the mixtures of QAS and HBD. The OT-2 is completely open source and programmable via the Opentrons Python API. Concentrations of the stock solutions along with the desired molar ratio of QAS and HBD mixtures are fed into a python script that first calculates the correct volumes of stock solution to dispense to achieve the desired DES composition using the system of equations below:

$$V_{QAS} + V_{HBD} = V_{Total} \tag{5.1}$$

$$\frac{C_{QAS}*V_{QAS}}{(C_{QAS}*V_{QAS}+C_{HBD}*V_{HBD})} = X_{QAS} \tag{5.2}$$

$$\frac{C_{HBD}*V_{HBD}}{(C_{QAS}*V_{QAS}+C_{HBD}*V_{HBD})} = X_{HBD} \tag{5.3}$$

In equation 1, V_{QAS} and V_{HBD} are the volumes of QAS and HBD stock solution to dispense, and V_{Total} is the final desired total volume of each mixture. Equations 5.2 and 5.3 are analogous to expressions for the mole fraction of a two-component mixture, where C_{QAS} and C_{HBD} are the molar concentration of the QAS and HBD stock solutions, and X_{QAS} and X_{HBD} are the mole fractions of QAS and HBD to produce the desired DES composition. Knowing the total desired volume of mixture, concentration of stock solutions, and molar composition of the DES to synthesize, this becomes a system with 3 equations and 2 unknowns which can be solved trivially. Once the volumes of stock solutions to dispense are calculated by this script, they are then passed on to protocol scripts which contains hardware specifications and commands for the OT2 to perform. The OT-2 has 11 customizable slots to hold a variety of hardware, including pipette tips, stock solutions, and vials. Samples can be prepared in a variety of standard multi-well plate formats. In addition to these standards, a custom format from which to synthesize DES was designed. Custom 48-well plates were designed using a 3-D resin printer (FormLabs Form 3) with a temperature-resistant resin that is stable up to 238°C. The custom well-plates are designed to hold 2mL glass scintillation vials in each well. Preparing the DES in vials allows the ability to still

incorporate aspects of the traditional synthesis into our high-throughput methodology, while also aiding in preserving and storing the samples for characterization later in the pipeline. The OT-2 will directly dispense the correct combination of stock solutions into the vials, and samples prepared in the custom 48-well plate format consisted of a total mixture volume of 600μL.

After samples are prepared it is necessary to remove the volatile carrier solvent so that only the QAS and HBD remain. This is done via a series of gentle evaporation and heating steps. Once mixtures are created in the OT-2, all samples are moved to a large commercial dehydrator (Cabela's 80L SKU: 2517102) for a gentle evaporation step at 65°C for at least 24 hours. This initial step removes most of the carrier solvent. Samples are then heated in an oven at 100°C for 30 min, which gives a higher evaporation rate and ensures the formation of a homogeneous mixture, as reports have indicated heating below 80°C may resulted in the formation of precipitates or crystals upon cooling. Finally, samples are cooled and then dried under vacuum at ambient temperature for 30 min to remove any residual carrier solvent, and afterwards stored in airtight desiccators until screening and characterization is performed. Figure 5.10 shows a schematic of the high throughput DES synthesis procedure.

To demonstrate the high-throughput capabilities of this process, a variety of DES based on 4 QAS and 10 HBD were prepared, the structures of which can be seen in Figure 5.11. This selection was composed of QAS and HBD that are common in the literature, in addition to being selected from the investigation on the outlined design space. This gives a possible combination of 40 DES that could be prepared. It is important to note that while many of these materials have been reported in the literature, the total combinatorial space has not been investigated to the fullest potential. For example, nearly all HBD species selected in this set have been paired with choline chloride to form DES.[20,66–69] Here, we have broadened the investigation to other QAS besides

choline chloride, of which many combinations have never been studied. Therefore, prior to even delving into the expanded design space, there is an abundant combinatorial space that needs to be investigated just from materials that have already been reported in the literature. This high-throughput system is suited to tackle that challenge. For this combination of QAS and HBD, it was desired to prepare 12 molar compositions of each, which would result in a total of 480 samples to be prepared. The campaign was split into two separate runs: the first including acetylcholine chloride (AcChCl) and tetraethylammonium chloride (TEAC) with all 10 HBD, and the second including tetrapropylammonium bromide (TPAB) and tetraethylammonium iodide (TEAI) with all 10 HBD.

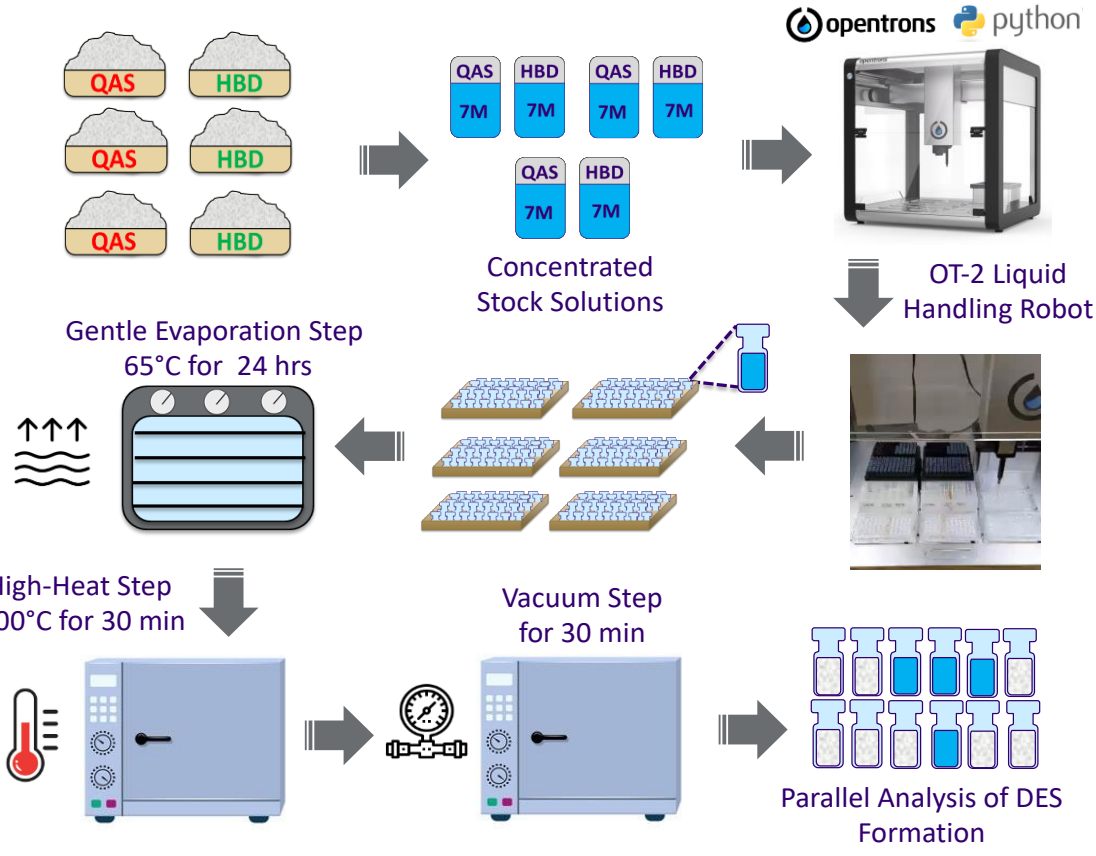

Figure 5.10. Schematic Illustration of high throughput DES synthesis

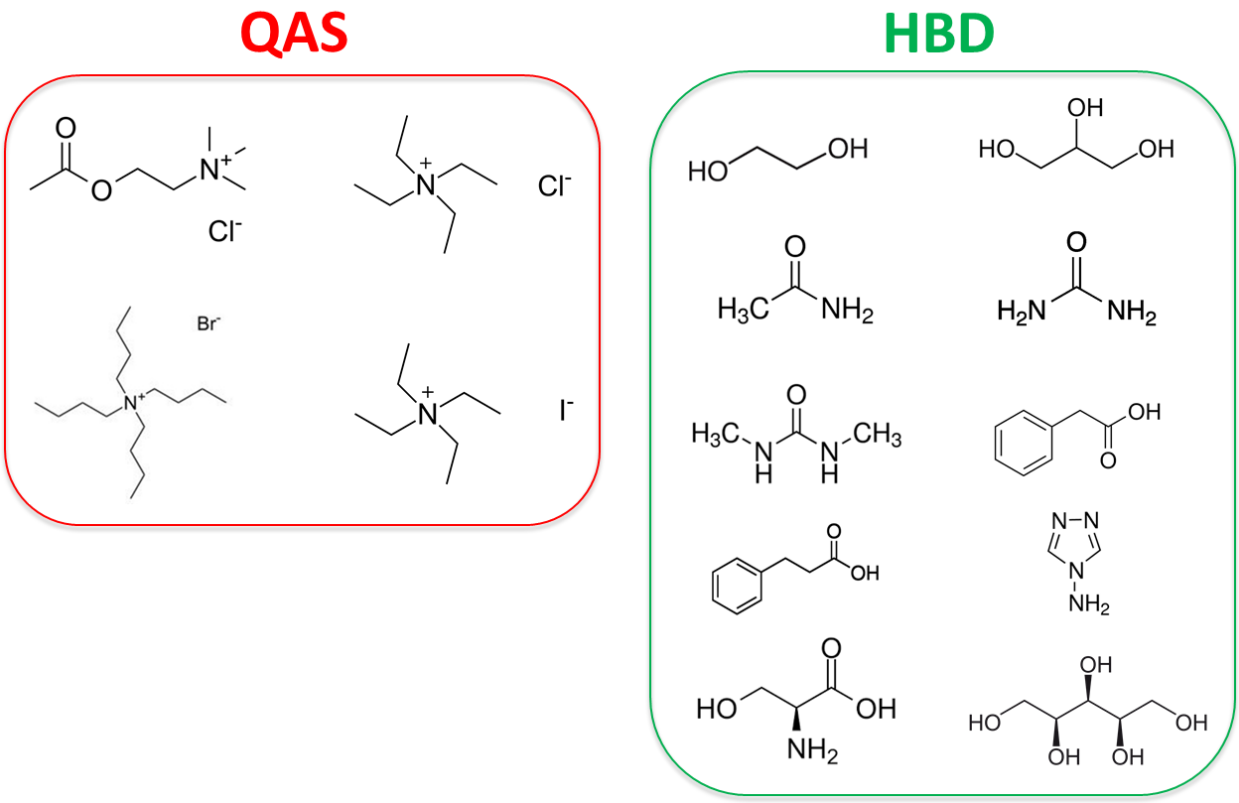

Figure 5.11. Structures of QAS and HBD used in high-throughput DES synthesis. QAS: Acetylcholine Chloride, Tetraethylammonium Chloride, Tetrapropylammonium Bromide, Tetraethylammonium Iodide. HBD: Ethylene Glycol, Glycerol, Acetamide, Urea, N,N-Dimethylurea, Phenylacetic Acid, Phenylpropionic Acid, 1,2,4-amino-4H-triazole, Xylitol.

As mentioned, the OT-2 has 11 slots on its deck for labware and hardware. For each run, 5 of the slots contained the custom 48-well plates which hold 2mL scintillation vials. The maximum sample volume in each vial was 600 µL, yet different volumes of each DES stock combination are necessary to achieve the maximum volume based on the molar composition desired and stock concentration. The OT-2 has several pipettes that are capable of transferring volumes of 1-1000 µL and depending on the volumes necessary to carry out the synthesis for each combination, it is possible to use two pipettes simultaneously that cover a complimentary range of

volumes. Here, the P1000 and P300 pipettes are utilized, which together cover volume ranges of 20-1000 µL. For each pipette, a tip rack is required, which holds 96 tips for the respective pipette, and two tip racks per pipette were utilized to ensure there are enough tips to carry out the synthesis. Stock solutions for the QAS and HBD were contained in 20 mL scintillation vials, and the OT-2 pipette transfers volumes from these stocks into the 2 mL scintillation vials to make the DES mixture. A diagram of the fully loaded OT-2 deck is shown in Figure 5.12.

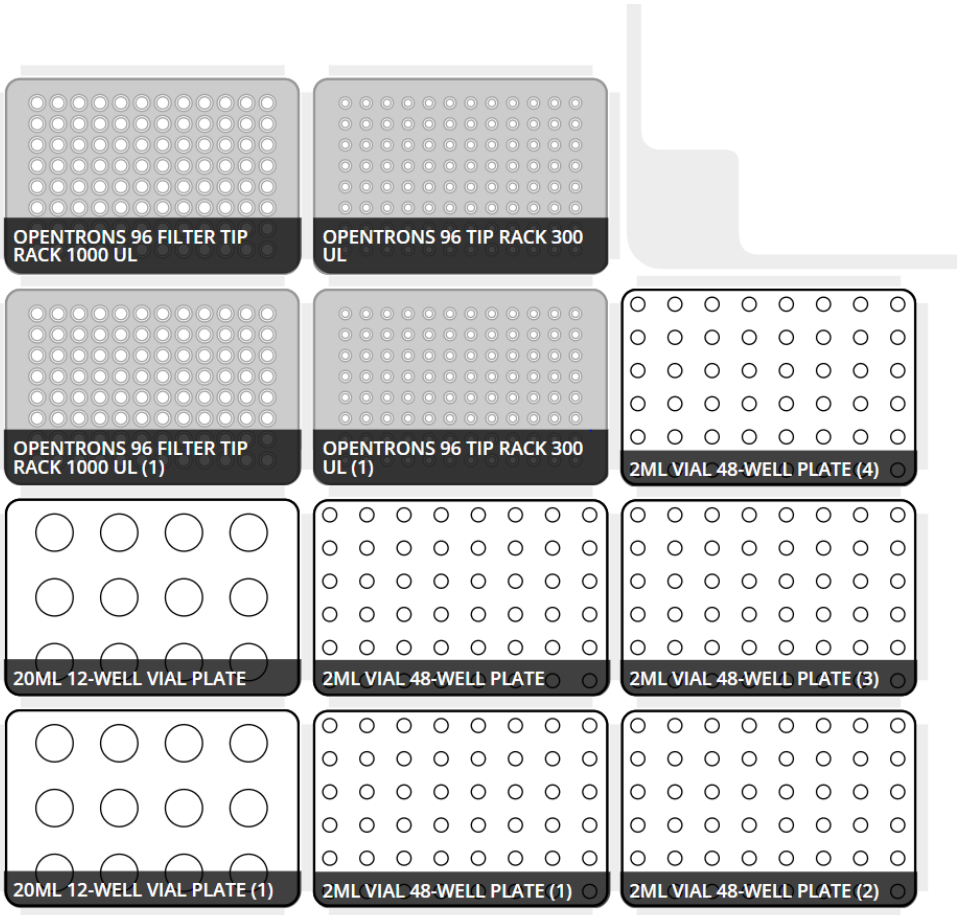

Figure 5.12. Diagram of Opentrons-OT-2 deck during high-throughput DES synthesis. Two tip racks are used per pipette, stock solutions are contained in 20mL vials in a 12-well plate, and stock solutions are transferred to 48-well plates containing 2mL vials. The deck configuration maximizes sample output utilizing all 11 labware slots available.

Each run in the campaign required a total of 253 minutes to prepare 240 samples, which is just over 1 minute per sample. This clearly demonstrates the high sample throughput of the system. After samples were processed through the evaporation, heating, and vacuum steps, it was noted that samples containing AcChCl, TEAC, and TPAB as QAS formed liquids at room temperature with some of the HBD tested. In contrast, all samples containing TEAI as a QAS did not form a liquid at room temperature with any HBD combination.

5.4.2 *High-Throughput Electrochemical Characterization*

The ability to screen and identify DES electrolytes in a high-throughput manner with high ionic conductivities and wide electrochemical potential windows will be crucial. However, most electrochemical measurements are still conducted with bulky electrodes and relatively large

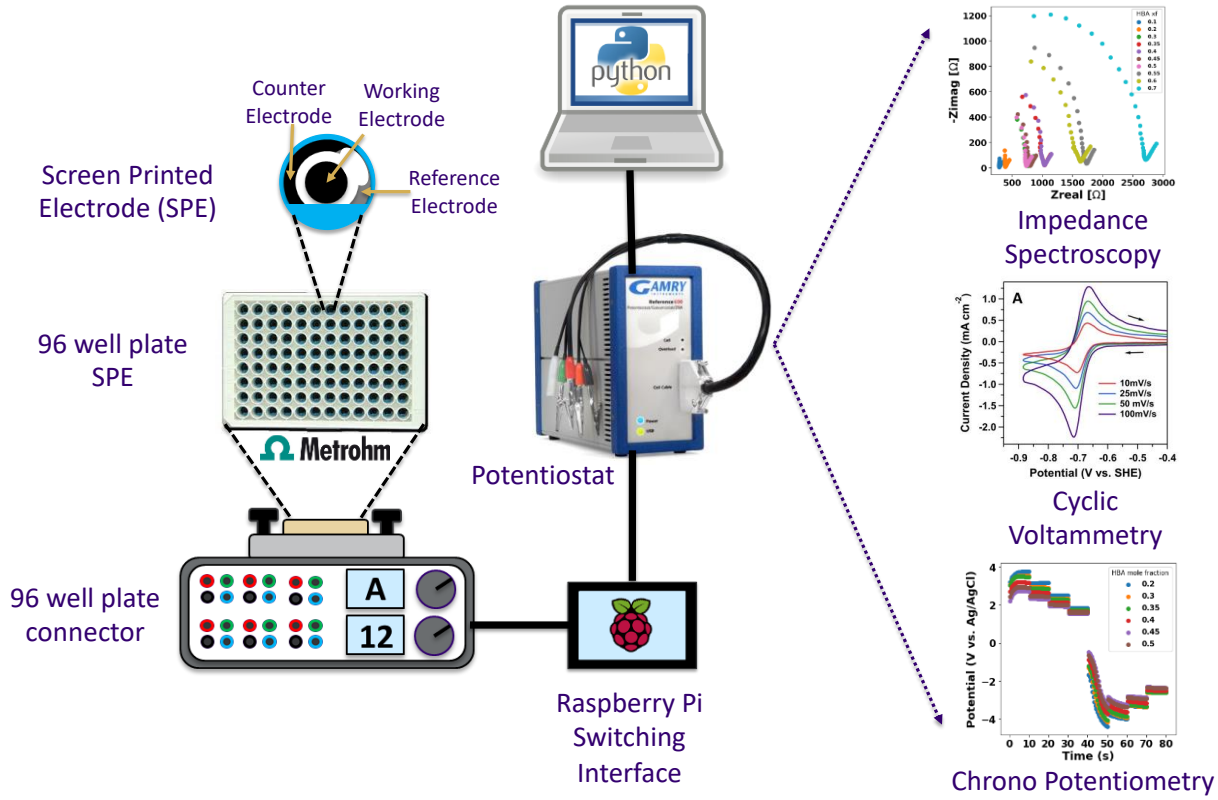

Figure 5.13. Schematic illustration of the high-throughput electrochemical setup for DES characterization.

sample quantities that are not conducive for screening large design spaces. To characterize electrochemical properties of DES, a high-throughput platform based on the use of SPEs that require minimal sample volume and are ideal for conducting measurements of multiple samples in shorter periods of time. The throughput of these SPEs can be increased further by arranging them in a 96-well plate system, and moreover direct interface with standard electrochemical equipment is possible, converting them into a high-throughput platform for parallel data collection and batch analysis. A schematic of this setup is shown in Figure 5.13.

The high-throughput setup is centered around a Gamry Reference 600 potentiostat which performs all electrochemical measurements on the samples. The Gamry is operated by its Windows based Framework software which contains all available scripts to initiate the experiments. While these are typical components used in any traditional measurements, the adaptation to a high-throughput system begins with the choice of electrodes. In previous chapters, measurements performed with the Gamry incorporated a 3mm glassy carbon working electrode, platinum wire counter electrode, and liquid Ag/AgCl reference electrode. This traditional setup typically required approximately 15-20mL of sample, and it was necessary to clean all electrodes following each measurement, as well as polishing of the working electrode to ensure an active surface free of contaminants from the previous sample. This was a rather time consuming and wasteful process in terms of the sample volumes necessary to prepare beforehand. Instead, these standard electrodes have been replaced using SPEs configured in either a single-cell or 96-well format, procured from Metrohm-DropSens. The single-cell configuration consists of the Metrohm-DropSens DRP-11L SPE which is interfaced directly with the Gamry via the Metrohm-DropSens CAC4MMH connector. The DRP-11L is a low cost and disposable compact 3-electrode SPE which is ideal for working with sample volumes of approximately 100 µL and consists of a 4mm

diameter carbon working electrode, carbon counter electrode, and a screen-printed Ag/AgCl reference electrode. These electrodes are arranged on a 3.4 x 1.0 x 0.05 cm ceramic strip with silver electrical connections. The ability to use a greatly reduced sample volume and avoid the need to clean and polish the electrodes after every use greatly increases the speed at which measurements can be conducted. While the single-cell configuration is already a significant improvement upon previous practices, a 96-well configuration using the Metrohm-DropSens 96x110 SPEs can further increase throughput. These consist of an array of 96 SPEs that are attached to the bottom of a standard 96-well enzyme-linked immunoabsorbent assay (ELISA) microplates. The electrode materials can be similarly configured to those of the single-cell format, with the working electrode having a slightly smaller diameter of 3mm. Gold plated contacts are found at the bottom of the 96x110 plates to provide the electrical connection for each SPE. These electrochemical ELISA plates are interfaced with the Gamry using the Metrohm-DropSens CONNECTOR96x, which can change the electrical connection of each well manually to perform experiments on the entire assay. However, a much more efficient method of using this SPE configuration is to include the use of a Raspberry Pi based controller, provided by Metrohm as the SYNCONN96x. This controller allows the ability to automate the switching of the electrical connection for each well. A cable connected to the IO port on the Gamry sends a voltage signal to the SYNCONN96x, which then sends a subsequent signal to the CONNECTOR96x and switches the electrical connection of the ELISA plate. Moreover, with the ability to program series of experiments on the Gamry using their sequence wizard, a near fully automated electrochemical test station is possible. However, while attempting to introduce the 96 well plate system, significant troubleshooting was necessary. The electrochemical array board is attached to the plastic ELISA plate by an adhesive. When this system was initially procured, defects in the fabrication of the

plate resulted in sample leakage of water-based electrolytes while experiments were running in the CONNECTOR96x, subsequently damaging the instrument. This concern was expressed to the manufacturer, and while the quality control was improved, it is noted that non-aqueous electrolytes based on organic solvents should be avoided to prevent dissolving the adhesive. This limited the synthesis of DES in the high-throughput method to be carried out in only standard labware and transferring to the electrochemical ELISA plate after the samples are processed with the evaporation and heating steps. In addition to concerns with the ELISA plates, the reliability of the CONNECTOR96x system also came into question on multiple occasions. The initial system that was damaged by the leaking ELISA plate was replaced, however during testing of the new system, there was malfunctions in terms of an inability to switch the electrical connection of a new well on the ELISA plate after receiving the voltage signal from the Gamry before a new experiment. This issue essentially defeats the purpose of the entire system since the only solution was to manually switch well connections after experiments. After lengthy discussions with the manufacturer, a second replacement system was ultimately obtained. While this last replacement system finally seemed to perform appropriately, one final aspect to take note of is the general compatibility of this system with electrochemical equipment from manufacturers other than Metrohm. Metrohm advertises their high-throughput electrochemical hardware to be used alongside their own potentiostat, the STAT8000. This potentiostat allows for seamless integration into the rest of Metrohm's equipment, yet in this situation where a much more powerful potentiostat is already owned (Gamry reference 600) purchasing the STAT8000 would be a downgrade in terms of the bandwidth of electrochemical experiments possible. Therefore, we requested integration of Metrohm's equipment with our Gamry, which required the manufacturing of a custom cable to connect the two systems. Integration of these two systems was possible yet

challenges with reliable communication have persisted. It is noted that on certain occasions there is a delay in the CONNECTOR96x to switch electrical connections between wells after receiving the voltage signal from the Gamry, resulting in switches being made mid-experiment which can completely disrupt sample characterization. This delay is also more prevalent during CV, and a workaround has been to order the series of experiment very carefully to ensure this delay is considered. The troubleshooting described here took place during a significant portion of the experiments that will be discussed later, and as such a majority of them were conducted using the single-cell SPE system, which proved to be significantly reliable on a repeatable basis. Despite this, use of the 96-well electrochemical ELISA plate still has the potential to significantly increase the throughput of electrochemical investigations, and will certainly be a key-instrument in future research taking place in the laboratory.

To reiterate, two of the main properties that will be investigated for assessing the performance of DES electrolytes are high ionic conductivities and wide electrochemical potential windows (also sometimes referred to as the electrolyte stability window). Electrochemical impedance spectroscopy (EIS) was applied to obtain the ionic conductivity. As discussed in previous chapters, EIS is a non-destructive technique that allows for the measurement of the overall impedance (resistance) of a system in response to either a small current or voltage input perturbation. For these DES electrolytes, a small voltage perturbation of 50 mV was applied, and the frequency was spanned from 100kHz to 100 Hz, with a total of 10 points per decade. The ionic conductivity is extracted from Nyquist plots in an identical manner to what was demonstrated previously for sol-gel membranes, where the intersection of the curve with the zero axis of the imaginary portion of the impedance yields the pure, ohmic resistance of the system. The non-parallel arrangement of the electrodes in the single-cell configuration however requires that a

calibration curve be used to accurately convert resistances to conductivities. Therefore, calibration curves were obtained by running EIS on standards of known conductivities of 84, 443, 1413, 2764, and 12880 µS/c with the single-cell SPEs. The resistances of each standard obtained from the EIS measurement were plotted against the resistivities, which is obtained from the inverse of the conductivities (which again, is a known value for the standards). A line of best fit was applied to the data, and the resulting equation from the fit can be utilized to obtain an appropriate resistivity from resistances obtained using the single-cell SPEs. This calibration curve can be seen in Figure 5.14.

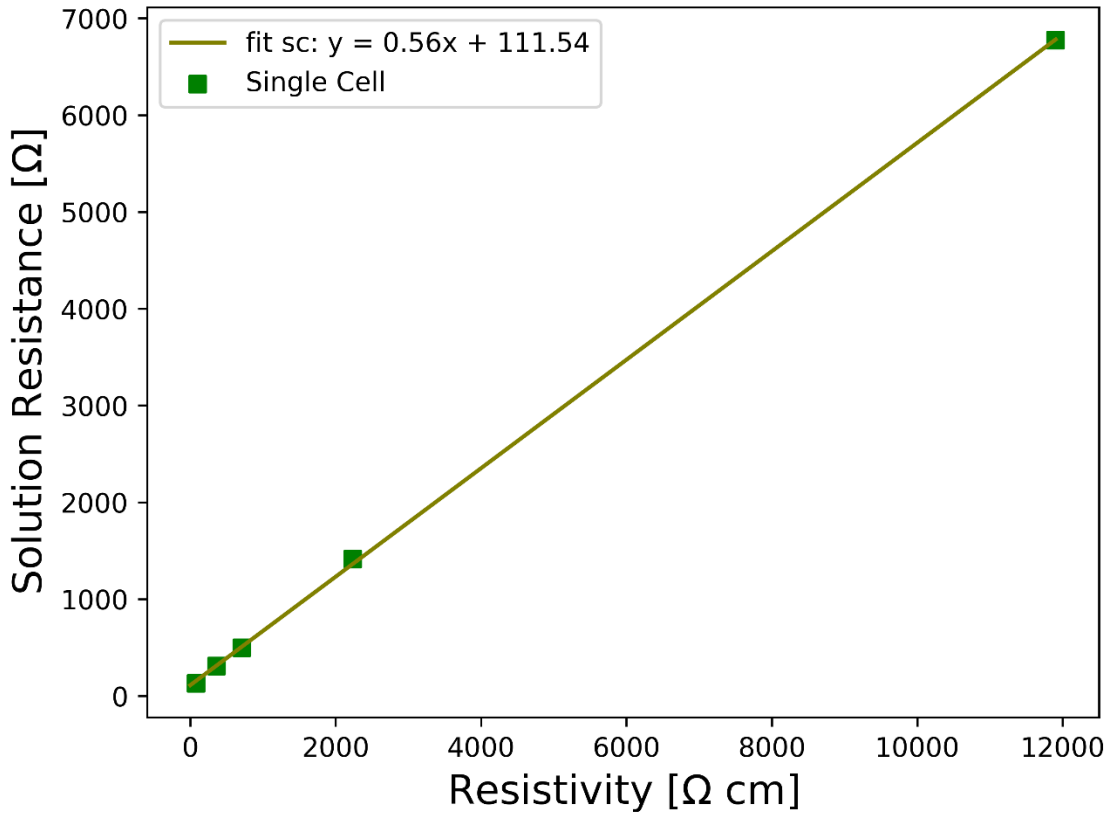

Figure 5.14. Calibration curve obtained from performing EIS on a series of conductivity standards on single-cell SPEs. From the equation obtained from the linear fit, resistivities can be obtained for resistances measured using the single-cell SPEs.

As for determining the electrochemical potential window, a combination of chronopotentiometry (CP) and CV was performed. Typically, CV is performed when the potential window of an electrolyte is desired to be obtained. However, as outlined in Chapter 2, the use of multi-step CP is an attractive alternative to determine limiting reduction and oxidation potentials, having previously been applied by Whitacre et al. to investigate potential windows of aqueous electrolytes for lithium ion batteries in high-throughput.[43,70] For these CP experiments, a series of four fixed positive currents of 1, 0.75, 0.5, and 0.25 mA was applied, followed by applying negative currents of the same magnitude. The first positive and negative current step is held for 15 seconds as an initial conditioning step, and the remaining current steps are all held for 10 seconds. The voltage response of these shorter current steps will equilibrate towards the end of the measurement, and the potentials from the last two seconds of each of these steps is averaged and extracted. Data is collected every half second during each of these measurements. Plots of current density vs potential are utilized to estimate the limiting reduction and oxidation potentials, as described in further detail in Chapter 2 previously. It is important to note that while Whitacre et al. was able to explicitly define these regions as the oxygen and hydrogen evolution reactions, in a non-aqueous system such as for DES, the nature of the limiting reactions is not intuitive. Therefore, CV was performed as a complimentary technique to potentially gain insight into the nature of these reactions and investigate the possibility of undesired electrochemical side reactions in between the limiting potentials. CV measurements were performed at 100mV/s scan rate, spanning voltages from -2V to 2V, for a total of four complete cycles per sample to ensure equilibration. Performing multiple cycles, or sweeps, during CV when investigating DES is important as electrochemical activation of the electrode surface in the first few cycles may cause peaks to be larger. This was noted by Fuchs et al. where multiple CV sweeps of a ChCl:EG DES

on graphene electrodes showed diminishing peaks with each sweep as the surface activity of the electrode equilibrated.[71]

The DES synthesized in the high-throughput process were then characterized by these electrochemical methods. Only samples that were liquid at room temperature were characterized, as there were no temperature control elements incorporated into the high-throughput setup at the time of writing. As mentioned, only samples consisting of AcChCl, TEAC, and TPAB as QAS had samples that were liquid at room temperature. No samples consisting of TEAI as QAS or L-serine as HBD formed liquids at room temperature.

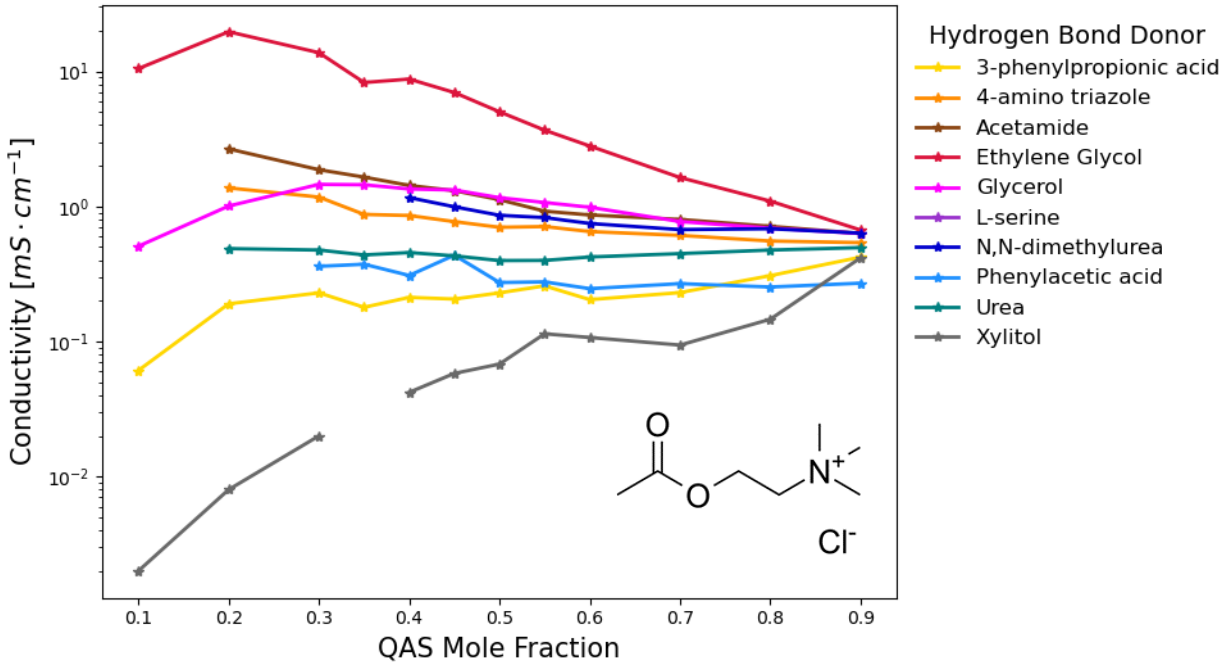

Figure 5.15. Conductivity of AcChCl based DES. AcChCl DES showed the greatest number of distinct DES to compare against. The break in the conductivity curve for Xylitol at 0.25 mole % AcChCl is a result of that sample not being liquid at room temperature.

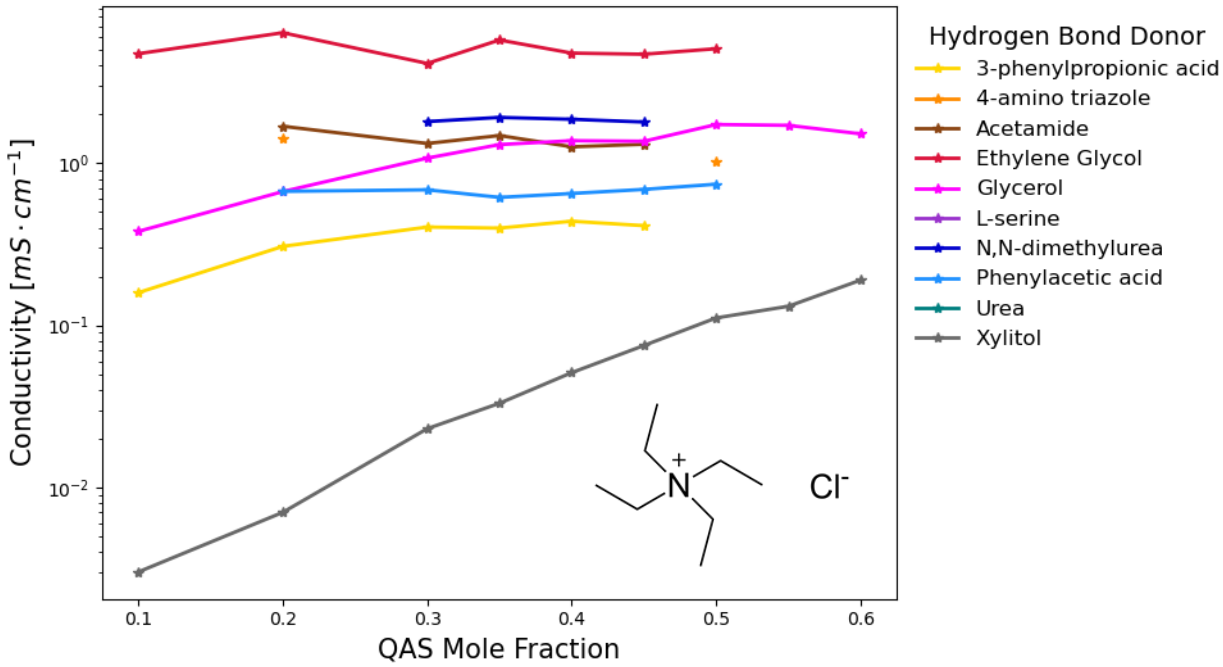

Figure 5.16. Conductivity of TEAC based DES.

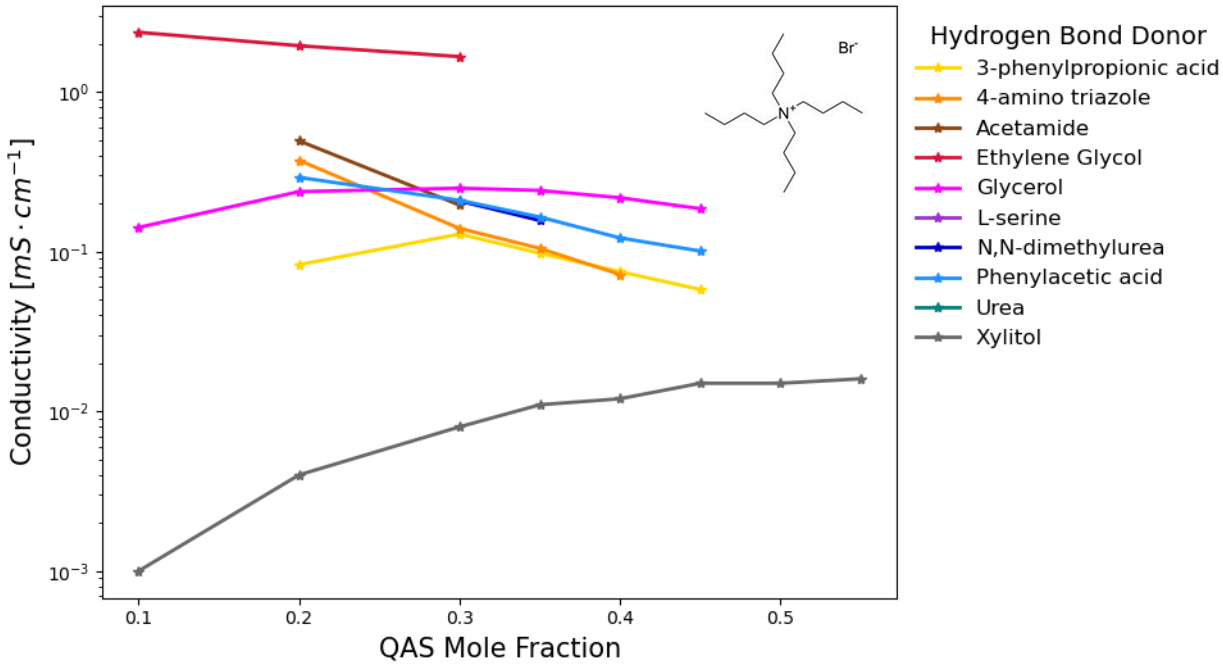

Figure 5.17. Conductivity of TPAB based DES. TPAB DES generally observed the lowest conductivities and fewest samples that remained liquid at room temperature.

Figures 5.15, 5.16, and 5.17 show comparisons of AcChCl, TEAC, and TPAB based DES, respectively. Immediately some interesting trends can be noticed from the results of this high-throughput electrochemical experiment. It is abundantly clear that variations in the molar composition in the DES with respect to the QAS and HBD components greatly affects the conductivity, which is a result of changes in viscosity as a result of variations in the molar composition.[20] All DES samples based on EG as HBD showed the highest conductivities, with the sample at 20 mol % AcChCl having the highest conductivity in the entire dataset at approximately 11 mS/cm. Conductivities for EG based DES with TEAC and TPAB were still respectable with maximum conductivities of approximately 5 mS/cm and 1 mS/cm. These conductivities compare well against conductivities reported for other EG based DES, particularly those with choline chloride.[72] Typically DES based on EG are known for possessing relatively high conductivities as the viscosity of EG is very low. On an opposite note, DES based on xylitol possessed the lowest conductivities in the dataset. DES with sugar based HBD, such as xylitol, are known to possess high viscosities, so it is intuitive that the conductivities for these DES would be quite poor, especially for the Xylitol based DES with 10 mol % TPAB which only exhibits a conductivity of approximately 0.001 mS/cm. Comparing the evolution of the conductivity between the EG and xylitol DES, important distinctions can be made. It is seen with all DES containing xylitol that the conductivity begins to substantially increase as the mole fraction of QAS is increased. This is also intuitive as generally one would hypothesize that greater number of ions available would increase conductivity, and it has been proposed previously that this is true for DES.[72] However, the data collected here suggests that that is certainly not true for all DES. Most notably, it can be seen for AcChCl based DES with EG and GL that the conductivity decreases significantly with increasing QAS concentration. This could suggest that the increased QAS concentrations are resulting in

increased viscosities for these DES, which would adversely affect the conductivity. Interestingly, when looking at EG and GL base DES with TEAC, the conductivities either remain relatively constant or increase slightly, and changing the QAS to TPAB causes the conductivities to behave more similarly as they did with AcChCl. Moreover, other studies have noted that conductivity of DES may evolve through a maximum.[73] This is noted particularly with EG and GL based DES, but is also seen in others such as the DES with AcChCl and PAA, which exhibits a sharp maximum conductivity at 45 mol % AcChCl. In general, aside from investigating the conductivities at either extreme, most DES other than those containing EG or xylitol fall within a range slightly above or below 1 mS/cm, which was mentioned earlier as a target metric for conductivities of DES. Overall, these initial results have shown good promise for rapidly and efficiently identifying high-conductivity DES, and further exploratory campaigns may yield further insight on new DES combinations.

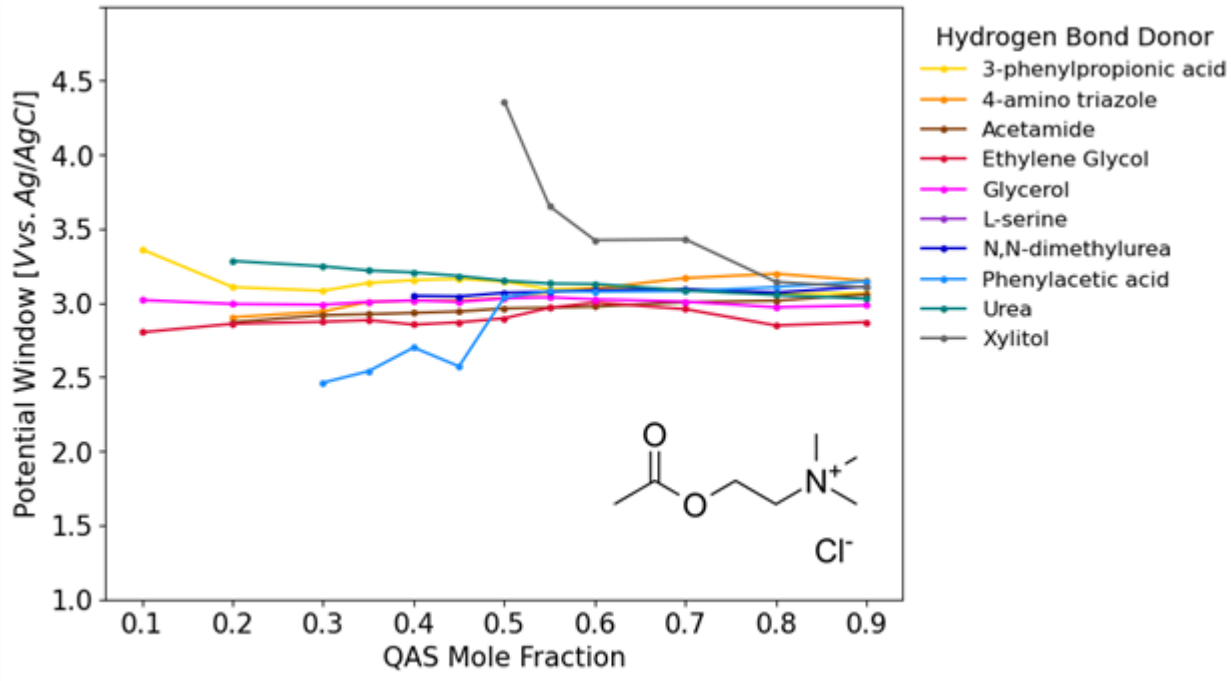

Figure 5.18. Electrochemical potential windows of AcChCl based DES.

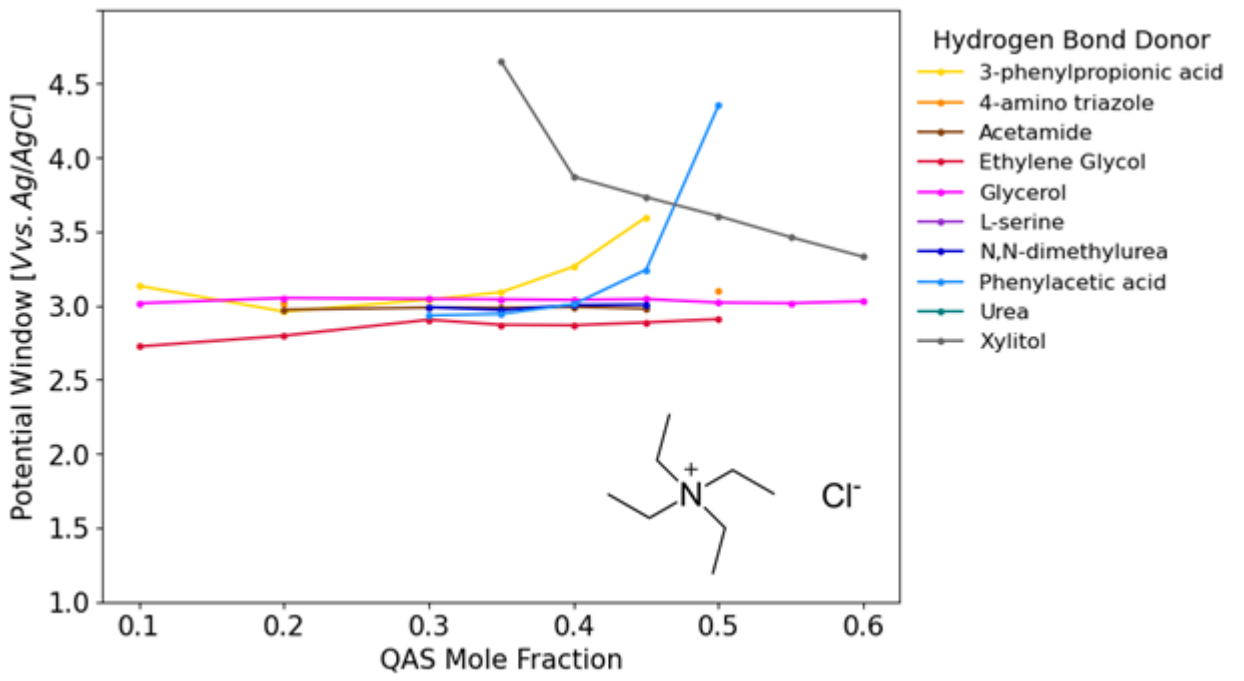

Figure 5.19. Electrochemical potential windows of TEAC based DES.

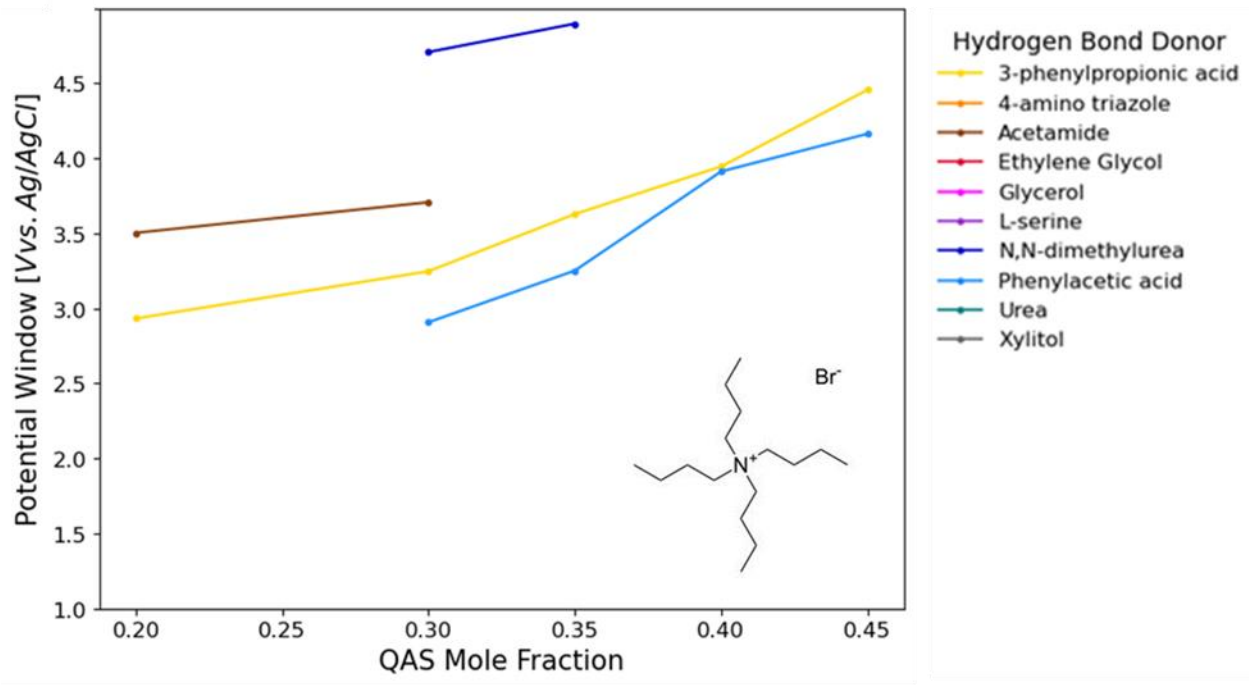

Figure 5.20. Electrochemical potential windows of TPAB based DES

Results of the high-throughput electrochemical measurements of the potential window of the various DES are shown in Figures 5.18, 5.19, and 5.20. Current industry leading systems for RFBs are typically based on aqueous electrolytes with limited operating voltage windows of approximately 1.23 V.[74] The DES electrolytes tested here possess windows at least twice as high as standard aqueous electrolytes, mostly falling in ranges between approximately 2.5 V to 4.5 V. These values are comparable to those reported in the literature for other DES systems, mostly based on choline chloride.[75] While further electrochemical studies with larger diversity of species such as those presented here are scarce, variations in the values of the potential windows for the same species in multiple studies can be noted.[52] It is known that the surface activity of the electrode is affected by the choice of material, which could explain the variability of potential windows in the literature. For example, Li et al. reported variability in the potential window of various ILs on gold, platinum, and GC working electrodes, noting that the GC electrode generally noted the largest potential windows.[75] Similar trends are noticed in DES by Bahadori et al., where the potential windows of 1:1 ChCl:Oxalic acid and 1:1 ChCl:Malonic acid were measured. The potential windows on GC electrodes for both DES were 2.64 V and 2.1 V, respectively, whereas on a platinum electrode they were 1.62 V and 1.43 V, respectively.[76] The values reported in this work using carbon-based SPEs are expected to be representative of those in full-scale RFB systems, which also use simple, carbon-based electrodes.

It can also be noticed that for most DES, the value of the potential window does not vary as drastically as the QAS concentration increases. This would make sense as the value of the potential window is correlated to the electrochemical degradation of the QAS and HBD that make up the DES, and so the relative concentration of these components would have less of an effect. However, we do see more variability with xylitol and PAA based DES. When paired with AcChCl,

the xylitol DES starts off at a relatively high potential window just under 4.5 V at 50 mol % AcChCl, then drops to 3 V at 80 mol % AcChCl. For PAA, the trend is the opposite where it increases significantly at 50 mol % AcChCl and then levels off. These trends are similar when they are paired with TEAC. It is important to note that some samples that were present in the conductivity measurements were not present in the potential window investigation, as certain samples (particularly those with xylitol) were so viscous that the potential required to meet the current at each galvanostatic step was outside the usable range of the Gamry for CP, which was 12V. Though only a limited number of samples were measured with TPAB, the potential windows of those samples were extremely attractive, almost all above 3 V. Substantial data on DES potential windows at various QAS and HBD combinations and compositions is extremely scarce in the literature, and this high-throughput investigation will yield valuable insight to the electrochemical community for applications beyond just electrolytes for RFB.

Looking at the CV for some of these DES combinations, interesting trends can be noted. Ideally when analyzing CV of electrolytes without active material, it is desired to see the current maintain as close to zero as possible during the measurement, without any significant peaks or features arising from side reactions. For many of the CVs shown, currents are below 1 mA. Below in figures 5.21 and 5.22 the CVs of PPA and PAA based DES with AcChCl, TEAC, and TPAB as the QAS are seen. All CVs were scanned at 100mV/s from -2 V to 2V vs. Ag/AgCl. The structures of PPA and PAA are extremely similar, both containing a carboxylic acid group. Comparing the CVs, strikingly similar features are seen. For the PPA and PAA paired with AcChCl, peaks at approximately 0.5 V are present, with the peaks for PPA increasing in magnitude with increasing QAS concentration.

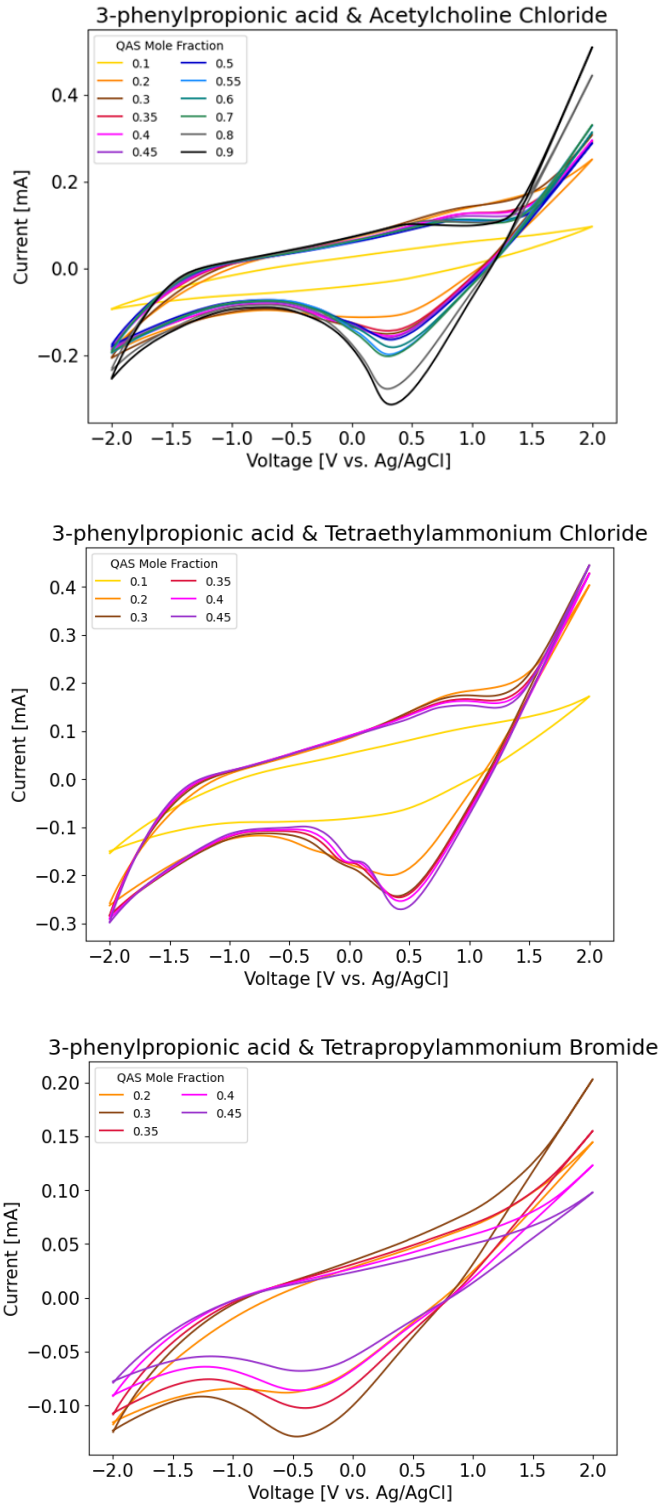

Figure 5.21. CV of 3-phenylpropionic acid (PPA) with various QAS. Top: AcChCl. Middle: TEAC. Bottom: TPAB.

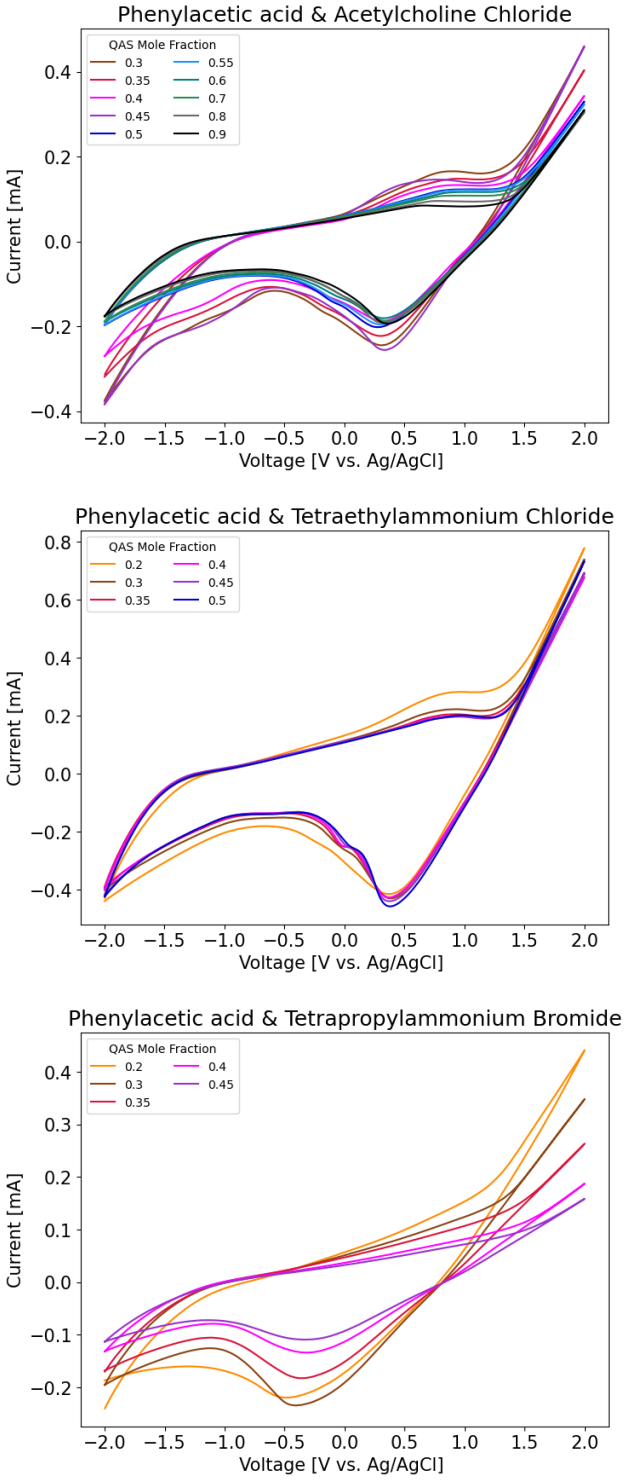

Figure 5.22. CV of phenylacetic acid (PAA) and various QAS. Top: AcChCl. Middle: TEAC. Bottom: TPAB.

The CVs with TEAC as the QAS are almost even more strikingly similar, with again the peaks increasing in magnitude with increased QAS concentration for PPA. Finally, when TPAB is used as the QAS, we again see a similar peak for both PPA and PAA but it is shifted by almost 1 V down to approximately -0.5 V. By varying the QAS, we see that the features that result in the CV can be heavily tied to the structure of the HBD, with both being primarily carboxylic acids. Looking at comparisons with other families of HBD, amide-based DES such as urea and acetamide with AcChCl both exhibit peaks occurring at more substantially negative potentials, near -1.5 V, yet the acetamide DES shows a much flatter curve in between the extreme potential regions, as seen in Figure 5.23. Alcohol/polyol-based DES such as EG and GL in Figure 5.24 show peaks occurring at 0.5 V, and even the slightest of peaks occurring at -1.25 V in the positive scan can be seen which is remarkable. It seems varying the halide of the QAS has an effect on shifting peak positions present, but it is noted for other studies involving ChCl based DES that the positive limits seen during CV is a result of the oxidation of Cl^- ions. [48,71] The limiting potentials in this case are attributed to decomposition with regards to the specific halide and structure of the QAS, where negative limiting potentials may be more closely influenced again by the nature of the HBD. Once again, CVs of DES with substantial variation in the choice of QAS and HBD is scarce, and this work is valuable to gain further insight other than high-throughput screening, specifically into mechanisms and reactions in DES for electrochemical applications.

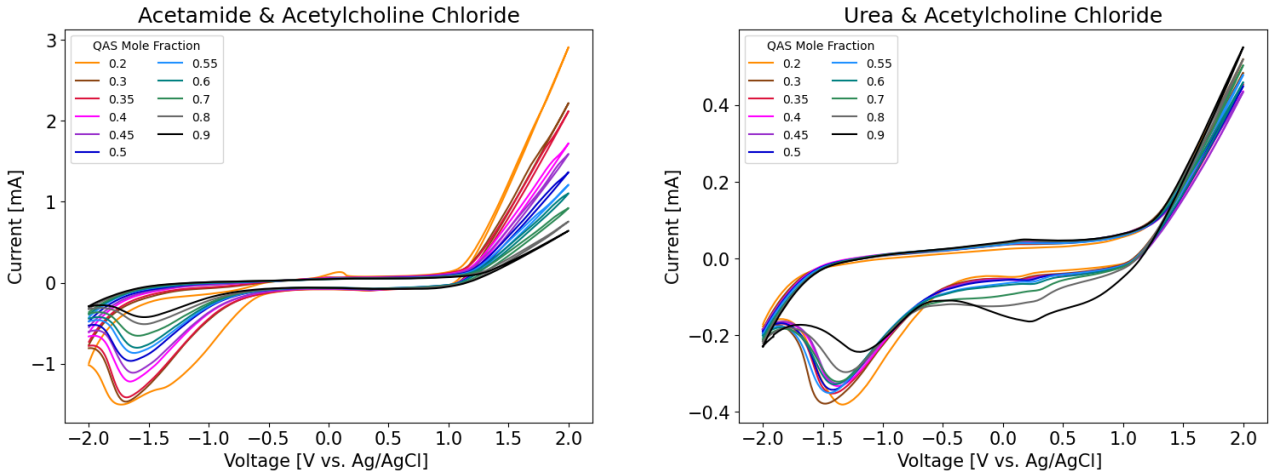

Figure 5.23. CV of amide HBD with AcChCl. Left: Acetamide. Right: Urea.

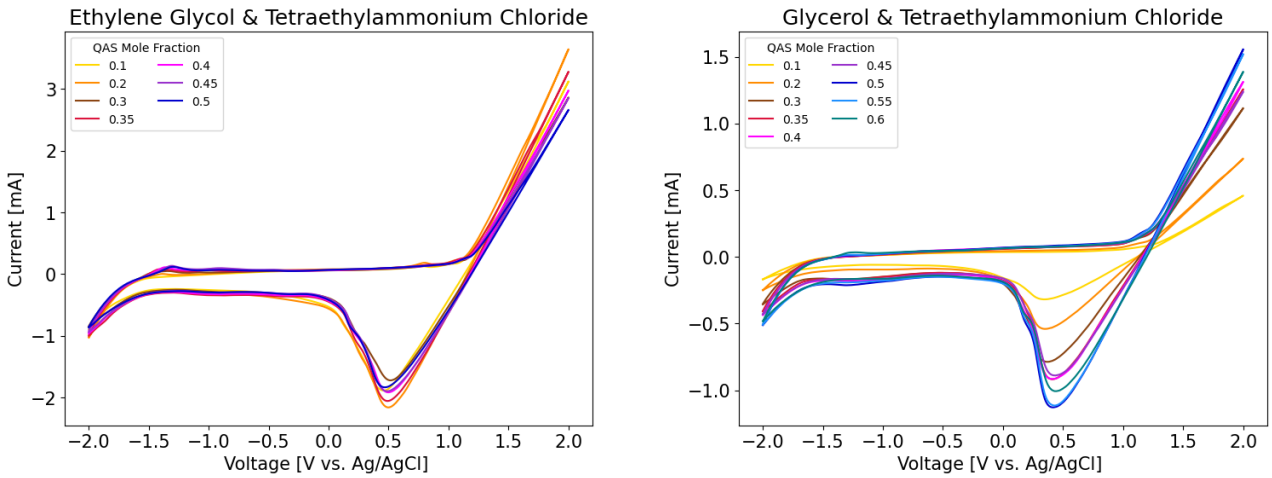

Figure 5.24. CV of polyol HBD with TEAC. Left: Ethylene Glycol. Right: Glycerol

5.4.3 *High-Throughput Melting Point Determination*

The thermal phase behavior of DES is arguably one of its most important properties and is frequently characterized via state of the art methods such as Differential Scanning Calorimetry (DSC).[28,77,78] DSC allows for accurate and precise determination of phase transitions, in which temperature differences are measured between the sample and a reference material that undergo identical thermal cycling.[79] Obviously melting points are of the utmost importance for characterizing DES, yet for samples that undergo glass transition phases this can be more difficult, but still suitable for detection using DSC. [80] Despite this, measurements at times can take upwards of an hour per sample when using DSC, which becomes time consuming and costly when investigating larger sample sets, or massive design spaces for DES which is the focus of this chapter. While additional instrumentation is available to increase throughput slightly, such as autosamplers, DSC is not conducive for high-throughput experimentation.

Recently, the concept of optically determining melting points and other thermal properties with an infrared (IR) camera has been proposed. The first to introduce this method was Kawakami in 2010, where an IR camera was used to observe the melting process of common active pharmaceutical ingredients on a programmable hot plate.[81] As the samples melted, an increase in their thermal conductivity resulted in a temporary spike in the temperature, from which the melting point could be estimated. The estimated melting points showed good agreement with melting points obtained through DSC. Because the technique used thermal imaging as a basis, it was proposed by the authors that it could be used to sample multiple materials at once. Similarly, Hou et al. also used this method to estimate melting points and other thermal properties for common materials using a dedicated aluminum pan with 16 wells for holding samples.[82] While these proof-of-concept systems have emphasized the high-throughput potentials for this unique method, the

demonstration of a fully integrated and open-source system that can be easily replicated by other users is still lacking. Moreover, the analysis also needs to be optimized for reliable automatic data interpretation so that the bottlenecks for sample analysis are not simply transferred from the measurement to the user that is interpreting the results. As such, an open source and high throughput thermal analysis system named PhasIR is described in this section that was developed with the goal of integrating into our high throughput DES characterization process to determine melting points and phase transitions for DES electrolytes.

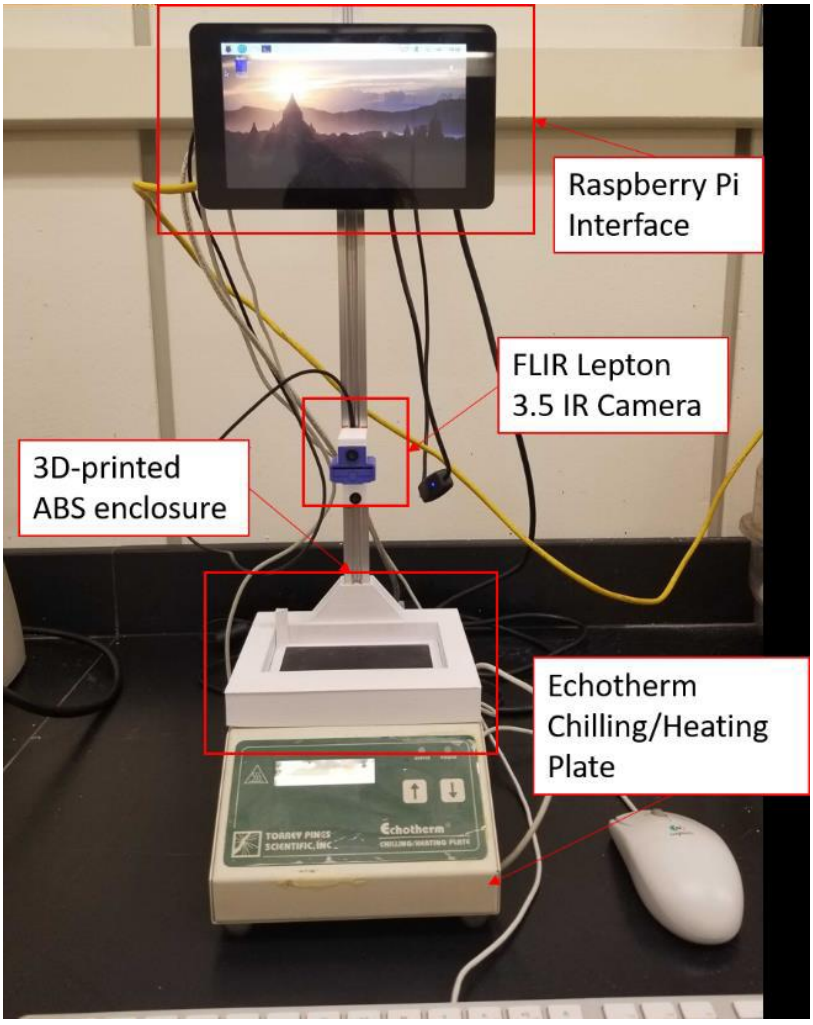

Figure 5.25. Image of PhasIR system and components.

Figure 5.25 shows the PhasIR system in addition to the hardware components. This high throughput system consists of a FLIR IR Lepton 3.5 IR camera that is placed at a fixed position above a Peltier plate to image a sample array. The Peltier plate, an Echotherm IC25, can be used with aluminum 96, 48 or 24 well-plate systems that are fabricated from black anodized aluminum to measure multiple samples at once in a parallel manner. The black coating on the plates is critical to maximize the emissivity and minimize the reflectivity of IR radiation. The aluminum multi-well plates are fabricated with conical-shaped wells, which was determined to be critical to maintaining sample positioning, after melting transitions, to facilitate automatic analysis with reduced error. The samples of interest are loaded onto the multi-well plates and heating on the Echotherm IC25 is initiated, as well as the IR camera feed on a Raspberry Pi interface to allow for simultaneous data collection for all samples, as seen in Figure 5.26. As the plate heats up, the temperature of the samples present in the camera field of view is measured and saved as a collection of frames in an *.HDF5* file format that is saved once the run is completed. The temperature of the multi-well plate during the measurement is used as the reference point while the sample temperature is obtained at the center-point of the conical wells. All of this is collected simultaneously using the IR camera that captures the full view of the plate. The data file that is produced by the camera is then analyzed with the open-source software package found on Github (https://github.com/pozzo-research-group/phasIR). The PhasIR system also provides a 3D-printed Acrylonitrile Butadiene Styrene (ABS) enclosure that allows for consistent placement of the well-plates below the IR camera and centered on top of the heating element. A consistent position of the plate allows for easier and more streamlined data collection.

Elaborating on the software portion, the package is designed to streamline the data exploration by allowing the user to extract and analyze the results directly from a Jupyter

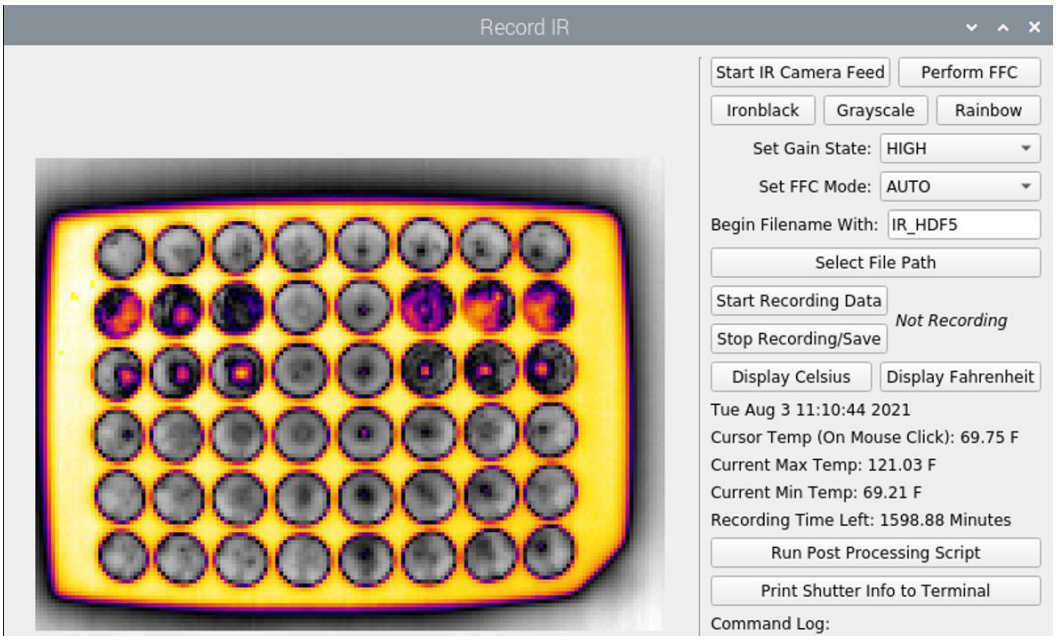

Figure 5.26. Screen capture of IR camera feed. The right panel allows the user to start data collection and later save into an .HDF5.

Notebook. The open-source package can be divided in two main sections: image analysis and thermal analysis. The image analysis module allows for the initial analysis of the frames that are collected by the IR camera. The image can be cropped and resized to remove any objects in the field of view that are neither samples nor part of the well-plate (e.g. insulating plastic enclosures). Next, the position of the wells containing the samples can be obtained automatically or selected manually on a sample frame. The average sample temperature is obtained from the average pixel values across a circular region of variable diameter that is positioned around each well's centroid across all frames of the video. For each well identified on the image, the plate temperature is identified as four equidistant points placed diagonally with respect to the well centroid. The thermal analysis module allows for the measurement of the temperature profile for each well and to analyze the curve, plotted relative to the plate temperature, to identify the phase transition temperature of each sample. The temperature is encoded in the pixel value composing the frames

collected by the IR camera. The final plate temperature is obtained as the average temperature of the four reference points for each well. Finally, the phase transition point is then obtained by identifying the onset of the peak that is formed by the curve that is obtained when subtracting the plate temperature from each sample temperature. Finally, the data that is extracted from each experimental run can be saved and stored in a new HDF5 file for subsequent sample characterization. Figure 5.27 shows screen captures from the image analysis and thermal analysis on a sample consisting of dodecanoic acid. The estimated melting point of the dodecanoic acid sample was 47.5°C, which agrees well with the range listed by the manufacturer Sigma-Aldrich at 44-66°C.

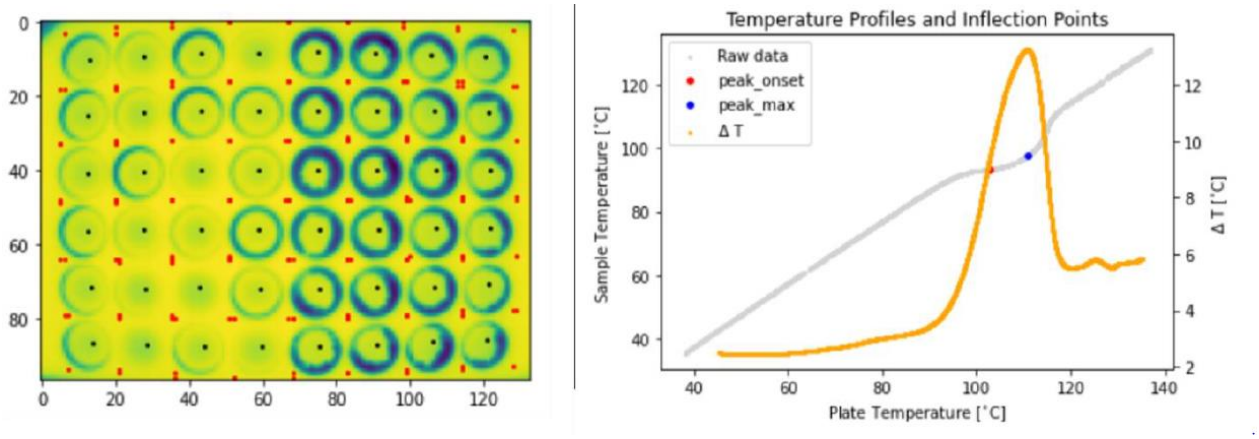

Figure 5.27. Screen captures of Image and thermal analysis on dodecanoic acid samples. Left: Plate locations (red markers) and well centroids (black markers). Right: Onset peak identification from temperature profile.

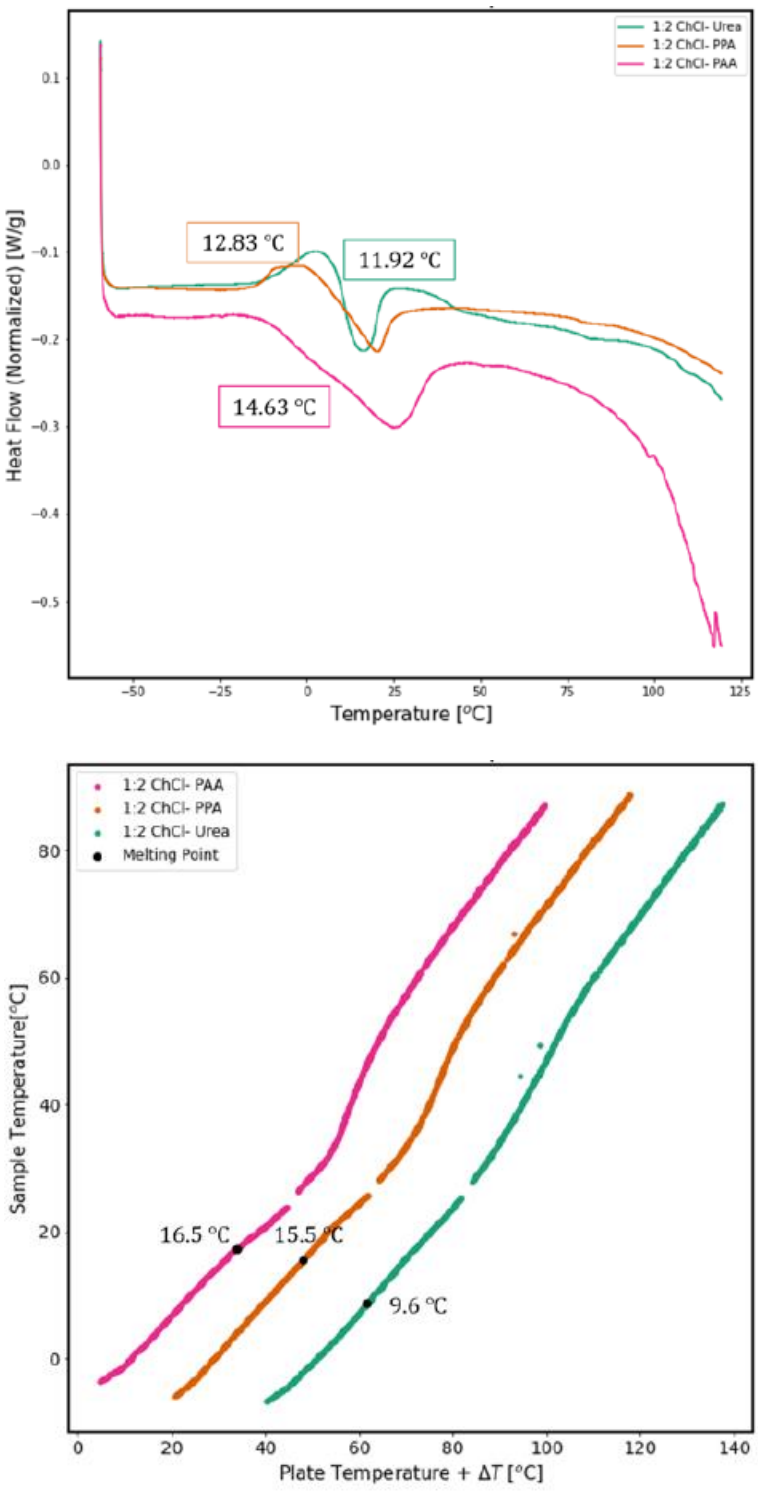

Figure 5.28. Melting point determination of three ChCl based DES. Top: DSC results. Bottom: PhasIR results.

It was desired to estimate the melting points of three common ChCl based DES as validation for the application of the system towards our high throughput DES characterization. The three DES consisted of 1:2 molar ratios of ChCl with urea, PPA, and PAA, whose melting points from the literature are 12°C, 20°C, and 25°C, respectively. [20,83] The DES were prepared in the traditional method by mixing each of the components at the appropriate molar ratios and heating in a vial until the mixture resulted in a uniform liquid. Samples were loaded onto the plate while hot and allowed to cool in an airtight desiccator. Once cooled, the samples were placed in a freezer at 0°C in an airtight bag containing desiccant to avoid moisture uptake. This freezing step was also done to ensure that the PPA and PAA samples were solid, as their melting points are just slightly below or at room temperature. This is a strategy that can be applied to other DES mixtures that may have melting points below room temperature. The results of the PhasIR system, are shown in Figure 5.28 and are compared with measurements obtained from a TA Discovery DSC 2500, with temperatures swept from -50°C to 120°C. Overall the results with the PhasIR system are quite comparable not only to the literature, but also to DSC. With the PhasIR system, the estimated melting points were 9.6°C, 15.5°C, and 16.5°C, for the urea, PPA, and PAA DES, respectively. Using the state-of-the-art DSC, the melting points were 11.9°C, 12.8°C, and 14.6°C, respectively. It is noted that the estimated melting points for the PPA and PAA DES were slightly lower than the literature value yet were comparable using both experimental systems. Considering the cost of the entire components in the PhasIR system being just $1,080, the results are quite remarkable. The modularity of this system should also be noted. Much of the hardware was already present in the laboratory when integrated into this high throughput melting point setup. The possibilities are not limited to only the components described here, as virtually any heating plate, IR camera, or wellplate design that fits within the frame of view can be utilized and accompanied by the software.

The PhasIR system has been demonstrated to be suitable for this high throughput investigation of DES and will be implemented much more heavily in the future. However, there is significant benefit the greater community with this system and it should not be limited to only the investigation of DES, as thermal analysis is a crucial aspect to materials characterization in industries and research areas such as pharmaceuticals and food sciences to name a few. Indeed, the open source nature of the system should also lead to others implementing this for a wide variety of applications that will increase the throughput of materials analysis and discovery overall.

5.5 Conclusions and Future Work

This chapter has offered an interesting perspective into the use of DES as electrolytes for RFBs, which is a new and exciting area of research for alternative solvents overall. DES were demonstrated to be extremely attractive for integration into RFBs due to their cost effectiveness, environmental friendliness and sustainability, and potential for increased performance aspects. The wider electrochemical potential windows yields possibilities for developing RFBs with higher cell potentials, when compared to conventional aqueous solvents, while still maintaining adequate ionic conductivities. Moreover, the increased solubility of many ROMs into DES is attractive for increasing the energy density of organic RFBs, which is a substantial challenge for this technology. Despite these benefits, the obstacles associated with identifying ideal DES for this system was made clear due to the massive design space associated with the materials. The high throughput and data driven strategies presented here provide an avenue for which to tackle this challenge, and work towards the development of ideal DES electrolytes for RFB.

It was demonstrated that use of cheminformatics proved effective in terms of outlining an initial design space for these materials to be investigated in a high throughput manner. After

proceeding through the high throughput experimentation, it is evident that the use of more advanced data science methods is necessary to effectively close the loop on this process. The ability to collect the amount of electrochemical and physiochemical data on DES systems has not been presented in the literature, and data in general is still quite scarce for DES. The methods outlined here will quickly increase the quantity of data available, and continued experimentation alone will not be sufficient to determine which features will lead to more favorable DES electrolytes. Thus, the use of statistical methods such as quantitative structure property relationships (QSPR) to predict DES properties from structural features will become extremely attractive. QSPR studies have already been applied to ILs and DES, although much more sparingly for DES. [84–87] Significant more data is available for ILs however, leading to a lack of generalized models for DES able to predict properties across various structures and functional groups. Continuing to implement the high throughput experimentation described in this chapter will aim to increase the quantity and diversity of data available to perform QSPR studies. In addition, as data is accumulated, it is important for discussions of centralized databases for DES to engage the broader community. Early discussions on avenues for this goal have been proposed recently by Xu et al. for extracting DES data scattered in the literature and integrating into machine-readable formats for open-source use. [88]

Additions towards the high-throughput experimentation platform are also an area to explore for future work. Currently, the system is only capable of performing electrochemical measurements on samples at room temperature. While this does effectively screen against candidates that most likely have much higher melting points, valuable insight into the electrochemical behavior of DES at across various temperatures is necessary, as RFBS are often operated at elevated temperatures in industry. This also may in turn lead to the usage of DES that

while not liquid at room temperature, behave favorably at elevated temperatures and opens further possibilities for tailored design of DES electrolytes. One of the most notable properties not mentioned in this high throughput system is viscosity. While in this case, information on the viscosity of samples can be inferred from the relationship to the conductivity, it is still a property that should be strived to measure in high throughput as well. While certain high-throughput viscometry systems have recently been developed, these have very high costs and are outside of reach for much of the broader community. However, examples of alternative and lower cost methods to measure viscosities such as that proposed by Deshmukh et al. show exciting promise, where their high-throughput system relied on the transient flow of fluids through a pipette.[89] Incorporating novel systems such as this into an automated, motorized platform would be ideal for combinatorial investigation of DES viscosities.

Lastly, while preliminary studies on the reversibility and solubilities of ROM in DES were presented at the beginning of the chapter, a much more extensive investigation is required, and now possible. Ideally, a small number of well-known ROMs could be initially incorporated to form ternary DES. The possibility of using ROMs that are somewhat soluble in water, ethanol, methanol, etc. would enable expansion of the current synthesis protocol to add in the ROM using the OT-2, varying the concentration of the active material. As shown earlier in the chapter, the addition of significant amounts of ROM into well-known DES may cause a shift in melting points. It is indeed likely that properties observed with binary DES may change drastically once they are converted to ternary systems. This does however pose an interesting opportunity to use DOE strategies to investigate the ternary space in efficient manners, which is a strategy frequently employed for mixture problems such as this. The work presented in this chapter will strive to

influence a new direction for how materials for RFBs are investigated moving forward and accelerate the advancement of this promising energy storage technology.

5.6 REFERENCES

1. Singh, V., Kim, S., Kang, J. & Byon, H. R. Aqueous organic redox flow batteries. *Nano Res.* (2019). doi:10.1007/s12274-019-2355-2
2. Wei, X., Nie, Z., Wang, W., Liu, T. & Sprenkle, V. A Total Organic Aqueous Redox Flow Battery Employing a Low Cost and Sustainable Methyl Viologen Anolyte and 4-HO-TEMPO Catholyte. *Adv. Energy Mater.* **6**, 1501449 (2015).
3. Wei, X. *et al.* Materials and Systems for Organic Redox Flow Batteries: Status and Challenges. *ACS Energy Lett.* **2**, 2187–2204 (2017).
4. Chen, H., Cong, G. & Lu, Y. C. Recent progress in organic redox flow batteries: Active materials, electrolytes and membranes. *J. Energy Chem.* (2018). doi:10.1016/j.jechem.2018.02.009
5. Winsberg, J., Hagemann, T., Janoschka, T., Hager, M. D. & Schubert, U. S. Redox-Flow Batteries: From Metals to Organic Redox-Active Materials. *Angewandte Chemie - International Edition* (2017). doi:10.1002/anie.201604925
6. Shah, A. A. *et al.* Recent developments in organic redox flow batteries: A critical review. *J. Power Sources* **360**, 243–283 (2017).
7. Gong, K., Fang, Q., Gu, S., Li, S. F. Y. & Yan, Y. Nonaqueous redox-flow batteries: Organic solvents, supporting electrolytes, and redox pairs. *Energy Environ. Sci.* **8**, 3515–3530 (2015).
8. Hu, B. & Liu, T. L. Two electron utilization of methyl viologen anolyte in nonaqueous

organic redox flow battery. *J. Energy Chem.* **27**, 1326–1332 (2018).

9. Zhang, Q., De Oliveira Vigier, K., Royer, S. & Jérôme, F. Deep eutectic solvents: Syntheses, properties and applications. *Chem. Soc. Rev.* **41**, 7108–7146 (2012).
10. Ghandi, K. A Review of Ionic Liquids, Their Limits and Applications. *Green Sustain. Chem.* **04**, 44–53 (2014).
11. Lei, Z. Introduction: Ionic Liquids. *Chem. Rev.* **117**, (2017).
12. Welton, T. Ionic liquids: a brief history. doi:10.1007/s12551-018-0419-2
13. Toledo Hijo, A. A. C., Maximo, G. J., Costa, M. C., Batista, E. A. C. & Meirelles, A. J. A. Applications of Ionic Liquids in the Food and Bioproducts Industries. *ACS Sustainable Chemistry and Engineering* **4**, 5347–5369 (2016).
14. Deetlefs, M. & Seddon, K. R. Assessing the greenness of some typical laboratory ionic liquid preparations. *Green Chem.* **12**, 17–30 (2010).
15. García, G., Aparicio, S., Ullah, R. & Atilhan, M. Deep eutectic solvents: Physicochemical properties and gas separation applications. *Energy and Fuels* **29**, 2616–2644 (2015).
16. Smith, E. L., Abbott, A. P. & Ryder, K. S. Deep Eutectic Solvents (DESs) and Their Applications. *Chem. Rev.* **114**, 11060–11082 (2014).
17. Abbott, A. P., Capper, G., Davies, D. L., Rasheed, R. K. & Tambyrajah, V. Novel solvent properties of choline chloride/urea mixtures. *Chem. Commun.* **9**, 70–71 (2003).
18. Ho, K. C. *et al.* Removal of glycerol from palm oil-based biodiesel using new ionic liquids analogues. *J. Eng. Sci. Technol.* **10**, 98–111 (2014).
19. Hayyan, M., Mjalli, F. S., Hashim, M. A. & AlNashef, I. M. A novel technique for separating glycerine from palm oil-based biodiesel using ionic liquids. *Fuel Process. Technol.* **91**, 116–120 (2010).

20. Abbott, A. P., Boothby, D., Capper, G., Davies, D. L. & Rasheed, R. K. Deep Eutectic Solvents formed between choline chloride and carboxylic acids: Versatile alternatives to ionic liquids. *J. Am. Chem. Soc.* **126**, 9142–9147 (2004).

21. Hou, Y. *et al.* Novel binary eutectic mixtures based on imidazole. *J. Mol. Liq.* **143**, 154–159 (2008).

22. Carriazo, D., Gutiérrez, M. C., Ferrer, M. L. & Del Monte, F. Resorcinol-based deep eutectic solvents as both carbonaceous precursors and templating agents in the synthesis of hierarchical porous carbon monoliths. *Chem. Mater.* **22**, 6146–6152 (2010).

23. Martins, M. A. R., Pinho, S. P. & Coutinho, J. A. P. Insights into the Nature of Eutectic and Deep Eutectic Mixtures. *J. Solution Chem.* (2018). doi:10.1007/s10953-018-0793-1

24. Millia, L. *et al.* Bio-inspired choline chloride-based deep eutectic solvents as electrolytes for lithium-ion batteries. *Solid State Ionics* **323**, 44–48 (2018).

25. Boisset, A., Menne, S., Jacquemin, J., Balducci, A. & Anouti, M. M. Deep eutectic solvents based on N-methylacetamide and a lithium salt as suitable electrolytes for lithium-ion batteries. *Phys. Chem. Chem. Phys* **15**, (2013).

26. Altamash, T. *et al.* Insights into choline chloride-phenylacetic acid deep eutectic solvent for CO2 absorption. *RSC Adv.* **6**, 109201–109210 (2016).

27. Söldner, A., Zach, J. & König, B. Deep eutectic solvents as extraction media for metal salts and oxides exemplarily shown for phosphates from incinerated sewage sludge ash. *Green Chem.* **21**, 321–328 (2019).

28. Morrison, H. G., Sun, C. C. & Neervannan, S. Characterization of thermal behavior of deep eutectic solvents and their potential as drug solubilization vehicles. *Int. J. Pharm.* **378**, 136–139 (2009).

29. Xu, Q. *et al.* A deep eutectic solvent (DES) electrolyte-based vanadium-iron redox flow battery enabling higher specific capacity and improved thermal stability. *Electrochim. Acta* **293**, 426–431 (2019).

30. Zhang, C. *et al.* A Sustainable Redox-Flow Battery with an Aluminum-Based, Deep-Eutectic-Solvent Anolyte. *Angew. Chemie - Int. Ed.* **56**, 7454–7459 (2017).

31. Wang, Y. *et al.* Zn-based eutectic mixture as anolyte for hybrid redox flow batteries. *Sci. Rep.* **8**, (2018).

32. Goeltz, J. C. & Matsushima, L. N. Metal-free redox active deep eutectic solvents. *Chem. Commun.* **53**, 9983–9985 (2017).

33. Sinclair, N. S., Poe, D., Savinell, R. F., Maginn, E. J. & Wainright, J. S. A Nitroxide Containing Organic Molecule in a Deep Eutectic Solvent for Flow Battery Applications. *J. Electrochem. Soc.* **168**, 020527 (2021).

34. Holbrey, J. D ; Seddon, K. R. Ionic Liquids. *Clean Technol. Environ. Policy* **1**, 223–236 (1999).

35. Kaul, M. J., Qadah, D., Mandella, V. & Dietz, M. L. Systematic evaluation of hydrophobic deep-melting eutectics as alternative solvents for the extraction of organic solutes from aqueous solution. *RSC Adv.* **9**, 15798–15804 (2019).

36. Haghbakhsh, R., Parvaneh, K., Raeissi, S. & Shariati, A. A general viscosity model for deep eutectic solvents: The free volume theory coupled with association equations of state. *Fluid Phase Equilib.* **470**, 193–202 (2018).

37. Lloret, J. O., Vega, L. F. & Llovell, F. Accurate description of thermophysical properties of Tetraalkylammonium Chloride Deep Eutectic Solvents with the soft-SAFT equation of state. *Fluid Phase Equilib.* **448**, 81–93 (2017).

38. González De Castilla, A., Bittner, J. P., Müller, S., Jakobtorweihen, S. & Smirnova, I. Thermodynamic and Transport Properties Modeling of Deep Eutectic Solvents: A Review on gE-Models, Equations of State, and Molecular Dynamics. *J. Chem. Eng. Data* **65**, 943–967 (2020).

39. Dean, W., Klein, J. & Gurkan, B. Do Deep Eutectic Solvents Behave Like Ionic Liquid Electrolytes? A Perspective from the Electrode-Electrolyte Interface. *J. Electrochem. Soc.* **168**, 026503 (2021).

40. Matsuda, S., Nishioka, K. & Nakanishi, S. High-throughput combinatorial screening of multi-component electrolyte additives to improve the performance of Li metal secondary batteries. *Sci. Rep.* **9**, 1–3 (2019).

41. Cheng, L. *et al.* Accelerating Electrolyte Discovery for Energy Storage with High-Throughput Screening. *Journal of Physical Chemistry Letters* **6**, 283–291 (2015).

42. Sun, S. *et al.* Accelerated Development of Perovskite-Inspired Materials via High-Throughput Synthesis and Machine-Learning Diagnosis. *Joule* **3**, 1437–1451 (2019).

43. Whitacre, J. F. *et al.* An Autonomous Electrochemical Test Stand for Machine Learning Informed Electrolyte Optimization. *J. Electrochem. Soc.* **166**, A4181–A4187 (2019).

44. Bru, M. *et al.* Cross-linked poly(2-hydroxyethylmethacrylate) films doped with 1,2-diaminoanthraquinone (DAQ) as efficient materials for the colorimetric sensing of nitric oxide and nitrite anion. *Tetrahedron Lett.* **47**, 1787–1791 (2006).

45. Enoch, I. V. M. V. & Swaminathan, M. Fluorimetric study on molecular recognition of β-cyclodextrin with 2-amino-9-fluorenone. *J. Fluoresc.* **16**, 501–510 (2006).

46. Ali, S., Hussain, T. & Nawaz, R. Optimization of alkaline extraction of natural dye from Henna leaves and its dyeing on cotton by exhaust method. *J. Clean. Prod.* **17**, 61–66 (2009).

47. Wei, X. *et al.* Radical Compatibility with Nonaqueous Electrolytes and Its Impact on an All-Organic Redox Flow Battery. *Angew. Chemie - Int. Ed.* **54**, 8684–8687 (2015).

48. Haerens, K., Matthijs, E., Binnemans, K. & Van Der Bruggen, B. Electrochemical decomposition of choline chloride based ionic liquid analogues. *Green Chem.* **11**, 1357–1365 (2009).

49. Murray, P. M. & Forfar, L. C. The Application of Advanced Design of Experiments for the Efficient Development of Chemical Processes. *Chem. Informatics* **03**, (2017).

50. Cao, B. *et al.* How to optimize materials and devices via design of experiments and machine learning: Demonstration using organic photovoltaics. *ACS Nano* **12**, 7434–7444 (2018).

51. Kazakov, A. , Magee, J. , Chirico, R. , Diky, V. , Kroenlein, K. , Muzny, C. and Frenkel, M. Ionic Liquids Database - ILThermo (v2.0). *NIST* (2013).

52. Marcus, Y. *Deep Eutectic Solvents*. (Springer International Publishing, 2019). doi:10.1007/978-3-030-00608-2

53. Swain, M. PubChemPy. (2014).

54. Kim, S., Thiessen, P. A., Cheng, T., Yu, B. & Bolton, E. E. An update on PUG-REST: RESTful interface for programmatic access to PubChem. *Nucleic Acids Res.* **46**, W563–W570 (2018).

55. Kim, S. *et al.* Pug-View: Programmatic access to chemical annotations integrated in PubChem. *J. Cheminform.* **11**, 56 (2019).

56. Cereto-Massagué, A. *et al.* Molecular fingerprint similarity search in virtual screening. *Methods* **71**, 58–63 (2015).

57. National Institute of Health. PubChem Substructure Fingerprint. (2009).

58. Bajusz, D., Rácz, A. & Héberger, K. Why is Tanimoto index an appropriate choice for

fingerprint-based similarity calculations? *J. Cheminform.* **7**, 1–13 (2015).

59. Morgan, H. L. The Generation of a Unique Machine Description for Chemical Structures-A Technique Developed at Chemical Abstracts Service. *Am. Chem. Soc.* **5**, 107–113 (1965).

60. Firdaus Begam, B., Begam, B. F. & Kumar, J. S. Visualization of Chemical Space Using Principal Component Analysis. *World Appl. Sci. J.* **29**, 53–59 (2014).

61. Ivosev, G., Burton, L. & Bonner, R. Dimensionality reduction and visualization in principal component analysis. *Anal. Chem.* **80**, 4933–4944 (2008).

62. Verslycke, T. *et al.* The Chemistry Scoring Index (CSI): A hazard-based scoring and ranking tool for chemicals and products used in the oil and gas industry. *Sustain.* **6**, 3993–4009 (2014).

63. Dehghan-Manshadi, B., Mahmudi, H., Abedian, A. & Mahmudi, R. A novel method for materials selection in mechanical design: Combination of non-linear normalization and a modified digital logic method. *Mater. Des.* **28**, 8–15 (2007).

64. Spiwok, V. & Kříž, P. Time-Lagged t-Distributed Stochastic Neighbor Embedding (t-SNE) of Molecular Simulation Trajectories. *Front. Mol. Biosci.* **7**, 132 (2020).

65. Janssen, A. P. A. *et al.* Drug Discovery Maps, a Machine Learning Model That Visualizes and Predicts Kinome-Inhibitor Interaction Landscapes. *J. Chem. Inf. Model.* **59**, 1221–1229 (2019).

66. Maugeri, Z. & Domínguez De María, P. Novel choline-chloride-based deep-eutectic-solvents with renewable hydrogen bond donors: Levulinic acid and sugar-based polyols. *RSC Adv.* **2**, 421–425 (2012).

67. Shahbaz, K., Mjalli, F. S., Hashim, M. A. & Al Nashef, I. M. Using deep eutectic solvents for the removal of glycerol from palm oil-based biodiesel. *Journal of Applied Sciences* **10**,

3349–3354 (2010).

68. Abbott, A. P. *et al.* Glycerol eutectics as sustainable solvent systems. *Green Chem.* **13**, 82–90 (2011).

69. Abbott, A. P., Capper, G., Davies, D. L., Rasheed, R. K. & Tambyrajah, V. Novel solvent properties of choline chloride/urea mixtures. *Chem. Commun.* 70–71 (2003). doi:10.1039/b210714g

70. Dave, A. *et al.* Autonomous discovery of battery electrolytes with robotic experimentation and machine-learning. *arXiv* (2019). doi:10.1016/j.xcrp.2020.100264

71. Fuchs, D. *et al.* Electrochemical Behavior of Graphene in a Deep Eutectic Solvent. *ACS Appl. Mater. Interfaces* **12**, 40937–40948 (2020).

72. Abbott, A. P., Harris, R. C. & Ryder, K. S. Application of hole theory to define ionic liquids by their transport properties. *J. Phys. Chem. B* **111**, 4910–4913 (2007).

73. García, G., Aparicio, S., Ullah, R. & Atilhan, M. Deep eutectic solvents: Physicochemical properties and gas separation applications. *Energy and Fuels* **29**, 2616–2644 (2015).

74. Chalamala, B. R. *et al.* Redox flow batteries: An engineering perspective. *Proc. IEEE* **102**, 976–999 (2014).

75. Li, Q. *et al.* The electrochemical stability of ionic liquids and deep eutectic solvents. *Sci. China Chem.* **59**, 571–577 (2016).

76. Bahadori, L. *et al.* Physicochemical properties of ammonium-based deep eutectic solvents and their electrochemical evaluation using organometallic reference redox systems. *Electrochim. Acta* **113**, 205–211 (2013).

77. Hall, C. L. *et al.* Metastable crystalline phase formation in deep eutectic systems revealed by simultaneous synchrotron XRD and DSC. *Chem. Commun.* **56**, 10726–10729 (2020).

78. Jani, A., Sohier, T. & Morineau, D. Phase behavior of aqueous solutions of ethaline deep eutectic solvent. *J. Mol. Liq.* **304**, 112701 (2020).

79. Bhadeshia, H. K. D. H. Thermal Analyses Techniques. Differential Thermal Analysis. *Univ. Cambridge, Mater. Sci. Metall.* (2002). doi:10.1351/goldbook.d01709

80. Chemat, F., Anjum, H., Shariff, A. M., Kumar, P. & Murugesan, T. Thermal and physical properties of (Choline chloride + urea + l-arginine) deep eutectic solvents. *J. Mol. Liq.* **218**, 301–308 (2016).

81. Kawakami, K. Parallel Thermal Analysis Technology Using an Infrared Camera for High-Throughput Evaluation of Active Pharmaceutical Ingredients: A Case Study of Melting Point Determination. *AAPS PharmSciTech* **11**, 1202–1205 (2010).

82. Hou, S., Huo, R. & Su, M. High throughput integrated thermal characterization with non-contact optical calorimetry. *Rev. Sci. Instrum.* **88**, 104902 (2017).

83. Abbott, A. P., Capper, G. & Gray, S. Design of improved deep eutectic solvents using hole theory. *ChemPhysChem* **7**, 803–806 (2006).

84. Khajeh, A., Shakourian-Fard, M. & Parvaneh, K. Quantitative structure-property relationship for melting and freezing points of deep eutectic solvents. *J. Mol. Liq.* **321**, 114744 (2021).

85. Lemaoui, T. *et al.* Prediction of Electrical Conductivity of Deep Eutectic Solvents Using COSMO-RS Sigma Profiles as Molecular Descriptors: A Quantitative Structure-Property Relationship Study. *Ind. Eng. Chem. Res.* **59**, 13343–13354 (2020).

86. Paduszyński, K., Kłębowski, K. & Królikowska, M. Predicting melting point of ionic liquids using QSPR approach: Literature review and new models. *J. Mol. Liq.* **344**, 117631 (2021).

87. Sepehri, B. A review on created QSPR models for predicting ionic liquids properties and their reliability from chemometric point of view. *J. Mol. Liq.* **297**, 112013 (2020).

88. Xu, X., Range, J., Gygli, G. & Pleiss, J. Analysis of Thermophysical Properties of Deep Eutectic Solvents by Data Integration. *J. Chem. Eng. Data* (2019). doi:10.1021/acs.jced.9b00555

89. Deshmukh, S. *et al.* A Novel High-Throughput Viscometer. (2016). doi:10.1021/acscombsci.5b00176

APPENDIX

A1: NEUTRON ANALYSIS OF AQUEOUS ORGANIC REDOX-FLOW BATTERIES

1 Background and Motivation

As discussed previously, the use of redox-active organic materials (ROMs) in aqueous RFBs has gained widespread attention due to the numerous advantages over their metal ion counterparts. [1–3] At such a novel stage in development, organic RFBs still have several obstacles to overcome including increasing the energy density (solubility) stability of the ROMs. However, because of their synthetic tunability and modularity, the pathway for these obstacles to be overcome exists. One strategic method lies in obtaining knowledge pertaining to the structure of the ROM and how certain characteristics may lead to undesired performance in the cell. This ideology can also be extended to structure-performance relationships related to the membrane during cycling.

A ubiquitous characteristic in all ROMs that have been proposed for aqueous organic RFBs is the presence of a polar functional group to enable solubility in aqueous media. [4] It's possible that some of these ROMs may behave similarly to surfactants in that they have a tendency to form structures in solution such as micelles, due to the hydrophilic polar functional group and the remaining hydrophobic organic structure. [5] The dynamic environment in which these ROMs exist consist of frequent changes in pH and various molecular states of charge which could affect their structure and subsequently many of the properties that are crucial for performance in RFBs. Structure-performance relationships become even more important with various new aqueous RFBs based on redox-active polymers and redox-active colloids whose structure is the basis for their entire functionality as novel ROMs. [6–8] Similarly, the structure of the membrane can also

drastically vary during RFB cycling. Structure analysis is commonly performed for membranes *ex-situ* in the literature, where pH and hydration swelling can greatly affect the pore sizes and their interconnected network. [9–11] As expected, Nafion has been one of the most investigated membranes as it's suited for several applications, but it's structure and pore network is still relatively not fully understood. [12] This uncertainty increases when evaluating the membrane performance under actual, realistic operating conditions inside a RFB. Specifically, fouling from ROM degradation during cycling could occur affecting the transport properties which are crucial for performance.

Here, we present the unique opportunity to apply small-angle neutron scattering (SANS) to probe the structure of ROM assembly and the membrane. *Ex-situ* preliminary data obtained using SAXS on ROMs and Nafion membranes after charge-discharge cycling in a RFB shows noticeable changes compared to their pristine, unused state. This was followed by the design of a RFB SANS environment to probe structures *in-situ* during cycling. Preliminary data using this SANS environment indicated that modifications to the materials used in the environment construction are necessary to obtain reliable scattering data on the membrane. Follow up experiments to assess the quality of SANS data related to ROMs in our environment is necessary. SANS is a powerful technique and is well suited for this application due to the ability to probe structure in real-time environments, and this work has provided valuable insight towards adequately applying this methodology.

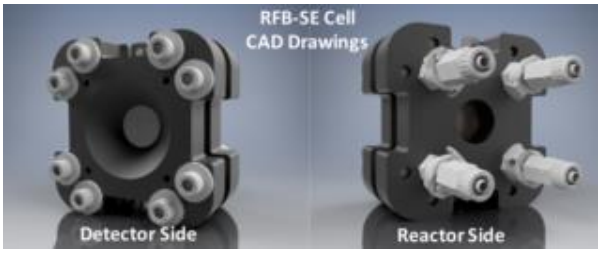

Figure A.1. Schematic of RFB-SE.

2 EXPERIMENTAL METHODS

Modifications were made to a commercially available lab-scale RFB enabled *in-situ* SANS analysis during operation. (Figure A.1)**.** Many components of this RFB SANS environment (RFB-SE) are very similar to others our lab has developed previously. The goal for the design of the RFB-SE was to allow for analysis of the membrane directly through the electrochemical cell as seen in Figure A.2. Analysis of the ROMs would ideally be done in adjacent flow cells

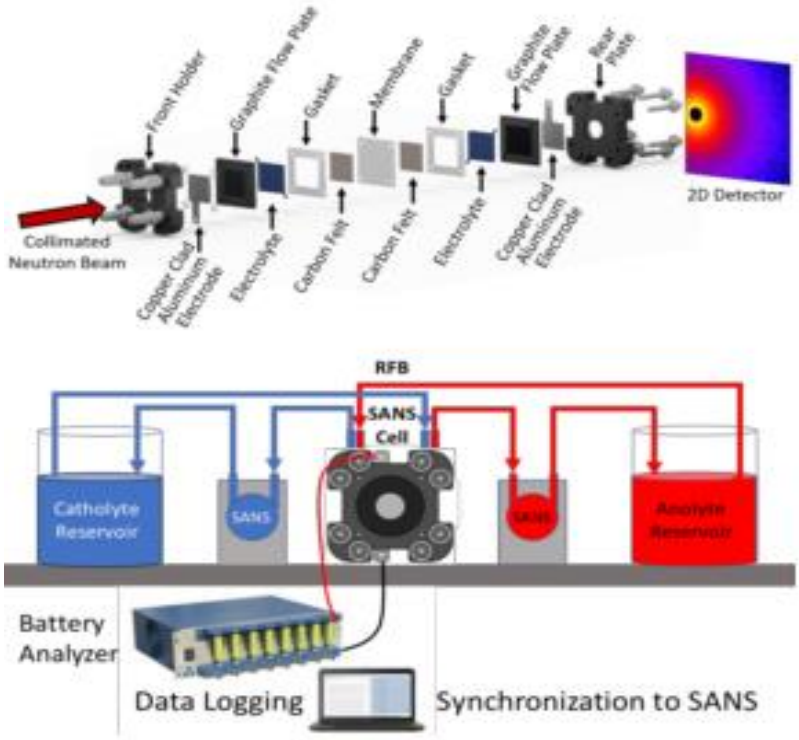

Figure A.2. Schematic illustration of the RFB-SE during operation.

Changes that are seen in the structure of the membrane would be correlated to performance metrics (Energy capacity, Coulombic, voltage, energy efficiencies) that are simultaneously collected using a battery analyzer.

3 RESULTS AND CONCLUSIONS

Preliminary SAXS data has been obtained for the membrane before and after 100 cycles in a RFB. **(**Figure A.3**).** There is a substantial change in low Q followed by changes in intensity at high Q values. SAXS of the ROM (F2CA) used in the RFB was also obtained. Figure A.4 shows SAXS profiles of uncharged F2CA in 1M KOH followed by SAXS profiles of F2CA that were extracted at different states of charge from the battery.

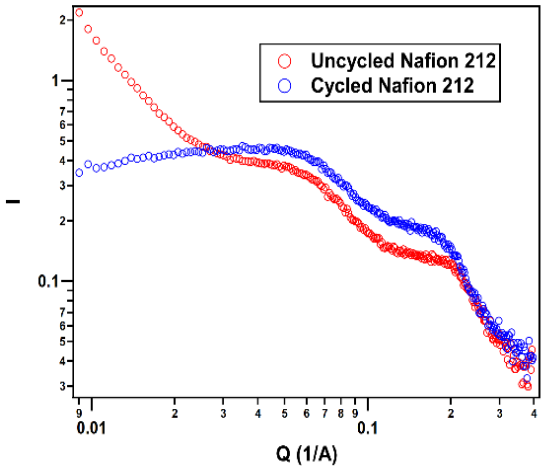

Figure A.3. SAXS of cycled and uncycled Nafion 212.

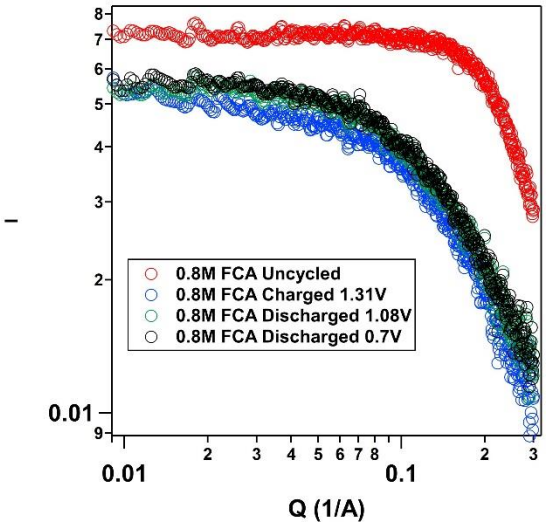

Figure A.4. SAXS of F2CA before cycling and at various states of charge.

While the profiles of the F2CA at different states of charge did not vary too much from each other, there is a substantial change compared to the uncycled F2CA sample with regards to the intensity at the low Q region.

Preliminary data was followed by experiments on the sample environment performed at the National Institute of Standards and Technology's (NIST) Center for High-Resolution Neutron Scattering (CHRNS). The instrument used was the NGB 30m SANS. Each of the individual components of the RFB-SE were tested for their preliminary scattering intensities before testing in the fully assembled state. The components consisted of two copper-clad aluminum current collectors, two graphite flow-fields, two carbon-based electrodes (cloth, paper, or felt), and a Nafion 212 proton exchange membrane. The Nafion membrane was tested in a dry state followed by a hydrated state in deuterium oxide. Figure A.5 shows the scattering profiles of all the individual components. The scattering intensity of the Nafion membrane is unfortunately multiple orders of magnitude lower than the intensities of all the other components. Figure A.6 shows the scattering intensity of the fully assembled RFB-SE, which was filled with D_2O in order to attempt to improve the contrast towards the Nafion membrane. Unfortunately, the scattering intensity of the Nafion membrane was completely overshadowed by the intensity of the other components, especially since that in this configuration there are two layers of each component and only one single membrane. Further modification of the RFB-SE is necessary in order to obtain scattering profiles of the membrane *in-situ*, specifically with regards to finding alternate materials for the components whose scattering intensities are too high. Titanium is a possible candidate; however, the carbon-based electrodes will pose a challenge as these are necessary for RFB operation.

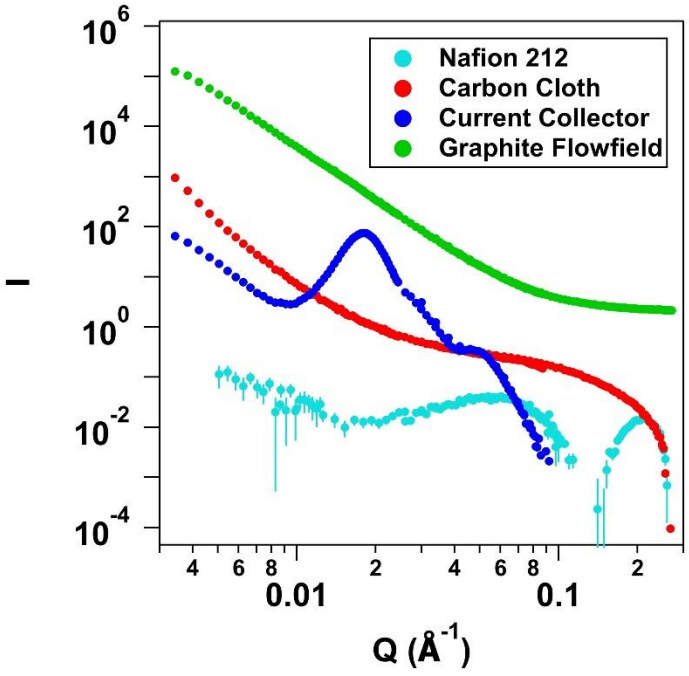

Figure A.5. SANS profiles of RFB-SE components.

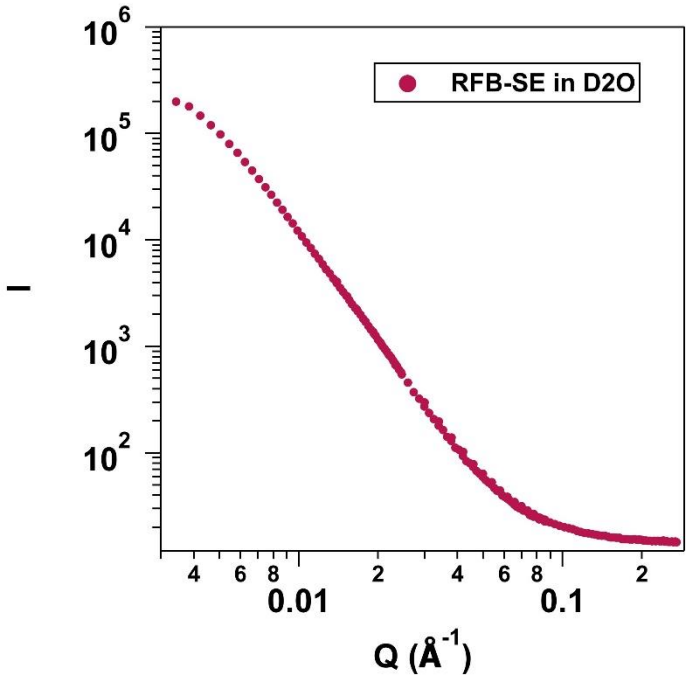

Figure A.6. SANS profiles of fully assembled RFB-SE with D_2O.

4 REFERENCES

1. Wei, X. *et al.* Materials and Systems for Organic Redox Flow Batteries: Status and Challenges. *ACS Energy Lett.* **2**, 2187–2204 (2017).

2. Chen, H., Cong, G. & Lu, Y. C. Recent progress in organic redox flow batteries: Active materials, electrolytes and membranes. *J. Energy Chem.* (2018). doi:10.1016/j.jechem.2018.02.009

3. Shah, A. A. *et al.* Recent developments in organic redox flow batteries: A critical review. *J. Power Sources* **360**, 243–283 (2017).

4. Singh, V., Kim, S., Kang, J. & Byon, H. R. Aqueous organic redox flow batteries. *Nano Res.* (2019). doi:10.1007/s12274-019-2355-2

5. Ohashi, Y., Sawada, K. & Iimura, N. *Complex Formation of Surfactants with Aromatic Compounds and their Pharmaceutical Applications*. (2010).

6. Hatakeyama-Sato, K. *et al.* Hydrophilic Organic Redox-Active Polymer Nanoparticles for Higher Energy Density Flow Batteries. (2019). doi:10.1021/acsapm.8b00074

7. Janoschka, T. *et al.* An aqueous, polymer-based redox-flow battery using non-corrosive, safe, and low-cost materials. *Nat. Publ. Gr.* **527**, 78–81 (2016).

8. Montoto, E. C. *et al.* Redox Active Colloids as Discrete Energy Storage Carriers. (2016). doi:10.1021/jacs.6b06365

9. Kalisvaart, W. P., Fritzsche, H. & Méridamérida, W. Water Uptake and Swelling Hysteresis in a Nafion Thin Film Measured with Neutron Reflectometry. (2015). doi:10.1021/acs.langmuir.5b00764

10. Duan, Q., Wang, H. & Benziger, J. Transport of liquid water through Nafion membranes. *J. Memb. Sci.* **392**, 88–94 (2011).

11. Rollet, A.-L., Diat, O. & Gebel, G. LETTERS A New Insight into Nafion Structure. (2002). doi:10.1021/jp020245t

12. Mauritz, K. A. & Moore, R. B. State of understanding of Nafion. *Chem. Rev.* **104**, 4535–

4585 (2004).